Ozone ~~and~~, DNA active UV radiation **and cloud** changes for the near global mean and at high latitudes due to enhanced greenhouse gas concentrations

Kostas Eleftheratos[1,2], John Kapsomenakis[3], Ilias Fountoulakis[4,5], Christos S. Zerefos[2,3,6], Patrick Jöckel[7], Martin Dameris[7], Alkiviadis F. Bais[8], Germar Bernhard[9], Dimitra Kouklaki[1], Kleareti Tourpali[8], Scott Stierle[10], J. Ben Liley[11], Colette Brogniez[12], Frédérique Auriol[12], Henri Diémoz[5], Stana Simic[13], Irina Petropavlovskikh[14], Kaisa Lakkala[15,16], Kostas Douvis[3]

[1]Department of Geology and Geoenvironment, National and Kapodistrian University of Athens, Athens, Greece
[2]Center for Environmental Effects on Health, Biomedical Research Foundation of the Academy of Athens, Athens, Greece
[3]Research Centre for Atmospheric Physics and Climatology, Academy of Athens, Athens, Greece
[4]Institute for Astronomy, Astrophysics, Space Applications and Remote Sensing, National Observatory of Athens (IAASARS/NOA), Athens, Greece
[5]Aosta Valley Regional Environmental Protection Agency (ARPA), Saint-Christophe, Italy
[6]Navarino Environmental Observatory (N.E.O), Messenia, Greece
[7]Deutsches Zentrum für Luft- und Raumfahrt, Institut für Physik der Atmosphäre, Oberpfaffenhofen, Germany
[8]Department of Physics, Aristotle University of Thessaloniki, Thessaloniki, Greece
[9]Biospherical Instruments Inc., San Diego, CA 92110, USA
[10]NOAA Global Monitoring Laboratory, Boulder, CO 80305, USA
[11]National Institute of Water & Atmospheric Research (NIWA), Lauder, New Zealand
[12]Univ. Lille, CNRS, UMR 8518 - Laboratoire d'Optique Atmosphérique, F-59000 Lille, France
[13]Institute for Meteorology and Climatology, University of Natural Resources and Life Sciences, Vienna 1180, Austria
[14]Cooperative Institute for Research in Environmental Sciences, University of Colorado, Boulder, CO, USA
[15]Space and Earth Observation Centre, Finnish Meteorological Institute, Sodankylä, Finland
[16]Climate Research Programme, Finnish Meteorological Institute, Helsinki, Finland

Correspondence to: Kostas Eleftheratos (kelef@geol.uoa.gr)

Abstract. This study analyses the variability and trends of ultraviolet-B (UV-B, wavelength 280–320 nm) radiation that can cause DNA damage, which are caused by climate change due to enhanced greenhouse gas (GHG) concentrations. The analysis is based on DNA active irradiance, total ozone, total cloud cover, and surface albedo calculations with the EMAC Chemistry-Climate Model (CCM) free running simulations following the RCP-6.0 climate scenario for the period 1960–2100. The model output is evaluated with DNA active irradiance ground-based measurements, satellite SBUV (v8.7) total ozone measurements and satellite MODIS/Terra cloud cover data. The results show that the model reproduces the observed variability and change of total ozone, DNA active irradiance, and cloud cover for the period 2000-2018 quite well according to the statistical comparisons. Between 50° N–50° S, the DNA-damaging UV radiation is expected to decrease until 2050 and to increase thereafter, as it was shown previously by Eleftheratos et

al. (2020). This change is associated with decreases in the model total cloud cover and ~~insignificant~~ negative trends in total ozone after about 2050 due to increasing GHGs. The new study confirms the previous work by adding more stations over low and mid-latitudes (13 instead of 5 stations). In addition, we include estimates from high latitude stations with long-term measurements of UV irradiance (~~2~~ 3 stations in the northern high latitudes and 4 stations in the southern high latitudes greater than 55°). In contrast to the predictions for 50° N–50° S, it is shown that DNA active irradiance will continue to decrease after the year 2050 over high latitudes because of upward ozone trends. At latitudes poleward of 55° N, we estimate that DNA active irradiance will decrease by ~~10.6~~8.2 ± ~~3.7~~3.8% from 2050 to 2100. Similarly, at latitudes poleward of 55° S, DNA active irradiance will decrease by 4.8 ± 2.9% after 2050. The results for the high latitudes refer to the summer period and not to the seasons when ozone depletion occurs, i.e., in late winter and spring. The contributions of ozone, cloud and albedo trends on the DNA active irradiance trends are estimated and discussed.

1 Introduction

The observed depletion of stratospheric ozone in the middle and high latitudes in the 1980s and the 1990s was followed by a general stabilization in the 2000s and by signs of recovery in the 2010s (Solomon et al., 2016; Weber et al., 2018; Krzyścin and Baranowski, 2019). The general behavior of ozone in the last 4 decades motivated research into the response of UV variability to ozone variability during periods with and without ozone decline. UV-B radiation is of special importance because of its effects on human health and the environment. In the short-term, the biological effects of UV-B radiation on humans include skin effects (erythema, photodermatitis) and eye effects (keratitis, conjunctivitis). Long-term effects include skin cancer, skin aging and cataracts. UV radiation can also damage the immune system and DNA (Lucas et al., 2019, Section 3.2 and references therein).

Changes in UV-B radiation and their relation to the depletion of the ozone layer in the stratosphere are being studied since the early 1990s (e.g., Blumthaler and Ambach, 1990; McKenzie, 1991; Bais and Zerefos, 1993; Bais et al., 1993). Early measurements of solar UV irradiance suggested that the long-term increase of the strongly ozone dependent wavelength of 305 nm was solely attributed to the observed stratospheric ozone decline and that it was not the result of improvements of air quality in the troposphere and changes in environmental conditions (Kerr and McElroy, 1993; Zerefos et al., 1998). Later studies based on longer atmospheric measurements looked at the effects of cloud cover, aerosols, air pollutants and surface reflectance on the long-term UV variability (e.g., Bernhard et al., 2007; den Outer et al., 2010; Kylling et al., 2010; Douglass et al., 2011). Over Canada, Europe, and Japan, it was found that the observed positive change in UV-B irradiance could not be explained solely by the observed ozone change and that a large part of the observed UV increase was attributed to tropospheric aerosol decline, the so-called brightening effect (Wild et al., 2005), since cloudiness had no significant trends (Zerefos et al., 2012). At

high latitudes on the other hand, it was found that the long-term variability of UV-B irradiance was not affected by aerosol trends but by ozone trends (Eleftheratos et al., 2015).

Further efforts to understand the interactions between solar UV radiation and related geophysical variables were done by Fountoulakis et al. (2018). They concluded that the long-term changes in UV-B radiation vary greatly over different locations over the Northern Hemisphere, and that the main drivers of these changes are changes in aerosols and total ozone. Updated analysis of total ozone and spectral UV data recorded at four European stations during 1996–2017 revealed that long-term changes in UV are mainly driven by changes in aerosols, cloudiness, and surface albedo, while changes in total ozone play a less significant role (Fountoulakis et al., 2020b). Over higher latitudes, part of the observed changes may be attributed to changes in surface reflectivity and clouds (Fountoulakis et al., 2018 and references therein). Dedicated studies assessing trends of UV radiation in Antarctica provided further evidence that the UV indices are now decreasing in Antarctica during summer months, but not yet during spring when the ozone hole leads to large UV index variability (Bernhard and Stierle, 2020). The downward trends in UV index during summer are associated with upward trends in total ozone.

Long-term predictions of UV radiation are governed by assumptions about the future state of the ozone layer, changes in clouds, changes in tropospheric pollution, mainly aerosols, and changes in surface albedo. Unpredictable volcanic eruptions, increasing emissions of GHGs, effects from growing air traffic, changes in air quality and changes in the oxidizing capacity of the atmosphere induce uncertainties to long-term predictions of ozone and therefore to UV radiation levels (Madronich et al., 1998). The Environmental Effects Assessment Panel of the United Nations Environment Programme publishes the most recent global environmental effects from the interactions between stratospheric ozone, UV radiation and climate change. The Panel noted that future changes in UV radiation will be influenced by changes in seasonality and extreme events due to climate change (Neale et al., 2021). Simulations of surface UV erythemal irradiance by Bais et al. (2011) showed that UV irradiance will likely return to its 1980 levels by the first quarter of the 21st century at northern mid and high latitudes, and 20-30 years later at southern mid- and high latitudes. After reaching this level, UV will continue to decrease towards 2100 in the Northern Hemisphere because of the continuing increases in total ozone due to circulation changes induced by the increasing GHG concentrations, whereas it is highly uncertain whether UV will reach its 1960s levels by 2100 in the Southern Hemisphere (Bais et al., 2011). However, in the Arctic, large, seasonal loss of column ozone could persist for much longer that commonly appreciated. Projections of stratospheric halogen loading and humidity with General Circulation Model (GCM)-based forecasts of temperature, suggested that conditions favorable for large Arctic ozone loss could persist or even worsen until the end of this century, if future GHG concentrations continue to steeply rise. Consequently, anthropogenic climate change has the potential to partially counteract the positive effects of the Montreal Protocol in protecting the Arctic ozone layer (von der Gathen et al., 2021). CCM simulations of DNA-damaging UV variability analyzed by Eleftheratos et al. (2020) showed that UV irradiance will likely increase at low and mid-latitudes during the second half

of the 21st century due to decreases in cloud cover driven by climate change caused by enhanced GHG concentrations.

GHG changes can be an important driver of cloudiness changes. Norris et al. (2016) provided evidence for climate change in the satellite cloud record. They estimated fewer clouds over the mid-latitudes from 1983 to 2009 and concluded that the observed and simulated cloud change patterns are consistent with poleward retreat of mid-latitude storm tracks, expansion of subtropical dry zones, and increasing height of the highest cloud tops at all latitudes. The primary drivers for these changes were found to be the increasing GHG concentrations and a recovery from volcanic radiative cooling (Norris et al., 2016). In the same direction, Schneider et al. (2019) showed that stratocumulus clouds, some of the planet's most effective cooling systems, become unstable and break up into scattered clouds under increasing GHG concentrations. Their results also showed that less clouds will trigger additional surface warming in addition to that from the rising CO2 levels (Schneider et al., 2019). Both studies provided indications that increasing GHGs can affect clouds, which in turn can affect the UV radiation changes.

In this work we investigate the UV variability and trends for the near global mean (50° N–50° S) and at high latitudes due to the expected increase of GHG concentrations in the future. We show that DNA active irradiance will continue to decrease after 2050 at high latitudes due to the prescribed evolution of greenhouse gases in contrast to regions located between 50° N and 50° S where it is shown to increase. The year 2050 was chosen as a mid-point to evaluate the trends as it divides the 21st century into two equal periods, 2000-2049 and 2050-2099, but most importantly because it was noted that for a Representative Concentration Pathway (RCP) of 6.0, the Chemistry-Climate Model Initiative (CCMI, phase 1) simulations project that global total column ozone will return to 1980 values around the middle of this century (Dhomse et al., 2018). Our study confirms the previous work by Eleftheratos et al. (2020), which focused on ozone profiles from five well-maintained lidar stations at low and mid-latitudes. Here, we add more ozone and UV stations in mid-latitudes and include estimates from high latitude stations with long-term measurements of UV radiation. The analysis aims to investigate whether the increase of DNA active radiation predicted for mid-latitudes in view of climate change, will also be observed at high latitudes. To address the issue, we use the same methodology as Eleftheratos et al. (2020), in which we compare two CCM simulations; one with increasing GHGs according to RCP-6.0 and one with fixed GHGs emissions at 1960 levels. The variability of ozone from the model simulations is evaluated against solar backscatter ultraviolet radiometer 2 (SBUV/2) satellite ozone data. The variability of DNA active irradiance from the model simulations is evaluated against ground-based DNA active radiation measurements, and the variability of simulated cloud cover is evaluated against cloud fraction data from the MODerate-resolution Imaging Spectroradiometer (MODIS)/Terra v6.1 satellite dataset.

It is important to clarify the novelty of this research and its added value with respect to the previous study, and to point out the main differences and similarities. The objective of this research is to study how total ozone, DNA active irradiance and cloud cover might change in the future at high latitudes due to the

149 increasing GHGs in comparison to the near global mean (50° N–50° S). Also, to estimate the part of the
150 DNA active irradiance change that can be explained by ozone and cloud changes in the future using
151 multiple linear regression (MLR) statistical analysis. The previous study by Eleftheratos et al. (2020) did
152 not look at high latitudes and did not apply MLR analysis to quantify the related contributions to the DNA
153 weighted UV irradiance. The previous work analysed 5 stations between 50° N and 50° S. The new study is
154 enriched with more stations at the near global scale (13 instead of 5 stations, of which 4 are identical) and,
155 in addition, it includes analysis of averages in latitudinal bands, which was not done in the previous study,
156 thus providing more complete results.

157 The study is organized as follows. Section 2 describes the data sources and methodology. Section 3 shows
158 the variability and projections of DNA-damaging UV radiation at high latitude stations in comparison to
159 mid-latitude stations, and, finally, Section 4 summarizes the main results.

160 **2 Data sources**

161 **2.1. Ground-based data**

162 We have analyzed DNA-weighted UV irradiance data at ~~19~~ 20 ground-based (GB) stations listed in Table
163 1. Although the DNA action spectrum tends to exaggerate UV effects on humans, mammals, etc., (as it was
164 determined with bacteria and viruses and does not take the wavelength dependence of the skin's
165 transmission into account), it is the appropriate action spectrum for studying the detrimental biological
166 effects of solar radiation and the effective dose of UV radiation in producing skin cancer (Setlow, 1974).

167 Most of the stations listed in Table 1 contribute spectral UV data to the data repository of the Network for
168 the Detection of Atmospheric Composition Change (NDACC, www.ndacc.org) at https://www-
169 air.larc.nasa.gov/pub/NDACC/PUBLIC/stations/~~https://ftp.cpc.ncep.noaa.gov/ndacc/station/~~ (last access ~~10~~
170 ~~February~~4 September 2022) (De Mazière et al., 2018) and have been reported among those possessing
171 high-quality long term UV irradiance measurements (McKenzie et al., 2019). Sites not part of NDACC are
172 Aosta, Athens, Sodankylä, and Thessaloniki. Data from these stations are of high-quality as well (e.g.,
173 Fountoulakis et al., 2018; Fountoulakis et al., 2020a; Kosmopoulos et al., 2021; Lakkala et al., 2008). The
174 high quality of the spectral UV measurements is ensured by applying strict calibration and maintenance
175 protocols.

176 We have calculated monthly mean irradiances from noon averages for all stations listed in Table 1 (average
177 of measurements ± 45 minutes around local noon) and compared them with the DNA active irradiance data
178 from an EMAC sensitivity simulation (internally named SC1SD-base-02), with specified dynamics
179 representing the recent past (2000-2018) as a means for model evaluation. The comparisons are presented
180 in Section 3.1 and in the Supplementary materials of this study for each station separately.

2.2. Satellite data

We have analyzed the daily solar backscatter ultraviolet radiometer 2 (SBUV/2) ozone profile and total ozone data, selected to match the UV stations' locations. The data are available from April 1970 to the present, with nearly continuous data coverage from November 1978. The satellite ozone data coverage is from backscatter ultraviolet radiometer (BUV) to solar backscatter ultraviolet radiometer 2 (SBUV-2; Bhartia et al., 2013), as follows: Nimbus-4 BUV (05/1970–04/1976), Nimbus-7 SBUV (11/1978–05/1990), NOAA-9 SBUV/2 (02/1985–01/1998), NOAA-11 SBUV/2 (01/1989–03/2001), NOAA-14 SBUV/2 (03/1995–09/2006), NOAA-16 SBUV/2 (10/2000–05/2014), NOAA-17 SBUV/2 (08/2002–03/2013), NOAA-18 SBUV/2 (07/2005–11/2012), NOAA-19 SBUV/2 (03/2009–present) and Suomi NPP OMPS (12/2011–present). We calculated daily averages by averaging the measurements from all available SBUV instruments, and then we calculated monthly means from daily averages according to Zerefos et al. (2018).

Cloud fraction monthly mean data were taken from the MODIS/Terra v6.1 dataset for the period 2000–2020. We include estimates of the variability in cloudiness around each of the ground-based monitoring stations listed in Table 1. The cloud data were taken at a spatial resolution of 3° × 3° around each monitoring station. We have calculated the correlation coefficients between the de-seasonalized monthly time series of cloud fraction from MODIS/Terra and EMAC CCM for their common period (03/2000–07/2018), in order to evaluate the model simulations. The seasonal component was removed from the series by subtracting from each monthly value the 2000–2018 seasonal mean. Analytical estimates are provided in Section 3.1 and in the Supplementary materials.

2.3. EMAC Chemistry climate model (CCM) simulations

We use the same CCM simulations and methodology as described by Eleftheratos et al. (2020). The simulations come from the European Centre for Medium-Range Weather Forecasts – Hamburg (ECHAM) / Modular Earth Submodel System (MESSy) Atmospheric Chemistry (EMAC) model. The EMAC model is designed to study the chemistry and dynamics of the atmosphere (Jöckel et al., 2016). The resolution applied here is 2.8º x 2.8º in latitude and longitude, with 90 model levels reaching up to 0.01 hPa (about 80 km).

~~Two free running hind case and projection simulations have been analyzed, both based on boundary conditions following the RCP 6.0 scenario: the reference simulation RC2 base 04 (1960 2100, with additional 10 years spin-up; Jöckel et al., 2016) and the sensitivity simulation SC2 fGHG-01 (1960 2100), in which the GHG mixing ratios have been kept on 1960 levels (Dhomse et al., 2018). Furthermore, we~~We have analyzed the EMAC RC1SD-base-10 (Jöckel et al., 2016) and SC1SD-base-02 simulation results of ozone, DNA active irradiance, and total cloud cover (in %). These simulations have been performed in a "specified dynamics" (SD) setup, i.e., nudged with ECMWF ERA-Interim reanalysis data (Dee et al., 2011) for the periods January 1979 – December 2013 (RC1SD-base-10) and January 2000 – July 2018 (SC1SD-base-02), respectively, and are therefore particularly suited for a direct comparison with observations such

as ground-based and satellite measurements as presented in Section 3.1 and Appendix A. We note that the SD simulation RC1SD-base-10 (which starts in 1979) is used for the comparisons during the period of ozone depletion as the SC1SD-base-02 doesn't cover that period (the 80's and 90's).

Two free running hind-case and projection simulations have been analyzed, both based on boundary conditions following the RCP-6.0 scenario: the reference simulation RC2-base-04 (1960–2100, with additional 10 years spin-up; Jöckel et al., 2016) and the sensitivity simulation SC2-fGHG-01 (1960–2100), in which the GHG mixing ratios have been kept on 1960 levels (Dhomse et al., 2018). The RC2-base-04 and SC2-fGHG-01 simulations were forced with sea surface temperatures (SSTs) and sea ice concentrations (SICs) from the Hadley Centre Global Environment Model version 2 – Earth System (HadGEM2-ES) Model (Collins et al., 2011; Martin et al., 2011). These simulations were performed for the Coupled Model Intercomparison Project – Phase 5 (CMIP5) multi-model data sets in the frame of the Program for Climate Model Diagnosis and Intercomparison (PCMDI). For years up to 2005, the data of the "historical" simulation with HadGEM2-ES is used. Afterwards, the RCP-6.0 simulation, which is initialized with the historical simulation, has been employed (Jöckel et al., 2016, and reference therein). The future solar forcing, used for the projections, has been prepared according to the solar forcing used for CMIP5 simulation of HadGEM2-ES, where the SSTs and SICs are taken from Jones et al. (2011; see also Sect. 3.3 of Jöckel et al., 2016). It consists of repetitions of an idealized solar cycle connected to the observed time series in July 2008. This has been applied consistently for all projections with prescribed SSTs (RC2-base) and the same holds also for the SC-simulations. Here, we deviate from the CCMI recommendations consisting of a sequence of the last four solar cycles (20–23) (see Sect. 3.4 of Jöckel et al., 2016).

The UV-B radiation calculated by the photolysis scheme (JVAL) (Sander et al., 2014) is weighted with the DNA damage potential of Setlow (1974) with the parameterization by Brühl and Crutzen (1989). The DNA damaging irradiance of the NDACC database is again based on the action spectrum by Setlow (1974) and parameterized using Eq. (2) of Bernhard et al. (1997). The different parameterization of the DNA action spectrum in the EMAC CCM simulations and the GB measurements will likely lead to small difference between the two datasets. For example, the radiative amplification factors (RAFs) for the two parameterizations may not be identical, which may lead to seasonal variations because RAFs are solar zenith angle and ozone dependent. To reduce such differences, we only compared de-seasonalized data. The seasonal component at each station was removed by subtracting the long-term monthly mean (2000–2018) from each individual monthly value. The monthly departures were then expressed in percent of the long-term monthly mean.

Ozone and total cloud cover data from the two RC2-base-04 and SC2-fGHG-01 free running simulations for the stations listed in Table 1 have been analyzed as well and respective de-seasonalized monthly means were derived. Here, the monthly data were de-seasonalized with respect to the 30-year long-term monthly mean (1990–2019).

252 We note here that by a separate analysis (not shown) on total cloud cover variability and trends through the
253 21st century, using the available simulations from the CCMI-1 REF-C2 set (e.g., Eyring et al., 2013), the
254 EMAC models results fall well within the range of uncertainty, close to the ensemble average.

255 In all simulations analyzed here, we used prescribed aerosol distributions. The prescribed aerosol effects
256 are separated into the aerosol surface area, representing chemical effects via heterogeneous chemistry, and
257 the radiative properties influencing the radiation budget (Sect. 3.7 of Jöckel et al., 2016). Due to a glitch,
258 the stratospheric volcanic aerosol was not considered correctly in the free running simulations (Sect. 3.12.1
259 of Jöckel et al., 2016). Therefore, the dynamical effects of large volcanic eruptions (e.g. Mt. Pinatubo 1991;
260 El Chichón 1982) are essentially not represented in the simulations, except for the contribution to the
261 tropospheric temperature signal induced by the prescribed SSTs. For the specified dynamics simulations,
262 however, this has been corrected. Since the aerosol distributions have been prescribed, there is no aerosol
263 output for these simulations that we could look at. As such, we cannot investigate the impact of future
264 changes in aerosol loading on the UV radiation reaching the surface.

265 In the following sections, to assist the reader to easily follow the figure content, we change the notation of
266 our simulations as follows:

267 • SC1SD-base-02: further abbreviated as HIS-SD for historical specified dynamics
268 • RC2-base-04: further denoted as REF for reference, and
269 • SC2-fGHG-01: further denoted as FIX for fixed GHGs.

270

271 **2.4. Statistical methods**

272 In Section 3.1, we evaluate the variability of DNA active irradiance from the model simulations with
273 station measurements for a nearly 20-year period (2000–2018). The comparisons were based on regression
274 analyses between the simulated and observed DNA active irradiance monthly data after removing
275 variations related to the seasonal cycle. The monthly data at each station were de-seasonalized by
276 subtracting the long-term monthly mean (2000–2018) pertaining to the same calendar month.

277 We have calculated the Pearson's correlation coefficients, R, between the simulated and measured DNA
278 active irradiance (Eq. 1) and tested them for statistical significance using the t–test formula for the
279 correlation coefficient with n–2 degrees of freedom (Eq. 2) (von Storch and Zwiers, 1999):

$$R = \frac{\sum_{i=1}^{n}(x_i - \bar{x})(y_i - \bar{y})}{\sqrt{\sum_{i=1}^{n}(x_i - \bar{x})^2}\sqrt{\sum_{i=1}^{n}(y_i - \bar{y})^2}} \qquad (1)$$

280 Where x refers to the measured and y to the simulated data.

$$t = R\sqrt{\frac{n-2}{1-R^2}} \tag{2}$$

281 The same procedure was followed for the comparisons between the simulated and satellite derived total
282 ozone and cloud cover datasets for the period 2000–2018, which are presented in Section 3.1.

283 In Section 3.3, we apply a statistical test to compare the regression slopes in DNA active irradiances before
284 and after the year 2050. The null hypothesis, that the two slopes are statistically equal ($H_0: b_1 = b_2$), is
285 tested against the alternative hypothesis that the two slopes are not statistically equal ($H_1: b_1 \neq b_2$). The
286 difference in slopes is tested with the statistic:

$$t = \frac{b_1 - b_2}{s_{(b_1-b_2)}} = \frac{b_1 - b_2}{\sqrt{s_{b_1}^2 + s_{b_2}^2}} \tag{3}$$

287 With $n_1 + n_2 - 4$ degrees of freedom, according to Eq. (11.20) of Armitage et al. (2002). The parameter
288 $s_{(b_1-b_2)}$ is the standard error of $(b_1 - b_2)$. The parameters b_1 and b_2 are the slopes before and after 2050
289 in each geographical zone, and n_1 and n_2 are the numbers of data before and after 2050, respectively. The
290 test was performed using de-seasonalized monthly values but also with the averages shown in Figures 4c,
291 5c, 6c, calculated from de-seasonalized data. Both ways gave similar statistical results. In Section 3.3 we
292 provide the results using the de-seasonalized monthly values.

293 The equation for the slope of the regression line, using x as the time variable and y as the DNA active
294 irradiance variable, is:

$$b = \frac{\sum(x - \bar{x})(y - \bar{y})}{\sum(x - \bar{x})^2} \tag{4}$$

295 The residual mean square for the first group (1960-2049), $s_{b_1}^2$, is estimated as follows:

$$s_{b_1}^2 = \frac{\sum_{(1)}(y - Y_1)^2}{n_1 - 2} = \frac{S_{yy1} - S_{xy1}^2/S_{xx1}}{n_1 - 2} \tag{5}$$

296 And the corresponding mean square for the second group (2050-2099), $s_{b_2}^2$, as follows:

$$s_{b_2}^2 = \frac{\sum_{(2)}(y - Y_2)^2}{n_2 - 2} = \frac{S_{yy2} - S_{xy2}^2/S_{xx2}}{n_2 - 2} \tag{6}$$

297   Here, S_{yy} is the standard deviation of DNA active irradiance, S_{xx} is the standard deviation of time and

298   S_{xy} is their covariance, for the first (1960-2049) and second (2050-2099) groups, respectively.

299   If $|t| > t_{critical\ (n_1+n_2-4)}$, then the null hypothesis, H_0: the slopes are equal, is rejected at the significance

300   level a, and the alternative hypothesis (the two slopes are statistically different) is accepted.

301

3 Results and discussion

3.1 Evaluation of EMAC CCM simulations for the present

304   DNA active irradiance data from station observations and model simulations have been compared, for a

305   nearly 20 year period (2000 2018). The comparisons were based on regression analyses between the

306   simulated and observed DNA active irradiance monthly data after removing variations related to the

307   seasonal cycle. The monthly data at each station were de seasonalized by subtracting the long term

308   monthly mean (2000 2018) pertaining to the same calendar month.

309   The time series of de-seasonalized DNA active irradiance data are presented in Figure 1. The figure

310   compares model calculations of DNA active irradiance from the SC1SD base 02HIS-SD simulation with

311   ground-based measurements at stations described in Section 2. The upper panel refers to the average of de-

312   seasonalized data at two three stations in the northern high latitudes, the middle panel refers to the

313   respective average of thirteen stations between 50º N and 50º S, and the lower panel to the respective

314   average of four stations in the southern high latitudes. The comparisons refer to the period 2000–2018. We

315   note that this is a composite dataset, obtained with the same set of stations (both in the model and in the

316   observations). All timeseries start from the same year in the model, but not all timeseries start from the

317   same year in the observations.

318   We have calculated the Pearson's correlation coefficients, R, between the two datasets and tested them for

319   statistical significance using the t test formula for the correlation coefficient with n 2 degrees of freedom

320   (von Storch and Zwiers, 1999):

$$t = R\sqrt{\frac{n-2}{1-R^2}} \tag{1}$$

321   The correlations between the simulated and ground based DNA active irradiance data are statistically

322   significant. The results are presented in Table 2a. The de seasonalized data from the model agree quite well

323   with those measured from the ground, except for Barrow, Zugspitze, and Reunion Island, where they show

324   smaller correlation coefficients (0.342, 0.266, and 0.295, respectively) which may be related with the

325   coarse resolution of the model simulations (2.8°x2.8°). The correlation results between the two data sets at

The results show that the correlations between the simulated and ground-based DNA active irradiance data are statistically significant. Figure 1, however, shows that the variability between the simulated and ground-based data can be different. To have a better indication how the two datasets are scattered, Figure 2 presents the respective scatter plots. We have added the linear regression line and the y=x line which shows how much the slope of the fit deviates from the 1:1 line. The statistical results (correlation coefficient, slope, error, t-value, p-value, and root mean square error (RMSE)) are summarized in Table 2a.

The comparison for the near-global mean shows that the correlation coefficient between the simulated and observed DNA active irradiances is +0.709, the slope of the fit is 0.521, its error is 0.035, and the RMSE is 4.423. For the northern high latitudes, the statistical results are estimated to be R = 0.518, slope = 0.657, error of slope = 0.129, RMSE = 9.543. The respective results for the southern high latitudes are R = 0.746, slope = 0.879, error of slope = 0.070, RMSE = 14.766. It appears that the slope of the regression fit for the near-global mean is small; however, the RMSE, which is the measure of the differences between the simulated and observed values, is also small. A RMSE of 0 would indicate a perfect fit to the data, something that is never achieved in practice. It also appears that the respective RMSE of the residuals (i.e., simulated minus observed values) are larger at high latitudes; this is because it was derived from larger differences of de-seasonalized data at the northern high latitudes and even larger at the southern high latitudes.

The regression analysis results between the two data sets at each station separately are presented in Supplement Table S1. We note here that the model has a resolution of 2.8° x 2.8°, which is a large area for which the point measurement has to be representative for. As such, for stations where the surrounding area is inhomogeneous, such as mountain tops (Mauna Loa, Sonnblick, Zugspitze), or in valleys (Aosta), or by being in a town with very heterogeneous surroundings (sea, mountains, tropospheric ozone and aerosols such as Athens), the model simulations of DNA active irradiance are not expected to be fully representative of the specific UV sites. Thus, the correlation between simulated and measured DNA weighted UV irradiance is not very good at some stations, as shown in the figures provided in the supplementary material. For the same reason, the slope between two datasets can deviate significantly from unity (see Supplement Table S1). Therefore, the comparisons at the individual stations provide a qualitative evaluation of the model's variability, but cannot be considered as a strict validation of the model. We provide here indicative estimates for individual stations, which give very good to excellent correlations: a) Summit, Greenland: R = +0.709, slope = 0.757, error of slope = 0.081, p-value <0.0001, N = 88, b) Hoher Sonnblick, Austria: R = +0.673, slope = 0.946, error of slope = 0.075, p-value <0.0001, N = 192, c) Boulder, CO, USA: R = +0.748, slope = 0.677, error of slope = 0.047, p-value <0.0001, N = 163, d) Arrival Heights, Antarctica: R = +0.939, slope = 1.000, error of slope = 0.033, p-value <0.0001, N = 126.

The same procedure was followed to evaluate simulated ozone and cloud cover. Figure 2̶ 3 shows (a) ozone calculations from the S̶C̶1̶S̶D̶ ̶b̶a̶s̶e̶ ̶0̶2̶HIS-SD simulation compared to satellite SBUV retrievals and (b) shows simulated cloud cover compared to cloud cover from MODIS/Terra. It appears that the variability of ozone from the model simulation follows exceptionally well the variability of ozone from the satellite retrievals. It also appears that the variability of cloud cover from the model simulation is quite well correlated with the variability from the satellite observations (see Tables 2b and 2c). The respective comparisons using zonally averaged data for the northern high latitudes ($55^o – 75^o$ N), the near global mean (50° N – 50° S) and the southern high latitudes ($55^o – 75^o$ S) are presented in Supplement Figure S1. The regression results (R, slope, error of slope, t-value, p-value, and RMSE) for the large-scale latitudinal averages are presented in Supplement Table S2 and they are in line with the results from the station averages.

The Supplement Table S̶2̶ S3 presents analytically the comparisons of total ozone between the EMAC CCM calculations and SBUV satellite retrievals. The correlations between the two different data sets are statistically significant at confidence level greater than 99.9% at all stations under study. The correlation results for four indicative stations are: a) Summit, Greenland: R = +0.927, slope = 0.791, error of slope = 0.028, p-value <0.0001, N = 131, b) Hoher Sonnblick, Austria: R = +0.902, slope = 0.803, error of slope = 0.026, p-value <0.0001, N = 223, c) Boulder, CO, USA: R = +0.854, slope = 0.757, error of slope = 0.031, p-value <0.0001, N = 223, d) Arrival Heights, Antarctica: R = +0.896, slope = 0.655, error of slope = 0.029, p-value <0.0001, N = 128.

The Supplement Table S̶3̶ S4 presents the respective comparisons for cloud cover. The cloud observations come from MODIS/Terra. The correlation results for these four stations are: a) Summit, Greenland: R= +0.196, slope = 0.069, error of slope = 0.031, p-value = 0.025, N = 131, b) Hoher Sonnblick, Austria: R = +0.556, slope = 0.619, error of slope = 0.062, p-value <0.0001, N = 222, c) Boulder, CO, USA: R = +0.539, slope = 0.482, error of slope = 0.051, p-value <0.0001, N = 222, d) Arrival Heights, Antarctica: R = +0.537, slope = 0.949, error of slope = 0.133, p-value <0.0001, N = 129.

3.2 Future changes in ozone and DNA active irradiance

In the previous section we evaluated the SD simulation SC1SD-base-02 with satellite and ground-based measurements. In this section we use the EMAC CCM simulations to investigate the evolution of DNA active irradiance and o̶f̶ the parameters that affect its long-term variability into the future. More specifically, we have analyzed the free-running simulation of the EMAC CCM, namely RC2-base-04, with increasing GHGs according to RCP-6.0 at the stations under study. An evaluation of the free running simulation RC2-base-04 with the SD simulation SC1SD-base-02 is provided in Appendix A. It helps to evaluate the quality of the results of the free running model system with respect to the SD simulation and the observations of the stations, and it serves as a "bridge" from the observations via the SD simulation results to the results of the (longer-term) free-running model simulation.

396 We followed the same methodology as Eleftheratos et al. (2020), to examine the effect of increasing GHGs
397 on the evolution of DNA active radiation. We have compared the free-running simulation RC2-base-04
398 with the sensitivity simulation SC2-fGHG-01 where GHGs are kept constant at 1960 levels (see also
399 Appendix A). The difference between the two free-running simulations gives us an estimate of the desired
400 result.

401 We have prepared a series of figures to demonstrate the two different simulations and the differences
402 between them. Figure 3 4 is based on 13 UV stations between 50° north and south. Figure 4 5 shows the
403 results for the northern high latitude stations and Figure 5 6 for the southern high latitude stations. The top
404 panel refers to the evolution of total ozone anomalies from 1960 to 2100; the middle panel refers to the
405 evolution of DNA active irradiance and the lower panel to the evolution of clouds for the same period. The
406 left panel shows the two simulations, i.e., the free-running simulation with increasing GHGs (RC2 base-
407 04REF) versus the same simulation with fixed GHGs at 1960 levels (SC2 fGHG 01FIX) and the right
408 panel shows their respective differences. Shown are annual averages calculated from monthly de-
409 seasonalized data. The calculation of annual averages was done as follows: First, we de-seasonalized the
410 monthly data at each station by subtracting the long-term monthly mean (1990–2019) pertaining to the
411 same calendar month. Next, we calculated a monthly de-seasonalized time series for each geographical
412 zone by averaging the monthly de-seasonalized data of the stations belonging to each geographical zone.
413 The latter time series was used to estimate the annual data anomalies. For the northern high latitude
414 stations, the annual average refers to the average of monthly anomalies from March to September, and for
415 the southern high latitude stations, it refers to the average of monthly anomalies from September to March.
416 For the stations between 50° N–50° S we used all months to calculate the annual average.

417 In addition, we have added with green squares the DNA-weighted UV irradiance anomalies averaged at the
418 ground-based stations under study around local noon. We also include the total ozone anomalies from
419 SBUV with blue dots and the respective cloud cover anomalies from MODIS/Terra (magenta triangles)
420 averaged at the stations studied. The observational data have been added to show simply that the dispersion
421 of the simulated data matches the dispersion of the measured data.

422 In the study by Eleftheratos et al. (2020) data from 5 stations between 50 degrees north and south were
423 analyzed. Here, we examine for this latitude band 13 stations instead of 5 (Figure 34). The new findings
424 paint the same picture: an increasing trend in DNA active irradiance after the year 2050, associated with a
425 decreasing trend in cloud cover due to the evolution of GHGs and an insignificanta negative trend in total
426 ozone (Figure 3c4c). Thus, our new results, based on 13 instead of 5 stations, confirm qualitatively the
427 results of the previous study for 50° N–50° S. An offset between total ozone from SBUV and the free
428 running simulation is evident in the 1980s, which is larger at 50° N–50° S. This is discussed later.

429 The focus now is at higher latitudes, which show a different picture than that of 50° N–50° S after the year
430 2050. At the northern high latitude stations (Figure 45), DNA active irradiance (during the summer half
431 year) shows a decreasing trend after 2050, total ozone shows an increasing trend after 2050 and cloud cover

does not show any obvious statistically significant trend. The estimated trends (in % per decade) and their standard errors are presented in Table 3. More specifically, we estimate that total ozone will increase by ~~2.4~~1.8 ± ~~0.9~~0.8% from 2050 to 2100 (t-value = ~~2.675~~2.169, p-value = ~~0.01019~~0.035), DNA active irradiance will decrease by ~~10.6~~8.2 ± ~~3.7~~3.8% (t-value = ~~−2.161~~ −2.859, p-value = ~~0.00627~~0.036), and cloud cover will slightly increase by ~~1.3~~1.4 ± ~~2.0~~1.3% (t-value = ~~0.640~~1.061, p-value = ~~0.52496~~0.294). Accordingly, at the southern high latitude stations (Figure ~~5~~6), total ozone is estimated to increase by 4.2 ± 2.1% from 2050 to 2100 (t-value = 2.020, p-value = ~~0.04896~~0.049), DNA active irradiance is estimated to decrease by 4.8 ± 2.9% (t-value = −1.660, p-value = ~~0.10347~~0.103), and cloud cover will decrease insignificantly by 1.1 ± 1.7% (t-value = −0.604, p-value = ~~0.54842~~0.548).

The above estimates point to an increase in total ozone in the northern high latitudes by the end of the century on an almost year-round basis. In a recent study by von der Gathen et al. (2021), it was concluded that conditions favorable for large Arctic ozone loss during cold winters could persist or even worsen until the end of this century, if future abundances of GHGs continue to rise. As such, anthropogenic climate change has the potential to partially counteract the positive effects of the Montreal Protocol in protecting the Arctic ozone layer (von der Gathen et al., 2021). We examined the EMAC CCM projections regarding this finding. We have analyzed the ~~RC2-base-04~~REF and ~~SC2 fGHG 01~~FIX simulation results of ozone, DNA active irradiance, and cloud cover for January, February, and March for the ~~two~~three northern high latitude stations, ~~Summit and Barrow~~Summit, Barrow and Sodankylä. The trend results are presented in Table 4, which shows the trends from the two simulations, and their differences, for the periods 1960–1999, 2000–2049 and 2050–2099.

It appears that in January and February, considered as the two coldest months of the year, the trends decrease from the first (2000–2049) to the second period (2050–2099), while in March (less cold month) the picture is different. More specifically, in January, the significant positive trend of ~~1.72~~1.53 ± ~~0.59~~0.64% per decade in 2000–2049 changes to ~~−0.02~~0.21 ± ~~0.63~~0.73% per decade in 2050–2099. In February, the significant positive trend of ~~2.09~~1.79 ± ~~0.63~~0.78% per decade in 2000–2049 decreases to ~~1.39~~0.58 ± ~~0.62~~0.71% per decade in 2050–2099. On the other hand, the trends in March are ~~0.65~~0.17 ± ~~0.49~~0.58% per decade in 2000–2049 and ~~0.83~~1.20 ± ~~0.39~~0.51% per decade in 2050–2099, and they agree with the general course of trends seen in Figure ~~4~~5. We end up to findings that are qualitatively in agreement with those concluded by von der Gathen et al. (2021) about the large seasonal losses of Arctic ozone during cold winters until the end of the century. We also attempted to estimate the trends in DNA active irradiance in the northern high latitude stations for January, February, and March. The results are presented in Table 4 for the two periods, 2000–2049 and 2050–2099, but due to the polar night at the northern high latitudes, UV values are very low in January and February, and the predicted trends have large standard errors. As such, they are not analyzed any further.

Another issue is that Figure ~~4a~~5a suggests that clouds will stay more or less constant over the Arctic. Other models predict that cloud cover in the Arctic will increase until the end of the century. With sea ice

diminishing in the Arctic, evaporation would increase, leading to more moisture in the air, resulting in more clouds, which in turn is expected to reduce UV radiation. For example, Fountoulakis and Bais (2015) analyzed changes in UV radiation projected for the Arctic. Comparison of Figure 1 (clear-sky trends) and Figure 2 (all-sky trends) of Fountoulakis and Bais (2015) suggests that UV changes between the future and the present will become more negative when clouds are also considered due to the projected increase in cloud attenuation. Our estimates indicate a significant cloud increase of ~32.2% from 1960 to 2100 (~1.4% from 2050 to 2100, not significant). These increases are small and are based on the average of two three stations only, Summit and Barrow. Summit, Barrow and Sodankylä, but they are in accordance with the results obtained for the whole latitudinal band of 55°–75° N (~2.7% from 1960 to 2100, p-value < 0.0001, and ~0.9% from 2050 to 2100, p-value = 0.05). Summit and Sodankylä areis far away from the seashore and is are not affected by the ocean, while Barrow is located only 250 m away from the coast and is greatly affected by the ocean. Changes in cloudiness might be different at coastal and mainland sites. For Barrow (coastal site) we estimate a significant cloud increase of 5.5% in the period 1960–2100 (3% in the period 2050–2099), while for Summit (pure land site) we estimate an insignificant change of –0.1% in the period 1960–2100 (–0.4% in the period 2050–2100). For Sodankylä (also pure land site), we estimate an insignificant increase of 1.2% in the period 1960–2100 (p-value = 0.365), and of 1.6% in the period 2050–2100 (p-value = 0.446). Averaging large and small changes in cloudiness should finally result to moderate changes. These results generally agree with the results presented in other studies (Bais et al., 2015; Fountoulakis and Bais, 2015) for land areas of the Arctic (keeping also in mind that the results of the present study are averages for two three stations only). We note that the results presented in these two referenced studies were for RCPs 4.5 and 8.5, and thus not directly comparable with the results of our study. In a more recent study presenting RCP 6.0-based projections (Bais et al., 2019), it was shown that cloudiness changes at high latitudes would strongly affect the UV irradiance mainly over the ocean where the absence of sea ice would result to increased evaporation. For land, smaller and non-significant changes were reported (see Figure 8 of Bais et al., 2019), which is again in agreement with the results presented in our study. In another study (Figure 5 of Fountoulakis et al., 2014), changes in zonally averaged UV irradiance due to changes in cloudiness in 1950–2100 were estimated to be the order of 5–15% (depending on the RCP) for latitudes ~70 degrees. However, only changes over the ocean were considered in that study and not over land. Additional indications that our results should be considered representative of the two three stations under study and not the entire Arctic region is provided in Figure B1 (Appendix B), which shows the changes in zonal mean cloud cover for the Arctic region from the RC2-base-04REF simulation. It appears that the zonal mean cloudiness is expected to increase more and more as move northward of 50° towards the North pole, indicating that the largest changes in cloud cover are likely to occur over the ocean and not over land.

For the period 1960–1999, the DNA active irradiance (summer half year) showed upward trends in all geographical zones following the downward trends of total ozone. Nevertheless, we should note that the examined simulation RC2-base-04REF (simulation with full chemistry and increasing GHGs according to

505   RCP-6.0) seems to clearly underestimate the observed ozone depletion of the 1980s and 1990s in the

506   geographical region 50º N–50º S (Figure 3̶4), but in the higher latitude regions (Figs. 4̶ 5 and 5̶6) the

507   picture looks much better. This suggests that there may be a bias in the model, that might at least partly be

508   caused by not considering all ozone depleting substances (ODSs), but only a subset (only CFC-11 and

509   CFC-12 are considered; Jöckel et al., 2016). The R̶C̶2̶ ̶b̶a̶s̶e̶ ̶0̶4REF simulation also underestimates the

510   ozone depletion of the 1980s and 1990s in the northern high latitude stations (Figure 4̶5), but the picture is

511   better than that of 50º N–50º S. The S̶C̶2̶ ̶f̶G̶H̶G̶ ̶0̶1FIX simulation seems to reproduce better the Arctic

512   ozone depletion of the past. The latter, however, is coincidence; it only indicates that due to the higher

513   dynamic variability of the northern (winter) stratosphere, the evolution of the ozone layer in the Arctic

514   region is significantly affected by natural variability of the stratosphere due to planetary waves. The best

515   agreement between the R̶C̶2̶ ̶b̶a̶s̶e̶ ̶0̶4REF simulation and satellite measurements during the period of ozone

516   depletion is found for the southern high latitudes, as can be seen from Figure 5̶6. As such, we can infer that

517   the model simulations reproduce very well the observed ozone depletion of the past in particular in the

518   southern higher latitudes, and less well in the northern higher latitudes. Nevertheless, the simulated decline

519   of ozone during 1979–1999 and the minimum ozone values calculated by the model in the 1990s for the

520   near global mean (50° N-50° S) and for the higher latitudes, are qualitatively in line with the satellite ozone

521   observations, which is a good outcome. This is supported by Figure A1 (Appendix A), which shows the

522   free running simulation R̶C̶2̶ ̶b̶a̶s̶e̶ ̶0̶4REF against the SD simulation S̶C̶1̶S̶D̶ ̶b̶a̶s̶e̶ ̶0̶2HIS-SD which starts

523   in 2000. Because we wanted to evaluate the free running simulation for the period of ozone depletion, we

524   also analyzed the SD simulation RC1SD-base-10 which starts in 1979. It appears that the R̶C̶2̶ ̶b̶a̶s̶e̶ ̶0̶4REF

525   simulation seems to reproduce well the negative ozone trends during the period of ozone depletion, but not

526   the exact anomalies of a particular year. This is because the free running simulation has its own

527   meteorological/synoptical sequence, and thus we cannot expect that the observed time series of the past is

528   reproduced on a year-by-year basis in the free running simulation the same way is reproduced in the

529   simulation with "specified dynamics".

530   Finally, we should also refer to the recent assessment of the United Nations Environment Programme

531   (UNEP) Environmental Assessment Panel (EEAP) (Bernhard et al., 2020), which compared projections of

532   future UV radiation from two studies, Bais et al. (2019) and Lamy et al. (2019). We have compared our

533   trend estimates, which are based on one model only, with the estimates provided in Table 1 of Bernhard et

534   al. (2020), which are based on many models of the first phase of the Chemistry-Climate Model Initiative

535   (CCMI-1) and should therefore be considered more robust than the estimates provided here. We clarify that

536   it is only a qualitative comparison as our trends are based on DNA weighted irradiance while the table in

537   Bernhard et al. (2020) refers to erythema. The DNA radiation amplification factor is about 2.1 while that

538   for erythema is 1.2, which suggests that we would expect differences in trends by roughly a factor of 1.75.

539   We also note that the table of Bernhard et al. (2020) shows zonal mean changes of the clear-sky UV index,

540   whereas we estimate changes in DNA active irradiance based on station averages. Despite the

541   inconsistencies in the radiation fields being compared, our trend estimates from the R̶C̶2̶ ̶b̶a̶s̶e̶ ̶0̶4REF

simulation based on RCP-6.0 are qualitatively in line with the results presented by Bernhard et al. (2020) for the case of RPC-6.0. We estimate a statistically significant decrease in DNA active irradiance at the northern high latitude stations for the period 2015 to 2090 of about 16 17% (–16% for the zonal mean 55°–75° N). The numbers from Table 1 of Bernhard et al. (2020) for the northern high latitudes are –6% for the annual mean clear-sky UV index for the period 2015 to 2090, and –3%, –7%, –5% and –4% for January, April, July, and October, respectively. Our respective estimate for the southern high latitude stations is about –24% (–26% for the zonal mean 55°–75° S) and is also qualitatively in line with the negative trend estimates provided by Bernhard et al. (2020) for the southern high latitudes for the period 2015 to 2090 (–18% for the annual mean clear-sky UV index, and –8%, –6%, –6% and –23% for January, April, July, and October, respectively).

The above estimates are based on station averages. We have complemented the analysis presented in Figures 4, 5, 6 with zonally averaged data in order not to restrict the analysis of the model results to only 20 locations but to analyse the model results as a whole, for example in latitudinal bands. The Supplement Figures S2, S3, S4 show the changes from the free running simulations REF, FIX, and their differences, for the near global mean, the northern and southern high latitudes based on latitudinal averages. It appears that the results from the analysis of averaging the model data in latitudinal bands are in the same direction with that from the station averages. More specifically, for the near global mean we find similar results to those presented in Figure 4 for the station mean, but a stronger negative trend in total ozone after 2050 which together with the negative cloud trend drive the positive DNA active radiation trend after 2050. On the other hand, negative trends in ozone and clouds after 2050 are not observed in the northern or the southern high latitude belt.

We believe that the negative trends seen in the near-global mean after 2050 will result from the ongoing climate change that will affect ozone and clouds. It is well known that increasing GHG concentrations have led to tropospheric warming and stratospheric cooling over the last decades (Stocker et al., 2013; Zerefos et al., 2014). As a thermodynamic consequence, the troposphere has expanded and the height of the tropopause has increased (Santer et al., 2003). A recent study showed that the stratospheric layer has contracted substantially over the last decades due to increasing GHGs and will continue to contract under the RCP-6.0 scenario (Pisoft et al., 2021). Also, chemistry-climate and climate model projection results show an acceleration in Brewer-Dobson circulation in response to climate change (Butchard, 2014). These changes will not leave the ozone layer unaffected. Our model simulations for the near-global mean show a downward trend in total ozone after 2050, which will likely be shaped by the negative trends in the lower stratosphere due increasing GHGs. For clouds, it has been shown that increasing GHGs are responsible for less clouds over the mid-latitudes (Norris et al., 2016) and for breaking up stratocumulus clouds into scattered clouds (Schneider et al., 2019). Our simulations show that clouds will decrease in response to increasing GHGs, which is consistent with the indications from these studies.

The results based on the zonally averaged data fully support the basic finding of the paper that DNA active irradiance is expected to change differently at high latitudes than at near-global scale after around 2050. It will continue to decline at high latitudes mainly due to ozone recovery from the reduction of ODSs (cloud cover changes are not significant), while it is expected to increase on a near-global scale, affected by reductions in cloud cover and total ozone due to climate change. This of course is an outcome that emerges from the simulations of a single climate-chemistry model, and as such, it may well turn out to be true or false. Verification of the results from other model simulations would be important, but also important is the further investigation of cloud behaviour from the model simulations and their verification from high quality measurements. It is important to note that our free running simulations were designed according to the definitions for the reference and sensitivity simulations provided by the IGAC and SPARC communities to address emerging science questions, improve process understanding and support upcoming ozone and climate assessments (Eyring et al., 2013).

3.3 Statistical evaluation of differences between trends and statistical modelling

We have compared the regression slopes in DNA active irradiances before and after the year 2050. The null hypothesis, that the two slopes are statistically equal ($H_0: b_1 = b_2$), is tested against the alternative hypothesis that the two slopes are not statistically equal ($H_1: b_1 \neq b_2$). The difference in slopes is tested with the statistic:

$$t = \frac{b_1 - b_2}{s_{(b_1 - b_2)}} = \frac{b_1 - b_2}{\sqrt{s_{b_1}^2 + s_{b_2}^2}} \tag{3}$$

With $n_1 + n_2 - 4$ degrees of freedom, according to Eq. (11.20) of Armitage et al. (2002). The parameters b_1 and b_2 are the slopes before and after 2050 in each geographical zone, and n_1 and n_2 are the numbers of data before and after 2050, respectively. The test was performed using de-seasonalized monthly values but also with the averages shown in Figures 3c, 4c, 5c, calculated from de-seasonalized data. Both ways gave similar statistical results. We provide here the results using the de-seasonalized monthly values.

The equation for the slope of the regression line, using x as the time variable and y as the DNA active irradiance variable, is:

$$b = \frac{\sum(x - \bar{x})(y - \bar{y})}{\sum(x - \bar{x})^2} \tag{4}$$

The residual mean square for the first group (1960-2049), $s_{b_1}^2$, is estimated as follows:

608 Our calculations according to Eq. 3 show that at the significance level $\alpha = 0.05$, the null hypothesis that the
609 slopes are statistically equal, cannot be rejected for neither the northern, nor the southern high latitudes
610 (>55°), and therefore we cannot conclude that there is any statistically significant difference between the
611 trends in DNA active irradiance before and after 2050 in these two latitude zones. On the other hand, the
612 null hypothesis is rejected for the latitude zone of 50° N–50° S, which means that the alternative hypothesis
613 is accepted, and so the two trends before and after 2050 are statistically different. The statistical results are
614 presented in Table 5.

615 We note here that the statistical test was also applied for the periods before 2050, i.e., the two periods 1960-
616 1999 and 2000-2049, to test if their trends are statistically significant or not. In all latitudes it was found
617 that the regression slope of the period 1960-1999 is not statistically significantly different from the
618 regression slope of the period 2000-2049. As such, it appears that only after the year 2050 there appears to
619 be a statistically significant change in the trends of DNA active irradiance because of the evolution of
620 GHGs and only at latitudes between 50° N and 50° S. At latitudes poleward of 55°, the DNA active
621 irradiance is more likely to continue to decrease due to the increasing ozone trends from the reduction of
622 the concentrations of ODSs.

623 Moreover, we have applied multiple linear regression (MLR) analysis to examine the contribution of ozone
624 and cloud trends to the estimated DNA active irradiance trends after the year 2050. The MLR model was
625 applied to the differences between the two model simulations, ~~RC2 base 04~~REF and ~~SC2 fGHG 01~~FIX,
626 which were estimated from monthly de-seasonalized data (*deseas*). The MLR model is of the following
627 form:

$$deseas\ DNA\ active\ irradiance = a + \beta_{O_3} \cdot deseas\ O_3 + \beta_{cloud} \cdot deseas\ Cloud \tag{7}$$

628 Where, a is the intercept, β_{O_3} is the ozone coefficient and β_{cloud} is the cloud coefficient for the period

629 2050–2099. The regression coefficients and their standard errors are presented in Table 6a. These

630 coefficients were derived from station mean data ~~and from zonal mean data~~, and hence might not be

631 representative for the entire geographical zones. As can be seen, the coefficients β_{O_3} and β_{cloud} are highly

632 statistically significant with small errors in all cases (p-values <0.001). We have used the regression

633 coefficients to determine the part of the DNA active irradiance trends that are caused by trends in total

634 ozone and cloud cover. We have derived the ozone-related DNA active irradiance trend by multiplying the

635 regression coefficient between DNA active irradiance and ozone (β_{O_3}) with the trend in ozone for the

636 period 2050–2099. Accordingly, we derived the respective cloud-related DNA active irradiance trend by

637 multiplying the regression coefficient β_{cloud} with the cloud trend.

638 For the northern high latitude stations (>55° N), we estimate an ozone-related DNA active irradiance trend

639 of about ~~0.96~~ 0.72% per decade, indicating that ~~47~~39% of the DNA active irradiance trend

640 (~~2.04~~ 1.86% per decade) is caused by the trends in ozone. The respective cloud-related DNA active

641 irradiance trend is smaller (~~0.14~~ 0.21% per decade), which means that the cloud trend explains ~~7~~11% of

642 the DNA active irradiance trend. Both parameters account for ~~54~~50% of the predicted DNA active

643 irradiance trend. The remaining part of the DNA active irradiance trend is related to changes in other

644 parameters, as for instance in surface albedo, as is discussed later in Section 3.4.

645 Similar results regarding the contribution of ozone and cloud trends to the predicted DNA active irradiance

646 trend are also found for the southern high latitude stations (>55° S), but not for the stations averaged

647 between 50° N and 50° S. The results are summarized in Table 6b. For the southern high latitude stations

648 (>55° S), the ozone-related DNA active irradiance trend is −0.57% per decade and the cloud-related DNA

649 active irradiance trend is +0.07% per decade. As such, ~59% of the DNA active irradiance trend (−0.96%

650 per decade) is explained by ozone, and ~7% is explained by clouds.

651 For stations averaged between 50° N–50° S, we estimate that the ozone-related DNA active irradiance trend

652 is +0.27% per decade, and the cloud-related DNA active irradiance trend is +0.33% per decade. The

653 contribution of changes in cloudiness is larger than the contribution of changes in ozone (~41% compared

654 to ~33%, respectively), and therefore, our findings support the previous results by Eleftheratos et al. (2020),

655 who analyzed a smaller number of GB stations between 50° N–50° S than those used here.

3.4   Changes in surface albedo and relation to DNA active irradiance

657 In the previous section we showed that DNA active irradiance will continue to decrease after the year 2050

658 at high latitudes as a result of ozone change rather than cloud cover change. Another parameter affecting

659 the solar UV variability at high latitudes is surface albedo (Weihs et al., 1999; Nichol et al., 2003;

660 Weatherhead et al., 2005; Gröbner, 2012; Bais et al., 2019). In this respect, changes in surface albedo are

661 expected to affect the long-term variability of surface UV-B irradiance. Figure 6 shows the changes in

662 surface albedo simulated with the EMAC CCM at the two stations, Barrow in Alaska and Palmer in

663 Antarctica. More specifically the figure shows the differences between the two model simulations, the one
664 with increasing GHGs (~~RC2 base 04~~REF) and the one with fixed GHGs (~~SC2 fGHG 01~~FIX), in order to
665 account also for the effect of increasing GHGs on surface albedo changes according to the methodology
666 applied in Section 3.2. The results refer to the summer seasons of the two hemispheres, where there is
667 sufficient sunlight in the Arctic and the Antarctic. Table 7 summarizes the trends in the differences between
668 the two model simulations, ~~RC2 base 04~~REF and ~~SC2 fGHG 01~~FIX, for the DNA active irradiance, total
669 ozone, cloud cover and surface albedo at Barrow (Alaska) and Palmer (Antarctica) for the periods 1960–
670 1999, 2000–2049 and 2050–2099. While variations in surface albedo are certainly of primary importance
671 for high-latitude sites, they can play a non-negligible role even at mid-latitudes. However, they were not
672 analyzed here.

673 From Figure ~~6~~7 it is clear that surface albedo decreases significantly by the end of the 21st century in view
674 of the increasing GHG emissions. The decreases in surface albedo (Table 7) are larger in Barrow (Alaska)
675 than Palmer (Antarctica). The trend for Barrow is qualitatively consistent with the conclusion by Bernhard
676 (2011), showing that the ground at Barrow is covered by snow later and later at the start of winter. We also
677 note that both, Barrow and Palmer, are coastal sites and are heavily affected by local conditions (e.g., how
678 far sea ice gets to the station), which may not be simulated correctly. Therefore, we point out that the
679 evolution of albedo at the two stations shown in Figure ~~6~~7 is representative for regional changes but may
680 not accurately reflect changes at the exact location of these stations.

681 To assess the impact of the albedo changes on UV variability, we used surface albedo as additional
682 explanatory variable in the MLR model of Eq. (7). We determined an additional regression coefficient,
683 namely β_{albedo}, which explains the effect of albedo change on DNA active irradiance change at the two
684 stations under study, Barrow and Palmer. We estimated an albedo-related DNA active irradiance trend, in
685 the same way as described above, by multiplying the coefficient β_{albedo} with the trend in albedo differences
686 between the two model simulations.

687 For Barrow, we estimate an ozone-related DNA active irradiance trend of about −0.87% per decade for the
688 period 2050–2099, indicating that ~41% of the DNA active irradiance trend (−2.14% per decade) is caused
689 by trends in ozone. The respective cloud-related DNA active irradiance trend is about −0.49% per decade,
690 which means that the cloud trend explains ~23% of the DNA active irradiance trend. The surface albedo-
691 related DNA radiation trend is about −0.45% per decade, explaining ~21% of the DNA active irradiance
692 trend in the period 2050-2099. The model suggests that all parameters together explain ~85% of the DNA
693 active irradiance trend, which however may not be such an unbiased result. This is because the effects of
694 clouds and albedo are not independent, as assumed in the regression equation. For 100% albedo and non-
695 absorbing clouds, clouds would barely attenuate UV radiation. For actual albedo and cloud conditions,
696 clouds do attenuate, but the effect is greatly reduced by surface albedo because of multiple reflections
697 between surface and cloud (Nichol et al., 2003).

698 At Palmer, the trends are smaller. The ozone-related DNA active irradiance trend is −0.46% per decade, the
699 cloud-related DNA active irradiance trend is 0.43% per decade, and the albedo-related DNA active
700 irradiance trend is −0.31% per decade. These trends together determine the small negative trend, which is
701 predicted for the DNA active UV irradiance in the period 2050–2099 of about −0.33% per decade.

702 The above calculations indicate that the impact of albedo trends on DNA active irradiance trends due to the
703 continuous increase of GHGs until the end of the 21st century is important and should not be ignored when
704 studying the long-term changes of DNA active radiation reaching the ground. The model simulations at
705 Barrow and Palmer suggest that the surface albedo changes might be larger at Barrow than Palmer
706 according to Table 7. The model simulations also suggest that the northern high latitudes might experience
707 larger changes in surface albedo than the southern high latitudes in the period 2050–2100 (Appendix C,
708 Figures C1 and C2).

709 In order to better represent the northern and southern high latitudes, we also applied the MLR model to the
710 large-scale zonal means of 55º – 75º N and 55º – 75º S. For the northern high latitude zone, the findings are
711 in the same direction as those found for Barrow. We estimate that ~31% of the DNA active irradiance trend
712 is determined by the trend in ozone, and that ~14% and ~32% of the DNA active radiation trend are
713 explained by trends in clouds and surface albedo, respectively. For the southern high latitude zone, we
714 estimate that the largest part of the DNA active irradiance trend is determined by the trend in ozone, and
715 that the contributions of cloud and albedo trends are small.

716 **4 Summary and Conclusions**

717 We have studied changes in ozone and, DNA active irradiance and cloud cover due to the evolution of
718 greenhouse gas concentrations in the near global mean (50° N–50° S) and in the northern and southern high
719 latitudes, using the EMAC CCM simulations from 1960 to 2100.

720 The model simulations have been evaluated against ground-based UV irradiance measurements, satellite
721 ozone observations from SBUV (v8.7) and satellite cloud fraction data from MODIS/Terra for the period
722 2000–2018. The evaluation results can be summarized as follows:

723 • Simulations of total ozone with specified dynamics (RC1SD-base-10 and SC1SD-base-02HIS-SD)
724 reproduce extremely well the variability of total ozone in the northern and southern high latitudes
725 for the periods 1979–2013 and 2000–2018, respectively. The correlation analysis results between
726 EMAC SC1SD-base-02HIS-SD simulation and SBUV (v8.7) satellite ozone de-seasonalized data
727 are: Northern high latitudes (2 3 station mean), R = +0.908+0.899, p-value <0.0001; Southern
728 high latitudes (4 station mean), R = +0.892, p-value <0.0001; 50º N–50º S (13 station mean), R =
729 +0.894, p-value <0.0001.
730 • The respective simulations of DNA active irradiance correlate quite well with ground-based UV
731 measurements, as follows: Northern high latitudes (2 3 station mean), R = +0.518+0.504, p-value

<0.0001; Southern high latitudes (4 station mean), R = +0.746, p-value <0.0001; 50º N–50º S (13 station mean, R = +0.499, p-value <0.0001).

- Evaluation of cloud cover simulations against MODIS/Terra cloud fraction data gave good correlations as follows: Northern high latitudes (2 3 stations mean), R = +0.480+0.453, p-value <0.0001; Southern high latitudes (4 station mean), R = +0.485, p-value <0.0001; 50º N–50º S, R = +0.703, p-value <0.0001.

Between 50º N–50º S, the DNA-damaging UV radiation is expected to decrease until 2050 and to increase thereafter. This increase is associated with expected decreases in cloud cover and insignificant trends in total ozone, as it was shown previously by Eleftheratos et al. (2020). Our study however expands the previous work by adding more stations in low and mid-latitudes and by including estimates from high latitude stations with long-term measurements of UV irradiance.

In contrast to the predictions for 50º N–50º S, we estimate that DNA active irradiance will continue to decrease after the year 2050 in the northern and southern high latitudes (>55º) due to increasing ozone. More specifically, for the northern high latitude stations we estimate that total ozone will increase by 2.41.8 ± 0.90.8% from 2050 to 2100, DNA active irradiance will decrease by 10.68.2 ± 3.73.8% and that cloud cover will increase insignificantly by 1.31.4 ± 2.01.3%. Similarly, in the southern high latitude stations, total ozone is estimated to increase by 4.2 ± 2.1% from 2050 to 2100, DNA active irradiance is estimated to decrease by 4.8 ± 2.9% and cloud cover will decrease insignificantly by 1.1 ± 1.7%.

The statistical results have been confirmed by statistical tests. Statistical comparisons of the regression slopes before and after 2050 in the northern and southern high latitude stations under study showed that there are no statistically significant different trends in DNA active irradiance before and after that year. On the other hand, between 50º N–50º S the trends before and after 2050 were found to be statistically significantly different at the 0.05 significance level. The test confirmed the statistical result that DNA active irradiance will reverse sign and become positive after 2050 at stations between 50º N–50º S mainly due to cloud cover and ozone changes associated with climate change, something that is likely not to happen at high latitudes, where the DNA-damaging UV-B radiation is projected to continue its downward trend after 2050 mainly due to the continued increase of ozone from the reduction of ODSs. In addition, it should be mentioned, that the enhanced GHG concentrations will cool the stratosphere and therefore the stratospheric ozone content (especially in the middle and upper stratosphere) is expected to increase because the ozone depleting reactions (homogeneous gas phase reactions) will be getting slower. From Dhomse et al. (2018) we know that the (future) Arctic and the Antarctic stratosphere are developing differently in spring. In particular, the Arctic region is indicating a stronger reaction on enhanced GHG concentrations (most likely due to the dynamic feedbacks in the northern hemisphere, i.e., related to the planetary wave activity).

We clarify here that our findings for the high latitudes refer to the summer periods and not to the seasons when ozone depletion occurs, for which it has been shown that climate change will favor large spring loss

768   of Arctic column ozone in connection with extraordinary (persistent) cold stratospheric winters (with low
769   planetary wave activity) in the future (von der Gathen et al., 2021). The best agreement between the ~~RC2 base 04~~REF simulation results and satellite measurements during the period of ozone depletion was found
770
771   for the southern high latitudes. The ~~RC2 base 04~~REF simulation (full chemistry and increasing GHGs
772   according to RCP-6.0) seems to underestimate the observed ozone depletion of the 1980s and 1990s for the
773   near global mean (50° N–50° S) and at high latitudes of the Northern Hemisphere. This might at least partly
774   be caused by not considering all ODSs, but only a subset (only CFC-11 and CFC-12 were considered).
775   Despite this feature, the simulated ozone declines during 1979–1999 and the minimum ozone values
776   calculated by the model in the 1990s for the northern mid- and high latitudes, are qualitatively in line with
777   the satellite ozone observations.

778   Also, our analysis suggests that clouds might stay constant over the Arctic, while other models predict that
779   cloud cover in the Arctic will increase during the next decades due to enhanced evaporation of water vapor
780   by the sea-ice decrease. Our estimates, however, refer to two sites in the Arctic and not to the entire Arctic
781   Ocean. As such, our results should be considered representative of the land sites under study and not of the
782   entire Arctic or Antarctic regions. In addition, we cannot reliably evaluate the projection of cloud cover
783   over time, using MODIS observations for a relatively short period. So, in the end we must trust that the
784   physics coded in the model is correct. Hence, verification of our results using independent CCMs would be
785   highly desired. We conducted a separate analysis on total cloud cover variability and trends through the 21st
786   century, using the available simulations from the CCMI-1 REF-C2 set, which showed that the EMAC CCM
787   results fall well within the range of uncertainty (i.e., $\pm 2\sigma$), close to the ensemble average ($\pm 1\sigma$).

788   Moreover, we applied a multiple linear regression model to examine the contribution of ozone and cloud
789   trends to the estimated DNA active irradiance trends after the year 2050. The model was applied to the
790   differences between the two model simulations, ~~RC2 base 04~~REF and ~~SC2 fGHG 01~~FIX. It was found that
791   ozone is the primary contributor accounting for about ~50% of the predicted trends in DNA active
792   irradiance after 2050 both in the northern and in the southern high latitude stations.

793   The impact of surface albedo on DNA active irradiance trends due to the evolution of GHGs (RCP-6.0) has
794   been examined at two stations, Barrow in the Arctic, and Palmer in the Antarctic. The model simulations
795   suggest that declining trends in surface albedo are larger at Barrow than Palmer. The driving force for the
796   decrease in Arctic surface albedo is by 70% the decrease in snow cover fraction over the Arctic land and
797   sea-ice due to the increase in surface air temperature and decrease in snowfall (Zhang et al., 2019).

798   Unlike the Arctic sea-ice, which has consistently declined over the past four decades, the Antarctic sea-ice
799   has shown little change (increase) from 1979 to 2015 but large regional and temporal variability (Maksym,
800   2019). A rapid decline in 2015–2018, far exceeding the decreasing rates seen in the Arctic (Parkinson,
801   2019), may have foreboded future changes in Antarctic sea-ice (Eayrs et al., 2021). The observed decline
802   lowered the region's surface albedo, highlighting the importance of Antarctic sea-ice loss to the global
803   snow and ice albedo feedback (Riihelä et al., 2021). This sea-ice reduction probably resulted from the

804 interaction of a decades-long ocean warming trend and an early spring southward advection of atmospheric
805 heat, with an exceptional weakening of the Southern Hemisphere mid-latitude westerlies in late spring
806 (Eayrs et al., 2021). Obviously, such abrupt declines cannot be predicted by the present-day model
807 simulations. This is because the mechanisms for the Antarctic sea-ice variations are not yet well understood
808 and future predictions are highly uncertain.

809 IPCC (2021) concluded that there has been no significant trend in Antarctic sea-ice area from 1979 to 2020,
810 due to regionally opposing trends and large internal variability. In the Bellingshausen and Amundsen Seas,
811 however, the observed sea-ice has shown decreasing trends (Maksym, 2019; Parkinson, 2019; Eayrs et al.,
812 2021). Our estimates for Palmer, which is located at the coast of the Bellingshausen Sea, shows a negative
813 trend in surface albedo from 1979 to 2020, which is in line with the negative trends in sea-ice observed in
814 Bellingshausen and Amundsen Seas. The ~~RC2-base-04~~REF simulation shows that the surface albedo at
815 Palmer will continue to decrease until 2100. This result should be considered representative of the Palmer
816 station and its surroundings, and not of the entire Antarctic region.

817 The key findings presented in this study are that model and measurements agree fairly well, giving support
818 to the simulations of the future scenarios. Cloud cover is generally decreasing, leading to increased solar
819 radiation, apart from the high latitudes, where no significant changes are observed. Total ozone shows an
820 increasing trend from the reduction of ODSs, while a decrease is observed after 2050 on a near-global scale
821 due to the increase of GHGs. UV trends are a combination of changes in ozone and cloud cover, while at
822 high latitudes, decreased surface albedo in the second half of the century has a significant influence on the
823 surface UV radiation.

824 The above findings were based on the analysis of model simulations from 3 stations in the northern high
825 latitudes, 4 stations in the southern high latitudes, and 13 stations in the near-global mean with
826 contributions mainly from the mid-latitudes. A separate analysis using zonal means showed that the results
827 from the analysis of the model data averaged over geographical zones are qualitatively in the same
828 direction with those from the station averages. All simulations were based on a single CCM, and therefore,
829 verification of the results from simulations of other models would be quite useful.

830

Appendix A Qualitative evaluation of free running CCM simulations against simulations with
831
832 **specified dynamics**

833 In this appendix, we compare the free running ozone simulation ~~RC2-base-04~~REF, with the SD simulation
834 RC1SD-base-10 and SBUV satellite ozone data (v8.7). The simulation with specific dynamics RC1SD-
835 base-10 covers the period January 1979 – December 2013. The simulation has been used in recent
836 assessments reports for stratospheric ozone studies (e.g., LOTUS, 2019). In addition to the nudging towards
837 ECMWF ERA-Interim (Dee at al., 2011) reanalysis data (for details about the nudging setup see Jöckel et
838 al., 2016) the simulation uses also sea surface temperatures and sea-ice concentrations from the ERA

839   Interim reanalysis data. Here, we use the SD simulation (RC1SD-base-10) to show that the free running

840   simulation (~~RC2-base-04~~REF) is capable to qualitatively reflect the negative ozone trends of the 1980s and

841   1990s. The reason for quoting the RC1SD-base-10 simulation is because the ~~SC1SD-base-02~~HIS-SD

842   simulation that is used in section 3.1 does not go back in time before 2000, and therefore we cannot

843   qualitatively evaluate our free running simulation before 2000. We also appose here the SD simulation

844   (~~SC1SD-base-02~~HIS-SD), which covers the period January 2000 – July 2018. This is useful and helpful to

845   classify the results of the free running model system concerning the quality with respect to the SD

846   simulation and the observations of the stations, and it serves as a "bridge" from the observations via the SD

847   simulation results, to the results of the (longer-term) free-running model simulation.

848   Figure A1 shows the comparison between the simulations and SBUV data. Obviously, the RC1SD-base-10

849   simulation (period 1979–2013) compares much better with the SBUV data than the ~~RC2-base-04~~REF

850   simulation. The same also holds for the ~~SC1SD-base-02~~HIS-SD simulation (period 2000–2018). This is

851   expected since the SD simulation uses reanalyzed meteorology, whereas the free running simulation has its

852   own meteorological/synoptical sequence. For comparison with the fixed GHG simulation, we need to

853   switch to the pair of free running simulations. And the question is, if the evaluation (comparison with

854   observations) also hold for the ~~RC2-base-04~~REF simulation, which is the basis for the comparison with the

855   fixed GHG simulation (~~SC2-fGHG-01~~FIX). In the case of free running simulations, the evaluation is only

856   possible for the trends and for the amplitude of the year-to-year variability, but not for the sign of the

857   anomaly in a given nominal year and/or month. Figure A1 shows that the free running simulation (~~RC2-~~

858   ~~base-04~~REF) reflects correctly the negative ozone trends of the past, seen in the observations and in the SD

859   simulation, and is therefore suitable for comparison with the fixed GHG simulation.

860

861

862
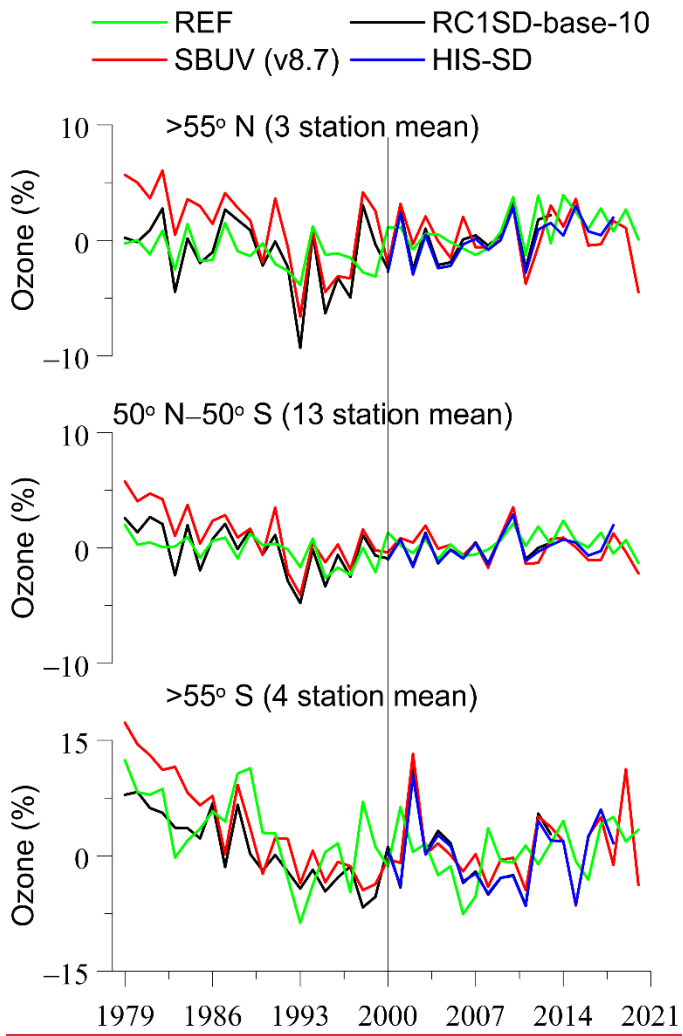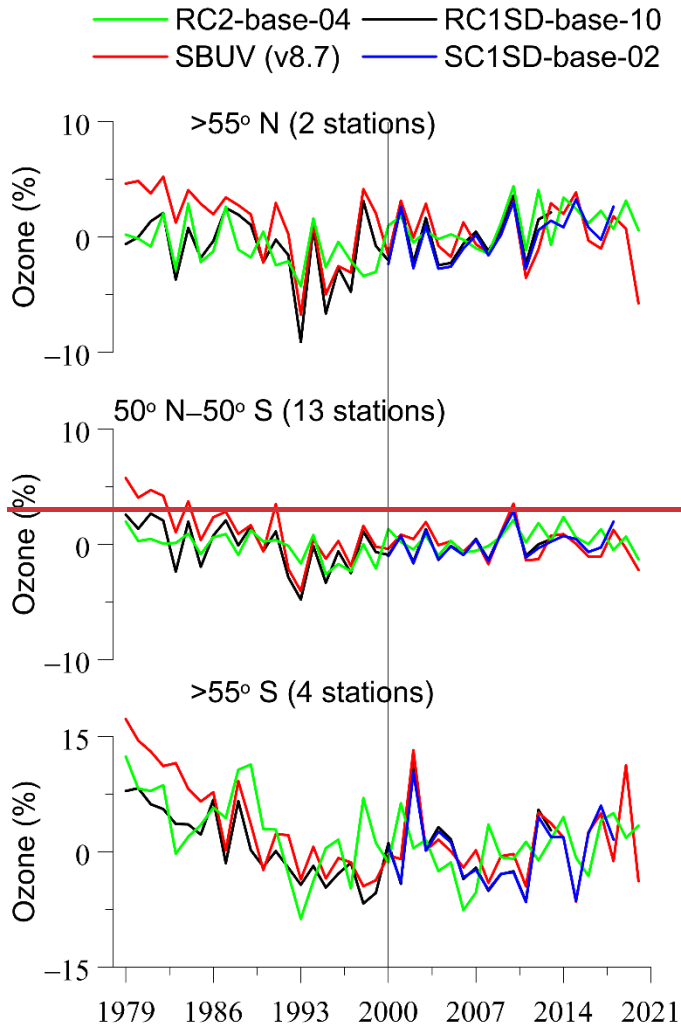
Figure A1. Comparison of ~~REF~~RC2-base-04 (free running simulation; green line) with RC1SD-base-10 (SD simulation for 1979–2013; black line), ~~SC1SD-base-02~~HIS-SD (SD simulation for 2000–2018; blue line) and SBUV (v8.7) satellite measurements (red line) for ~~2~~3 stations higher than 55° N (upper plot), 13 stations between 50° N–50° S (middle plot) and 4 stations higher than 55° S (lower plot). The vertical line has been put in the year 2000. The y-axis shows yearly averaged total ozone data (in %) calculated from de-seasonalized monthly data. The monthly data were de-seasonalized relative to the long-term monthly mean (2000–2018) and were expressed in %. For the northern high latitude stations, the annual average refers to the average of monthly anomalies from March to September, and for the southern high latitude stations, it refers to the average of monthly anomalies from September to March. For the stations between 50° N–50° S we used all months to calculate the annual average.

873

874 **Appendix B Model simulations of zonally averaged cloud cover between 50º and 80º N**

875 Figure B1 shows the changes of the zonally averaged cloud cover based on ~~RC2 base 04~~REF (RCP-6.0)

876 and ~~SC2 fGHG 02~~FIX simulations, and their differences (~~RC2 base 04~~REF minus ~~SC2 fGHG 01~~FIX), per

877 10-degree latitude zones from 50º to 80º N. For the period 1960 to 2100, the changes in cloud cover due to

878 the evolution of GHGs (RCP-6.0) are presented in Table B1. The same picture with increasing trends as we

879 move northward of 50º N is also found for the period 2050 to 2100.

880

881 **Table B1.** Changes in zonal mean cloud cover between 50º and 80º N due to the evolution of GHGs (RCP-

882 6.0), for the periods 1960–2100 and 2050–2100.

	1960–2100			2050–2100		
	% Change	p-value	N	% Change	p-value	N
50º–60º N	0.9	< 0.0001	140	0.3	0.56064	50
60º–70º N	2.7	< 0.0001	140	0.7	0.27113	50
70º–80º N	4.3	< 0.0001	140	1.9	0.00012	50

883
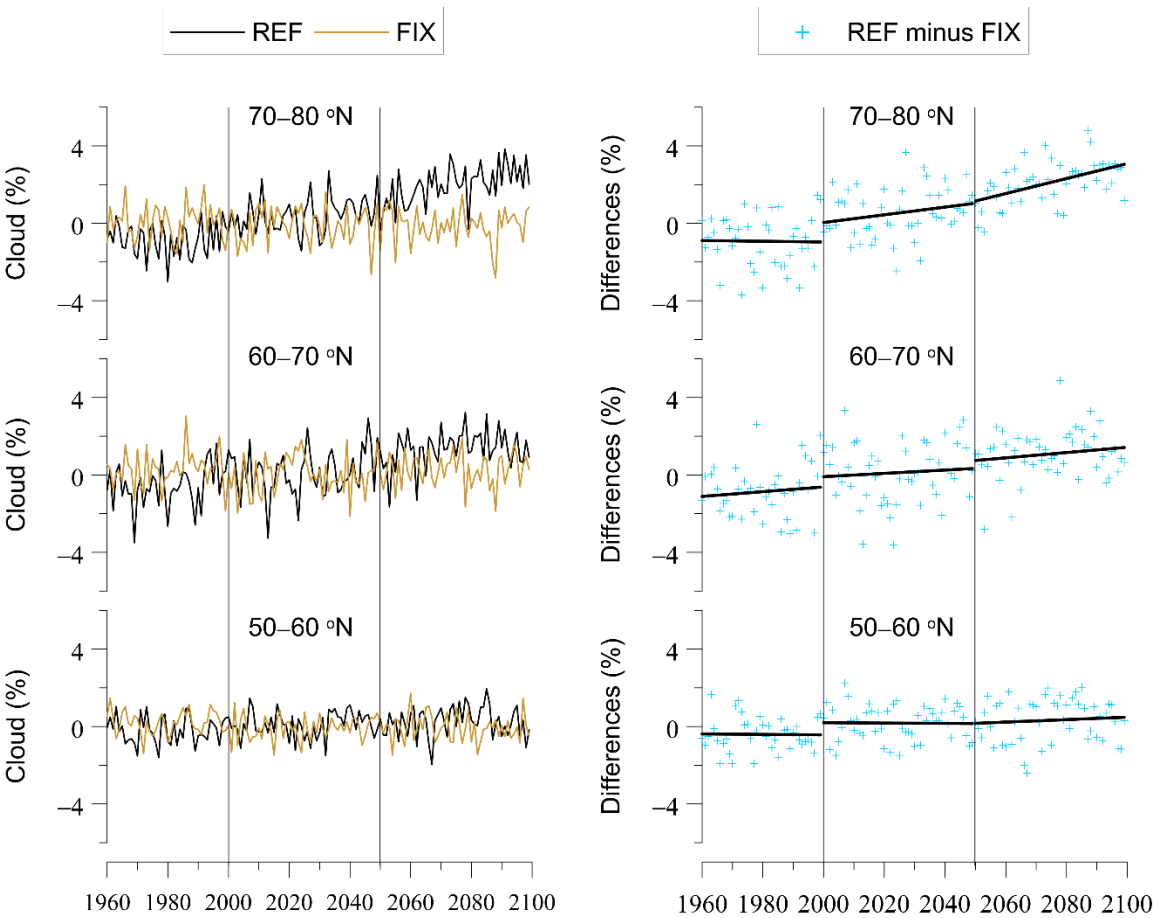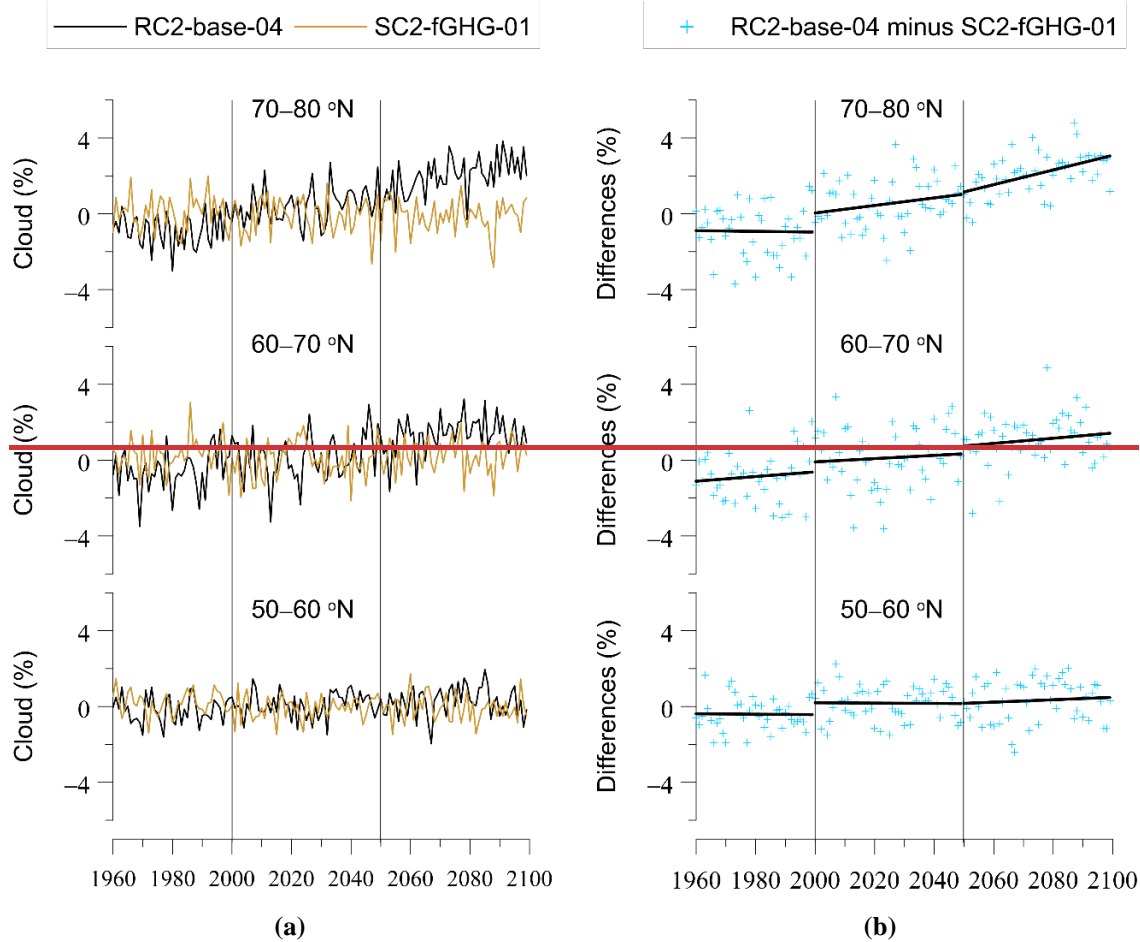
884 **Figure B1.** EMAC CCM projections of zonal mean cloud cover for 10-degree latitude zones (50º–60º N,

885 60º–70º N, 70º–80º N), based on simulations with increasing and fixed GHGs mixing ratios. **(a)** ~~RC2 base~~

886 ~~04~~REF is the simulation with increasing GHGs according to RCP-6.0. ~~SC2 fGHG 01~~FIX is the simulation

887 with fixed GHGs emissions at 1960 levels. **(b)** Difference between the two model simulations, as an

888 indicator of the impact of increasing GHGs. The y-axis in the left figure (a) shows yearly averaged cloud

889 cover data (in %) calculated from de-seasonalized monthly data. The monthly data were de-seasonalized

890 relative to the long-term monthly mean (1990–2019) and were expressed in %. For the northern high

891 latitudes, the annual average refers to the average of monthly anomalies from March to September.

892

893 **Appendix C Model simulations of zonally averaged surface albedo between 50º and 80º N, and 50º**
894 **and 80º S**

895 Figure C1 shows the changes in zonally averaged surface albedo based on ~~RC2 base 04~~REF (RCP-6.0) and

896 ~~SC2 fGHG 02~~FIX simulations, and their differences (~~RC2 base 04~~REF minus ~~SC2 fGHG 01~~FIX), per 10-

897 degree latitude zones between 50º N and 80º N. Figure C2 shows the respective changes between 50º S and

898   80º S. The changes in surface albedo due to the evolution of GHGs (RCP-6.0) between 50º and 80º N, and

899   50º and 80º S, are summarized in Table C1.

900

901   **Table C1.** Changes in zonal mean surface albedo due to the evolution of GHGs (RCP-6.0) between 50º and

902   80º N, and 50º and 80º S, for the periods 1960–2100 and 2050–2100.

North	1960–2100			2050–2100		
	% Change	p-value	N	% Change	p-value	N
50º–60º N	–21.0	< 0.0001	140	–8.9	< 0.0001	50
60º–70º N	–18.3	< 0.0001	140	–9.2	< 0.0001	50
70º–80º N	–41.3	< 0.0001	140	–15.1	< 0.0001	50

903

South	1960–2100			2050–2100		
	% Change	p-value	N	% Change	p-value	N
50º–60º S	–12.5	< 0.0001	140	–3.7	0.00299	50
60º–70º S	–22.5	< 0.0001	140	–3.8	0.00298	50
70º–80º S	–6.1	< 0.0001	140	–1.3	0.00132	50

904

905
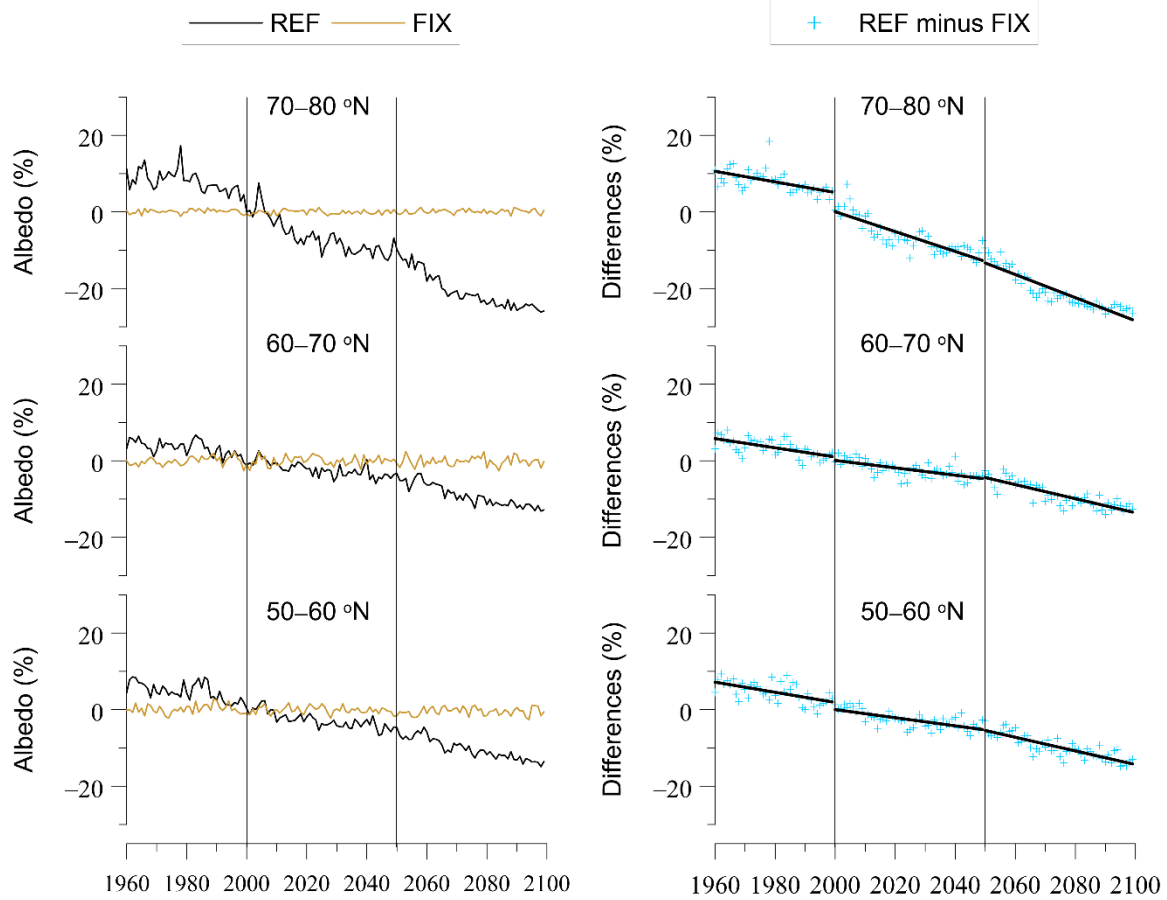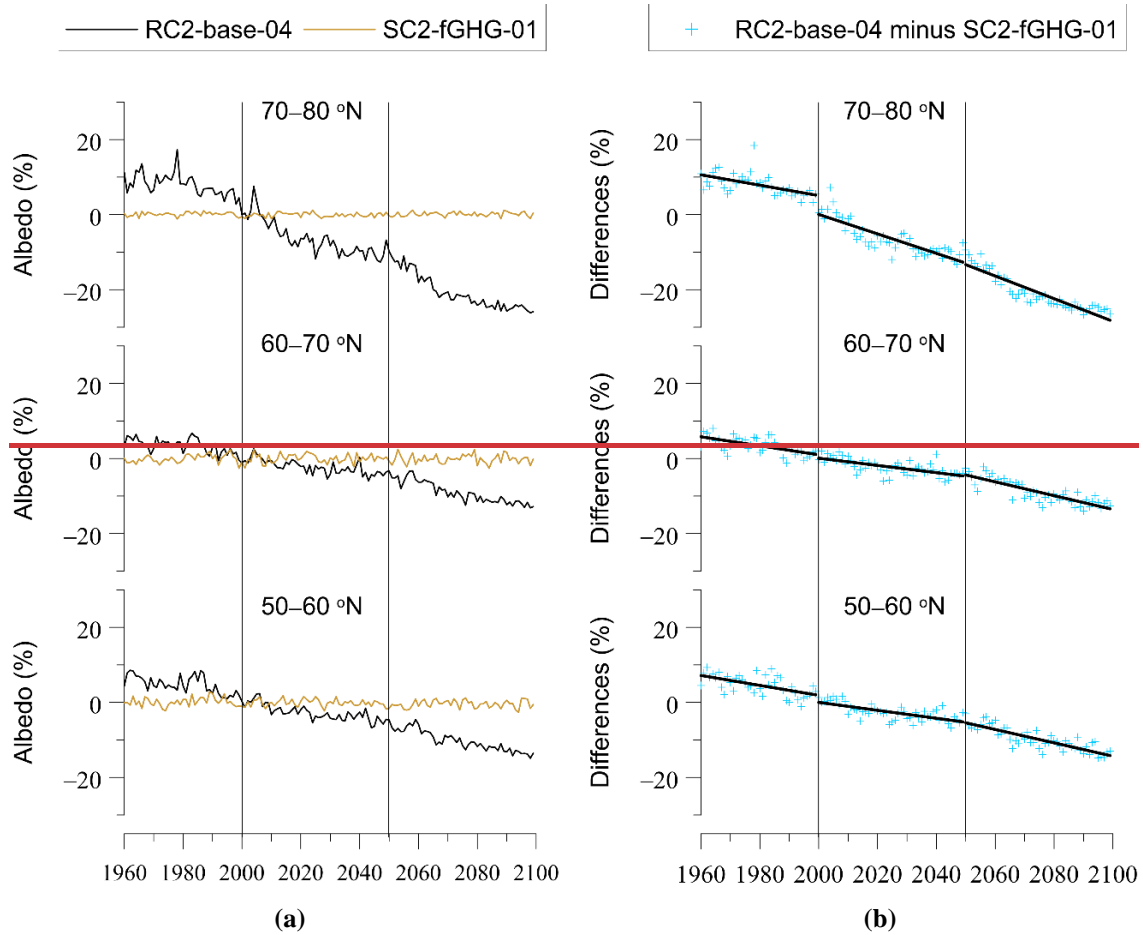
Figure C1. EMAC CCM projections of zonal mean surface albedo for 10-degree latitude zones (50-60º N, 60-70º N, 70-80º N), based on simulations with increasing and fixed GHGs mixing ratios. **(a)** ~~RC2 base-04~~REF is the simulation with increasing GHGs according to RCP-6.0. ~~SC2-fGHG-01~~FIX is the simulation with fixed GHGs emissions at 1960 levels. **(b)** Difference between the two model simulations, as an indicator of the impact of increasing GHGs. The y-axis in the left figure (a) shows yearly averaged surface albedo data (in %) calculated from de-seasonalized monthly data. The monthly data were de-seasonalized relative to the long-term monthly mean (1990–2019) and were expressed in %. For the northern high latitudes, the annual average refers to the average of monthly anomalies from March to September.

(a)
(b)
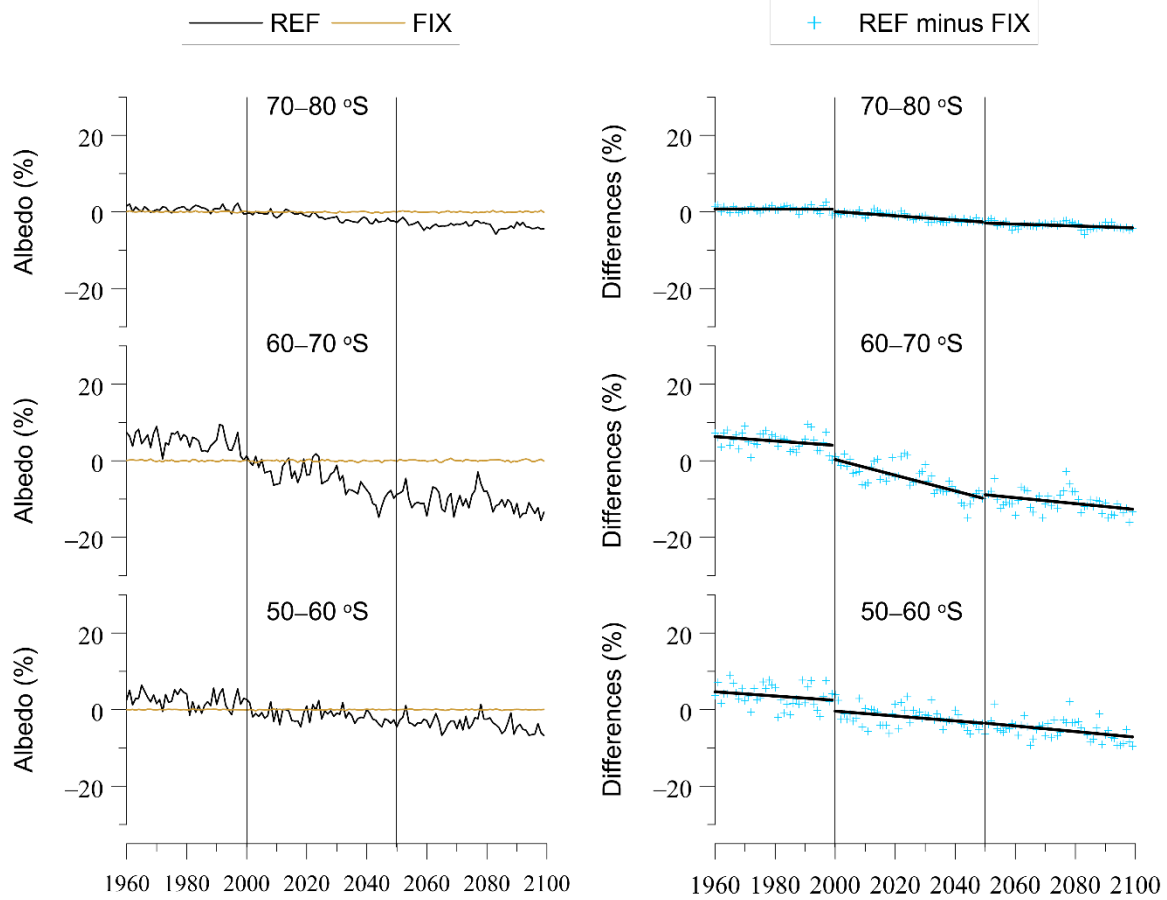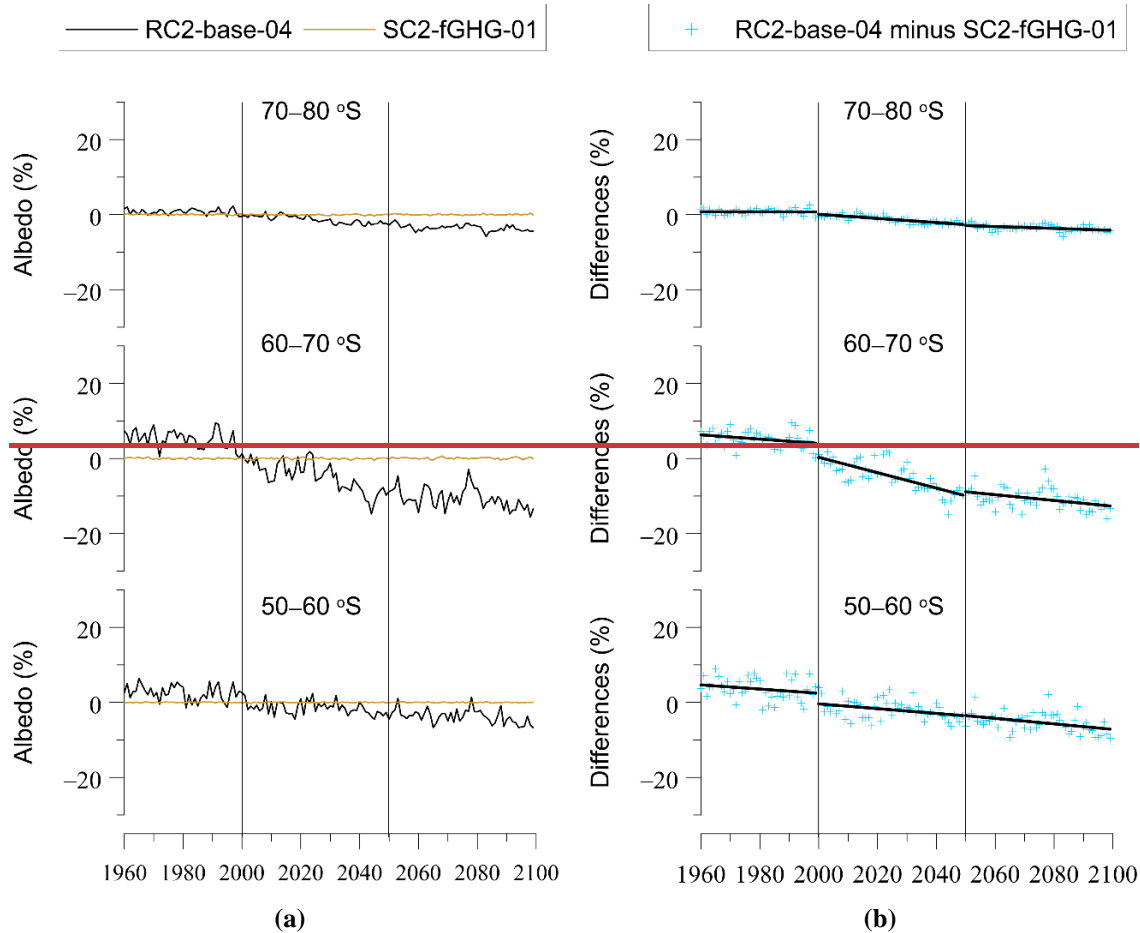
Figure C2. Same as Figure C1 but for 50-60º S, 60-70º S, and 70-80º S. The y-axis in the left figure (a) shows yearly averaged surface albedo data (in %) calculated from de-seasonalized monthly data. The monthly data were de-seasonalized relative to the long-term monthly mean (1990–2019) and were expressed in %. For the southern high latitudes, the annual average refers to the average of monthly anomalies from September to March.

Data Availability: The UV irradiance data are archived at the NDACC data repository, https://www-air.larc.nasa.gov/pub/NDACC/PUBLIC/stations/~~ftp://ftp.cpc.ncep.noaa.gov/ndacc/station/~~ (last access ~~27 July 2021~~4 September 2022). The SBUV (v8.~~6~~7) satellite ozone data are available at https://acd-ext.gsfc.nasa.gov/Data_services/merged/previous_mods.html (last access ~~18 March 2021~~4 September 2022). The MODIS/Terra v6.1 satellite cloud fraction monthly mean data (MOD08_M3 v6.1) are available at

https://giovanni.gsfc.nasa.gov/giovanni/#service=TmAvMp&starttime=&endtime=&data=MOD08_M3_6_1_Cloud_Fraction_Mean_Mean (last access ~~6 April 2021~~4 September 2022).

Author Contribution: K.E. and C.Z. conceptualized the study. A.B., G.B., D.K., S.S., B.L., C.B., F.A., S.S. ~~and~~, H.D.., and K.L. provided ground-based UV irradiance data. K.E., D.K., I.F. and K.T. analysed data. M.D. and P.J. provided the EMAC model simulations. J.K. and K.D. processed the model simulations. The manuscript was originally prepared by K.E. and was reviewed with comments and corrections from all co-authors.

Competing interests: One co-author (MD) is coordinator, and one co-author (IP) is co-organizer of the special issue "Atmospheric ozone and related species in the early 2020s: latest results and trends (ACP/AMT inter-journal SI), 2021".

Acknowledgments: The research work was partially funded by the Hellenic Foundation for Research and Innovation (H.F.R.I.) under the "First Call for H.F.R.I. Research Projects to support Faculty members and Researchers and the procurement of high-cost research equipment grant" (Atmospheric parameters affecting SPectral solar IRradiance and solar Energy (ASPIRE), Project Number: 300). We acknowledge support by the project "PANhellenic infrastructure for Atmospheric Composition and climatE change" (MIS 5021516) which is implemented under the Action "Reinforcement of the Research and Innovation Infrastructure", funded by the Operational Programme "Competitiveness, Entrepreneurship and Innovation" (NSRF 2014-2020), and co-financed by Greece and the European Union (European Regional Development Fund). The research contributes to the National Network for Climate Change and its Impact – CLIMPACT. We acknowledge the project Long-term Ozone Trends and Uncertainties in the Stratosphere (LOTUS) and the Mariolopoulos-Kanaginis Foundation for the Environmental Sciences. The EMAC simulations have been performed at the German Climate Computing Centre (DKRZ) through support from the Bundesministerium für Bildung und Forschung (BMBF). DKRZ and its scientific steering committee are gratefully acknowledged for providing the HPC and data archiving resources for this consortial project ESCiMo (Earth System Chemistry integrated Modelling). Measurements of French spectroradiometers are supported by CNES (French programme TOSCA); the Université de La Réunion and CNRS; the Région Hauts-de-France and the Ministère de l'Enseignement Supérieur et de la Recherche (CPER Climibio); and the European Fund for Regional Economic Development. Technicians at the three French and at the Finnish (Sodankylä) sites are acknowledged for the maintenance and calibration of the instruments. Kaisa Lakkala is supported by the CHAMPS project (grant no. 329225) of the Academy of Finland under the CLIHE programme. We acknowledge the SBUV science team for providing the satellite ozone profiles. NIWA UV spectrometer systems, serial numbers UV3 (Mauna Loa, HI) and UV5 (Boulder, CO) in the USA are owned and operated by NOAA/ESRL/Global Monitoring Division, Boulder CO. They are maintained, calibrated, and operated by NOAA. The final data from both of these instruments are quality controlled and produced by NIWA-Lauder, New Zealand. We thank NIWA and NOAA for the use of their data in this publication. Analyses and visualizations used in this study were produced with the Giovanni online data system, developed and maintained by the NASA GES DISC. We also acknowledge the MODIS mission scientists and associated NASA personnel for the production of the data used in this research

968 effect. We would like to thank the anonymous reviewer for summarizing the key findings which we
969 incorporated at the end of the conclusions.

970 **References**

971 Armitage, P., Berry, G., and Matthews, J. N. S.: Statistical methods in medical research, 4th edition,
972 Blackwell Publishing, ISBN 0-632-05257-0, pp.865, 2002.

973 Bais, A. F., Bernhard, G., McKenzie, R. L., Aucamp, P. J., Young, P. J., Ilyas, M., Jöckel, P., and Deushi,
974 M.: Ozone-climate interactions and effects on solar ultraviolet radiation, Photochem. Photobiol. Sci., 18,
975 602-640, https://doi.org/10.1039/C8PP90059K, 2019.

976 Bais, A. F., McKenzie, R. L., Bernhard, G., Aucamp, P. J., Ilyas, M., Madronich, S., and Tourpali, K.:
977 Ozone depletion and climate change: impacts on UV radiation, Photochem. Photobiol. Sci., 14(1), 19–52,
978 doi:10.1039/c4pp90032d, 2015.

979 Bais, A. F., Tourpali, K., Kazantzidis, A., Akiyoshi, H., Bekki, S., Braesicke, P., Chipperfield, M. P.,
980 Dameris, M., Eyring, V., Garny, H., Iachetti, D., Jöckel, P., Kubin, A., Langematz, U., Mancini, E.,
981 Michou, M., Morgenstern, O., Nakamura, T., Newman, P. A., Pitari, G., Plummer, D. A., Rozanov, E.,
982 Shepherd, T. G., Shibata, K., Tian, W., and Yamashita, Y.: Projections of UV radiation changes in the 21st
983 century: impact of ozone recovery and cloud effects, Atmos. Chem. Phys., 11, 7533–7545,
984 https://doi.org/10.5194/acp-11-7533-2011, 2011.

985 Bais, A. F., and Zerefos C. S.: The effect of changes in ozone on solar UV-B radiation at Reykjavik, SPIE
986 Vol. 2049 Atmospheric Radiation, 263–267, 1993.

987 Bais, A. F., Zerefos, C. S., Meleti, C., Ziomas I. C., and Tourpali, K.: Spectral measurements of solar UVb
988 radiation and its relations to total ozone, SO_2, and clouds, J. Geophys. Res., 98(D3), 5199–5204, 1993.

989 Bernhard, G.: Trends of solar ultraviolet irradiance at Barrow, Alaska, and the effect of measurement
990 uncertainties on trend detection, Atmos. Chem. Phys., 11, 13029–13045, https://doi.org/10.5194/acp-11-
991 13029-2011, 2011.

992 Bernhard, G., Booth, C. R., Ehramjian, J. C., Stone, R., and Dutton, E. G.: Ultraviolet and visible radiation
993 at Barrow, Alaska: Climatology and influencing factors on the basis of version 2 National Science
994 Foundation network data, J. Geophys. Res., 112, D09101, doi:10.1029/2006JD007865, 2007.

995 Bernhard, G., Mayer, B., Seckmeyer, G., and Moise, A.: Measurements of spectral solar UV irradiance in
996 tropical-Australia, J. Geophys. Res. Atmospheres, 102(D7), 8719 – 8730,
997 https://doi.org/10.1029/97JD00072, 1997.

998 Bernhard, G., Neale, R. E., Barnes, P. W., Neale, P. J., Zepp, R. G., Wilson, S. R., Andrady, A. L., Bais, A.
999 F., McKenzie, R. L., Aucamp, P. J., Young, P. J., Liley, J. B., Lucas, R. M., Yazar, S., Rhodes, L. E.,
1000 Byrne, S. N., Hollestein, L. M., Olsen, C. M., Young, A. R., Robson, T. M., Bornman, J. F., Jansen, M. A.

K., Robinson, S. A., Ballaré, C. L., Williamson, C. E., Rose, K. C., Banaszak, A. T., Häder, D.-P., Hylander, S., Wängberg, S.-Å., Austin, A. T., Hou, W.-C., Paul, N. D., Madronich, S., Sulzberger, B., Solomon, K. R., Li, H., Schkowski, T., Longstreth, J., Pandey, K. K., Heikkilä, A. M., and White, C. C.: Environmental effects of stratospheric ozone depletion, UV radiation and interactions with climate change: UNEP Environmental Effects Assessment Panel, update 2019, Photochem. Photobiol. Sci., 19, 542–584, doi:10.1039/d0pp90011g, 2020.

Bernhard, G., and Stierle, S.: Trends of UV Radiation in Antarctica, Atmosphere, 11(8), 795, https://doi.org/10.3390/atmos11080795, 2020.

Bhartia, P. K., McPeters, R. D., Flynn, L. E., Taylor, S., Kramarova, N. A., Frith, S., Fisher, B., and DeLand, M.: Solar Backscatter UV (SBUV) total ozone and profile algorithm, Atmos. Meas. Tech., 6, 2533–2548, https://doi.org/10.5194/amt-6-2533-2013, 2013.

Blumthaler M., and Ambach, W.: Indication of increasing solar ultraviolet-B radiation flux in alpine regions, Science, 248(4952), 206-208, doi: 10.1126/science.2326634, 1990.

Brühl, C., and Crutzen, P. J.: On the disproportionate role of tropospheric ozone as a filter against solar UV-B radiation, Geophys. Res. Lett., 16, 703–706, 1989.

Butchart, N.: The Brewer-Dobson circulation, Rev. Geophys., 52, doi:10.1002/2013RG000448, 2014.

Collins, W. J., Bellouin, N., Doutriaux-Boucher, M., Gedney, N., Halloran, P., Hinton, T., Hughes, J., Jones, C. D., Joshi, M., Liddicoat, S., Martin, G., O'Connor, F., Rae, J., Senior, C., Sitch, S., Totterdell, I., Wiltshire, A., and Woodward, S.: Development and evaluation of an Earth-System model – HadGEM2, Geosci. Model Dev., 4, 1051–1075, doi:10.5194/gmd-4-1051-2011, 2011.

Dee, D. P., Uppala, S. M., Simmons, A. J., Berrisford, P., Poli, P., Kobayashi, S., Andrae, U., Balmaseda, M. A., Balsamo, G., Bauer, P., Bechtold, P., Beljaars, A. C. M., van de Berg, L., Bidlot, J., Bormann, N., Delsol, C., Dragani, R., Fuentes, M., Geer, A. J., Haimberger, L., Healy, S. B., Hersbach, H., Hólm, E. V., Isaksen, L., Kållberg, P., Köhler, M., Matricardi, M., McNally, A. P., Monge-Sanz, B. M., Morcrette, J.-J., Park, B.-K., Peubey, C., de Rosnay, P., Tavolato, C., Thépaut, J.-N., and Vitart, F.: The ERA-Interim reanalysis: configuration and performance of the data assimilation system, Q. J. Roy. Meteor. Soc., 137, 553–597, doi:10.1002/qj.828, 2011.

De Mazière, M., Thompson, A. M., Kurylo, M. J., Wild, J. D., Bernhard, G., Blumenstock, T., Braathen, G. O., Hannigan, J. W., Lambert, J.-C., Leblanc, T., et al. The Network for the Detection of Atmospheric Composition Change (NDACC): History, status and perspectives, Atmos. Chem. Phys., 18, 4935–4964, 2018.

den Outer, P. N., Slaper, H., Kaurola, J., Lindfors, A., Kazantzidis, A., Bais, A. F., Feister, U., Junk, J., Janouch, M., and Josefsson, W.: Reconstructing of erythemal ultraviolet radiation levels in Europe for the past 4 decades, J. Geophys. Res., 115, D10102, doi:10.1029/2009JD012827, 2010.

Dhomse, S. S., Kinnison, D., Chipperfield, M. P., Salawitch, R. J., Cionni, I., Hegglin, M. I., Abraham, N. L., Akiyoshi, H., Archibald, A. T., Bednarz, E. M., et al.: Estimates of ozone return dates from Chemistry-Climate Model Initiative simulations, Atmos. Chem. Phys., 18, 8409–8438, 2018.

Douglass, A., Fioletov, V. (Coordinating Lead Authors), Godin-Beekmann, S., Müller, R., Stolarski, R. S., Webb, A. (Lead Authors), Arola, A., Burkholder, J. B., Burrows, J. P., Chipperfield, M. P., Cordero, R., David, C., den Outer, P. N., Diaz, S. B., Flynn, L. E., Hegglin, M., Herman, J. R., Huck, P., Jánosi, I. M., Krzyscin, J. W., Liu, Y., Logan, J., Matthes, K., McKenzie, R. L., Muthama N. J., Petropavlovskikh, I., Pitts, M., Ramachandran, S., Rex, M., Salawitch, R. J., Sinnhuber, B.-M., Staehelin, J., Strahan, S., Tourpali, K., Valverde-Canossa, J., and Vigouroux, C.: Stratospheric ozone and surface ultraviolet radiation. In Scientific assessment of ozone depletion: 2010, Global Ozone Research and Monitoring Project (Report No. 52, Chapter 2). Geneva, Switzerland: World Meteorological Organization, 2011.

Eayrs, C., Li, X., Raphael, M. N., and Holland, D. M.: Rapid decline in Antarctic sea ice in recent years hints at future change, Nat. Geosci., 14, 460 – 464, doi:10.1038/s41561-021-00768-3, 2021.

Eleftheratos, K., Kazadzis, S., Zerefos, C., Tourpali, K., Meleti, C., Balis, D., Zyrichidou, I., Lakkala, K., Feister, U., Koskela, T., Heikkilä, A., and Karhu, J. M.: Ozone and spectroradiometric UV changes in the past 20 years over high latitudes, Atmosphere-Ocean, 53, 117-125, doi:10.1080/07055900.2014.919897, 2015.

Eleftheratos, K., Kapsomenakis, J., Zerefos, C. S., Bais, A. F., Fountoulakis, I., Dameris, M., Jöckel, P., Haslerud, A. S., Godin-Beekmann, S., Steinbrecht, W., Petropavlovskikh, I., Brogniez, C., Leblanc, T., Liley, J. B., Querel R., and Swart, D. P. J.: Possible Effects of Greenhouse Gases to Ozone Profiles and DNA Active UV-B Irradiance at Ground Level, Atmosphere, 11, 228, doi:10.3390/atmos11030228, 2020.

Eyring, V., Lamarque, J.-F., Hess, P., Arfeuille, F., Bowman, K., Chipperfield, M., Duncan, B., Fiore, A., Gettelman, A., Giorgetta, M., Granier, C., Hegglin, M., Kinnison, D., Kunze, M., Langematz, U., Luo, B., Martin, R., Matthes, K., Newman, P., Peter, T., Robock, A., Ryerson, A., Saiz-Lopez, A., Salawitch, R., Schultz, M., Shepherd, T., Shindell, D., Stähelin, J., Tegtmeier, S., Thomason, L., Tilmes, S., Vernier, J.-P., Waugh, D., and Young, P.: Overview of IGAC/SPARC Chemistry-Climate Model Initiative (CCMI) Community Simulations in Support of Upcoming Ozone and Climate Assessments, SPARC Newsletter, 40, 48-46, 2013.

Fountoulakis, I., and Bais, A. F.: Projected changes in erythemal and vitamin D effective irradiance over northern-hemisphere high latitudes, Photochem. Photobiol. Sci., 14(7), 1251–1264, doi:10.1039/c5pp00093a, 2015.

Fountoulakis, I., Bais, A. F., Tourpali, K., Fragkos, K. and Misios, S.: Projected changes in solar UV radiation in the Arctic and sub-Arctic Oceans: Effects from changes in reflectivity, ice transmittance, clouds, and ozone, J. Geophys. Res. Atmos., 119(13), 8073–8090, doi:10.1002/2014JD021918, 2014.

Fountoulakis, I., Diémoz, H., Siani, A. M., Hülsen, G., and Gröbner, J.: Monitoring of solar spectral ultraviolet irradiance in Aosta, Italy, Earth Syst. Sci. Data, 12, 2787–2810, https://doi.org/10.5194/essd-12-2787-2020, 2020a.

Fountoulakis, I., Diémoz, H., Siani, A.-M., Laschewski, G., Filippa, G., Arola, A., Bais, A. F., De Backer, H., Lakkala, K., Webb, A. R., De Bock, V., Karppinen, T., Garane, K., Kapsomenakis, J., Koukouli, M.-E., and Zerefos, C. S.: Solar UV Irradiance in a Changing Climate: Trends in Europe and the Significance of Spectral Monitoring in Italy, Environments, 7(1), https://doi.org/10.3390/environments7010001, 2020b.

Fountoulakis, I., Zerefos, C. S., Bais, A. F., Kapsomenakis, J., Koukouli, M.-E., Ohkawara, N., Fioletov, V., De Backer, H., Lakkala, K., Karppinen, T., Webb, A. R.: Twenty-five years of spectral UV-B measurements over Canada, Europe and Japan: Trends and effects from changes in ozone, aerosols, clouds, and surface reflectivity, Comptes Rendus Geoscience, 350(7), 393–402, https://doi.org/10.1016/j.crte.2018.07.011, 2018.

Gröbner J.: Ultraviolet Radiation: Distribution and Variability. In: Meyers R.A. (eds) Encyclopedia of Sustainability Science and Technology, Springer, New York, NY, https://doi.org/10.1007/978-1-4419-0851-3_453, 2012.

Jöckel, P., Tost, H., Pozzer, A., Kunze, M., Kirner, O., Brenninkmeijer, C. A. M., Brinkop, S., Cai, D. S., Dyro, C., Eckstein, J., et al.: Earth System Chemistry integrated Modelling (ESCiMo) with the Modular Earth Submodel System (MESSy) version 2.51, Geosci. Model Dev., 9, 1153–1200, 2016.

Jones, C. D., Hughes, J. K., Bellouin, N., Hardiman, S. C., Jones, G. S., Knight, J., Liddicoat, S., O'Connor, F. M., Andres, R. J., Bell, C., Boo, K.-O., Bozzo, A., Butchart, N., Cadule, P., Corbin, K. D., Doutriaux-Boucher, M., Friedlingstein, P., Gornall, J., Gray, L., Halloran, P. R., Hurtt, G., Ingram, W. J., Lamarque, J.-F., Law, R. M., Meinshausen, M., Osprey, S., Palin, E. J., Parsons Chini, L., Raddatz, T., Sanderson, M. G., Sellar, A. A., Schurer, A., Valdes, P., Wood, N., Woodward, S., Yoshioka, M., and Zerroukat, M.: The HadGEM2-ES implementation of CMIP5 centennial simulations, Geosci. Model Dev., 4, 543–570, https://doi.org/10.5194/gmd-4-543-2011, 2011.

IPCC, 2021: Summary for Policymakers. In: Climate Change 2021: The Physical Science Basis. Contribution of Working Group I to the Sixth Assessment Report of the Intergovernmental Panel on Climate Change [Masson Delmotte, V., Zhai, P., Pirani, A., Connors, S. L., Péan, C., Berger, S., Caud, N., Chen, Y., Goldfarb, L., Gomis, M. I., Huang, M., Leitzell, K., Lonnoy, E., Matthews, J. B. R., Maycock, T. K., Waterfield, T., Yelekçi, O., Yu R., and Zhou, B. (eds.)]. Cambridge University Press. In Press.

Kerr, J. B., and McElroy, C. T.: Evidence for large upward trends of ultraviolet-B radiation linked to ozone depletion, Science, 262(5136), 1035–1034, doi:10.1126/science.262.5136.1032, 1993.

Kosmopoulos, P. G., Kazadzis, S., Schmalwieser, A. W., Raptis, P. I., Papachristopoulou, K., Fountoulakis, I., Masoom, A., Bais, A. F., Bilbao, J., Blumthaler, M., Kreuter, A., Siani, A. M., Eleftheratos, K., Topaloglou, C., Gröbner, J., Johnsen, B., Svendby, T. M., Vilaplana, J. M., Doppler, L., Webb, A. R.,

Khazova, M., De Backer, H., Heikkilä, A., Lakkala, K., Jaroslawski, J., Meleti, C., Diémoz, H., Hülsen, G., Klotz, B., Rimmer, J., and Kontoes, C.: Real-time UV index retrieval in Europe using Earth observation-based techniques: system description and quality assessment, Atmos. Meas. Tech., 14, 5657–5699, https://doi.org/10.5194/amt-14-5657-2021, 2021.

Krzyścin, J. W. and Baranowski, D. B.: Signs of the ozone recovery based on multi sensor reanalysis of total ozone for the period 1979–2017, Atmospheric Environment, 199, 334–344, https://doi.org/10.1016/j.atmosenv.2018.11.050, 2019.

Lakkala, K., Arola, A., Heikkilä,A., Kaurola, J., Koskela, T., Kyrö, E., Lindfors, A., Meinander, O., Tanskanen, A., Gröbner, J. and Hülsen, G.: Quality assurance of the Brewer spectral UV measurements in Finland. Atmos. Chem. Phys., 8, 3369-3383, 2008.

Kylling, A., Dahlback, A., and Mayer, B.: The effect of clouds and surface albedo on UV irradiances at a high latitude site, Geophys. Res. Lett., 27(9), 1411–1414, 2000.

Lamy, K., Portafaix, T., Josse, B., Brogniez, C., Godin-Beekmann, S., Bencherif, H., Revell, L., Akiyoshi, H., Bekki, S., Hegglin, M. I., Jöckel, P., Kirner, O., Liley, B., Marecal, V., Morgenstern, O., Stenke, A., Zeng, G., Abraham, N. L., Archibald, A. T., Butchart, N., Chipperfield, M. P., Di Genova, G., Deushi, M., Dhomse, S. S., Hu, R.-M., Kinnison, D., Kotkamp, M., McKenzie, R., Michou, M., O'Connor, F. M., Oman, L. D., Pitari, G., Plummer, D. A., Pyle, J. A., Rozanov, E., Saint-Martin, D., Sudo, K., Tanaka, T. Y., Visioni, D., and Yoshida, K.: Clear-sky ultraviolet radiation modelling using output from the Chemistry Climate Model Initiative, Atmos. Chem. Phys., 19, 10087–10110, https://doi.org/10.5194/acp-19-10087-2019, 2019.

Lucas, R. M., Yazar, S., Young, A. R., Norval, M., de Gruijl F. R., Takizawa, Y., Rhodes, L. E., Sinclair, C. A., and Neale, R. E.: Human health in relation to exposure to solar ultraviolet radiation under changing stratospheric ozone and climate, Photochem. Photobiol. Sci., 18, 641, doi: 10.1039/c8pp90060d, 2019.

Madronich, S., McKenzie, R. L., Björn, L. O., and Caldwell, M. M.: Changes in biologically active ultraviolet radiation reaching the Earth's surface, Journal of Photochemistry and Photobiology B: Biology, 46, 5–19, 1998.

Maksym, T.: Arctic and Antarctic sea ice change: contrasts, commonalities, and causes. Annu. Rev. Mar. Sci. 11, 187–213, doi:10.1146/annurev-marine-010816-060610, 2019.

(The HadGEM2 Development Team): Martin, G. M., Bellouin, N., Collins, W. J., Culverwell, I. D., Halloran, P. R., Hardiman, S. C., Hinton, T. J., Jones, C. D., McDonald, R. E., McLaren, A. J., O'Connor, F. M., Roberts, M. J., Rodriguez, J. M., Woodward, S., Best, M. J., Brooks, M. E., Brown, A. R., Butchart, N., Dearden, C., Derbyshire, S. H., Dharssi, I., Doutriaux-Boucher, M., Edwards, J. M., Falloon, P. D., Gedney, N., Gray, L. J., Hewitt, H. T., Hobson, M., Huddleston, M. R., Hughes, J., Ineson, S., Ingram, W. J., James, P. M., Johns, T. C., Johnson, C. E., Jones, A., Jones, C. P., Joshi, M. M., Keen, A. B., Liddicoat, S., Lock, A. P., Maidens, A. V., Manners, J. C., Milton, S. F., Rae, J. G. L., Ridley, J. K., Sellar, A., Senior,

C. A., Totterdell, I. J., Verhoef, A., Vidale, P. L., and Wiltshire, A.: The HadGEM2 family of Met Office Unified Model climate configurations, Geosci. Model Dev., 4, 723–757, https://doi.org/10.5194/gmd-4-723-2011, 2011.

McKenzie, R., Bernhard, G., Liley, B., Disterhoft, P., Rhodes, S., Bais, A., Morgenstern, O., Newman, P., Oman, L., Brogniez, C., et al.: Success of Montreal Protocol Demonstrated by Comparing High Quality UV Measurements with "World Avoided" Calculations from Two Chemistry-Climate Models, Sci. Rep., 9, 12332, 2019.

McKenzie, R. L., Matthews, W. A., and Johnston, P. V.: The relationship between erythemal UV and ozone, derived from spectral irradiance measurements, Geophys. Res. Lett., 18(12), 2269–2272, 1991.

Neale, R. E., Barnes, P. W., Robson, T. M., Neale, P. J., Williamson, C. E., Zepp, R. G., Wilson, S. R., Madronich, S., Andrady, A. L., Heikkilä, A. M., Bernhard, G. H., Bais, A. F., Aucamp, P. J., Banaszak, A. T., Bornman, J. F., Bruckman, L. S., Byrne, S. N., Foereid, B., Häder, D.-P., Hollestein, L. M., Hou, W.-C., Hylander, S., Jansen, M. A. K., Klekociuk, A. R., Liley, J. B., Longstreth, J., Lucas, R. M., Martinez-Abaigar, J., McNeill, K., Olsen, C. M., Pandey, K. K., Rhodes, L. E., Robinson, S. A., Rose, K. C., Schikowski, T., Solomon, K. R., Sulzberger, B., Ukpebor, J. E., Wang, Q.-W., Wängberg, S.-Å., White, C. C., Yazar, S., Young, A. R., Young, P. J., Zhu, L., Zhu, M.: Environmental effects of stratospheric ozone depletion, UV radiation, and interactions with climate change: UNEP Environmental Effects Assessment Panel, Update 2020, Photochemical & Photobiological Sciences, 20, 1–67, https://doi.org/10.1007/s43630-020-00001-x, 2021.

Nichol, S. E., Pfister, G., Bodeker, G. E., McKenzie, R. L., Wood, S. W., and Bernhard, G.: Moderation of cloud reduction of UV in the Antarctic due to high surface albedo, J. Applied Meteorology, 42, 1174–1183, 2003.

Norris, J. R., Allen, R. J., Evan, A. T., Zelinka, M. D., O'Dell, C. W., and Klein, S. A.: Evidence for climate change in the satellite cloud record, Nature, 536, 72–75, doi: 10.1038/nature18273, 2016.

Parkinson, C. L.: A 40-y record reveals gradual Antarctic sea ice increases followed by decreases at rates far exceeding the rates seen in the Arctic. Proc. Natl Acad. Sci. USA, 116, 14414–14423, doi:10.1073/pnas.1906556116, 2019.

Pisoft, P., Sacha, P., Polvani, L. M., Añel, J. A., de la Torre, L., Eichinger, R., Foelsche, U., Huszar, P., Jacobi, C., Karlicky, J., Kuchar, A., Miksovsky, J., Zak, M., and Rieder, H. E.: Stratospheric contraction caused by increasing greenhouse gases, Environ. Res. Lett., 16, 064038, https://doi.org/10.1088/1748-9326/abfe2b, 2021.

Riihelä, A., Bright, R. M., and Anttila, K.: Recent strengthening of snow and ice albedo feedback driven by Antarctic sea-ice loss, Nat. Geosci., 14, 832–836, doi:10.1038/s41561-021-00841-x, 2021.

Sander, R., Jöckel, P., Kirner, O., Kunert, A. T., Landgraf, J., and Pozzer, A.: The photolysis module JVAL-14, compatible with the MESSy standard, and the JVal PreProcessor (JVPP), Geosci. Model Dev., 7, 2653–2662, 2014.

Santer B. D., Wehner, M. F., Wigley, T. M. L., Sausen, R., Meehl, G. A., Taylor, K. E., Ammann., C., Arblaster, J., Washington, W. M., Boyle, J. S., and Brüggemann, W.: Contributions of Anthropogenic and Natural Forcing to Recent Tropopause Height Changes, Science, Vol 301, Issue 5632, 479–483, doi:10.1126/science.1084123, 2003.

Schneider, T., Kaul, C. M., and Pressel, K. G.: Possible climate transitions from breakup of stratocumulus decks under greenhouse warming, Nature Geoscience, 12, 163–167, https://doi.org/10.1038/s41561-019-0310-1, 2019.

Setlow, R. B.: The Wavelengths in Sunlight Effective in Producing Skin Cancer: A Theoretical Analysis, Proc. Nat. Acad. Sci. USA, 71(9), 3363–3366, https://doi.org/10.1073/pnas.71.9.3363, 1974.

Solomon, S., Ivy, D. J., Kinnison, J., Mills, M. J., Neely, R. R., and Schmidt, A.: Emergence of healing in the Antarctic ozone layer, Science 353, 269–274. https://doi.org/10.1126/science.aae0061, 2016.

Stocker, T. F., Qin, D., Plattner, G. K., Tignor, M. M. B., Allen, S. K., Boschung, J., Nauels, A., Xia, Y., Bex, V., and Midgley, P. M.: Climate change 2013 the physical science basis: Working Group I contribution to the fifth assessment report of the intergovernmental panel on climate change vol 9781107057999, 2013.

von der Gathen, P., Kivi, R., Wohltmann, I., Salawitch, R. J., and Rex, M.: Climate change favours large seasonal loss of Arctic ozone, Nature Communications, 12, 3886, https://doi.org/10.1038/s41467-021-24089-6, 2021.

von Storch, H. and Zwiers, F. W.: Statistical analysis in climate research, Cambridge University Press, Cambridge, 1999, ISBN 0 521 45071 3, 484 pp.

Weatherhead, B., Tanskanen, A., Stevermer, A. (Lead Authors), Andersen, S. B., Arola, A., Austin, J., Bernhard, G., Browman, H., Fioletov, V., Grewe, V., Herman, J., Josefsson, W., Kylling, A., Kyrö, E., Lindfors, A., Shindell, D., Taalas, P., and Tarasick, D.: Ozone and ultraviolet radiation, In Arctic Climate Impact Assessment (ACIA), (Chapter 5, pp. 151–182), Cambridge University Press, 2005, Retrieved from https://acia.amap.no/ (last access: 23 4 September 2021 2022).

Weber, M., Coldewey-Weber, M., Coldewey-Egbers, M., Fioletov, V. E., Frith, S. M., Wild, J. D., Burrows, J. P., Long, C. S., Loyola, D.: Total ozone trends from 1979 to 2016 derived from five merged observational datasets – the emergence into ozone recovery, Atmos. Chem. Phys., 18, 2097–2117, https://doi.org/10.5194/acp-18-2097-2018, 2018.

Weihs, P., Simic, S., Laube, W., Mikielewicz, W., Rengarajan, G., and Mandl, M.: Albedo Influences on Surface UV Irradiance at the Sonnblick High-Mountain Observatory (3106-m Altitude), J. Applied

1206 Meteorology, 38, 1599–1610, https://doi.org/10.1175/1520-0450(1999)038<1599:AIOSUI>2.0.CO;2,
1207 1999.

1208 Wild, M., Gilgen, H., Roesch, A., Ohmura, A., Long, C. N., Dutton, E. G., Forgan, B., Kallis, A., Russak,
1209 V., and Tsvetkov, A.: From dimming to brightening: decadal changes in solar radiation at Earth's surface,
1210 Science, Vol. 308, Issue 5723, 847–850, doi: 10.1126/science.1103215, 2005.

1211 Zerefos, C., Kapsomenakis, J., Eleftheratos, K., Tourpali, K., Petropavlovskikh, I., Hubert, D., Godin-
1212 Beekmann, S., Steinbrecht, W., Frith, S., Sofieva, V., et al.: Representativeness of single lidar stations for
1213 zonally averaged ozone profiles, their trends and attribution to proxies, Atmos. Chem. Phys., 18, 6427–
1214 6440, 2018.

1215 Zerefos, C., Meleti, C., Balis, D., Tourpali, K., Bais, A. F.: Quasi-biennial and longer-term changes in clear
1216 sky UV-B solar irradiance, Geophys. Res. Lett., Vol. 25, No. 23, 4345-4348, 1998.

1217 Zerefos, C. S., Tourpali, K., Zanis, P., Eleftheratos, K., Repapis, C., Goodman, A., Wuebbles, D., Isaksen,
1218 I. S. A., and Luterbacher, J.: Evidence for an earlier greenhouse cooling effect in the stratosphere before
1219 1980 over the Northern Hemisphere, Atmospheric Chemistry and Physics, 14, 7705–7720, doi:
1220 10.5194/acp-14-7705-2014, 2014.

1221 Zhang, R., Wang, H., Fu, Q., Rasch, P. J., and Wang, X.: Unraveling driving forces explaining significant
1222 reduction in satellite-inferred Arctic surface albedo since the 1980s, Proc. Natl. Acad. Sci. USA, 116(48),
1223 23947–23953, doi:10.1073/pnas.1915258116, 2019.

1224

1225

1226 **Table 1.** Ground-based stations with long-term UV measurements used for the evaluation of EMAC CCM

1227 DNA active irradiance simulations. Stations are listed from northern to southern high latitudes and are

1228 grouped as follows: ~~2~~3 stations at latitudes greater than 55° N, 13 stations between 50° N – 50° S and 4

1229 stations at latitudes greater than 55° S.

Station name	Latitude	Longitude	Period
1. Summit, Greenland*	72.58	-38.45	08/2004-08/2017
2. Barrow, AK, United States*	71.32	-156.68	02/1991-07/2016
3. Sodankylä, Finland	67.37	26.63	01/1990-12/2021
~~3~~4. Villeneuve d'Ascq, France*	50.61	3.14	01/2000-12/2019
~~4~~5. Groß-Enzersdorf, Austria*	48.20	16.56	05/1998-11/2019
~~5~~6. Zugspitze, Germany*	47.42	10.98	08/1995-06/2007
~~6~~7. Hoher Sonnblick, Austria*	47.05	12.95	01/1997-06/2020
~~7~~8. Aosta, Italy	45.74	7.36	08/2006-09/2020
~~8~~9. Observatoire de Haute Provence, France*	43.94	5.70	01/2009-11/2018
~~9~~10. Thessaloniki, Greece	40.63	22.95	08/1993-12/2019
~~10~~11. Boulder, CO, United States*	39.99	-105.26	01/2004-12/2019
~~11~~12. Athens, Greece	37.99	23.78	07/2004-12/2020
~~12~~13. Mauna Loa, HI, United States*	19.53	-155.58	07/1995-12/2019
~~13~~14. Reunion Island, St. Denis, France*	-20.90	55.50	03/2009-12/2019
~~14~~15. Alice Springs, Australia*	-23.80	133.87	01/2005-12/2019
~~15~~16. Lauder, New Zealand*	-45.04	169.68	01/1991-12/2019
~~16~~17. Ushuaia, Argentina*	-54.82	-68.32	01/1990-11/2008
~~17~~18. Palmer, Antarctica*	-64.77	-64.05	03/1990-05/2021
~~18~~19. Arrival Heights, Antarctica*	-77.83	166.67	01/1990-04/2021
~~19~~20. South Pole, Antarctica*	-90	0	11/1990-03/2021

1230 *NDACC sites

1231

Table 2. (a) Correlation results between model simulations (~~SC1SD base 02~~HIS-SD) and ground-based DNA active irradiance data for the northern high latitude stations (>55° N), the southern high latitude stations (>55° S), and the stations between 50° N – 50° S. **(b)** Same as (a) but for the ~~SC1SD base 02~~HIS-SD simulation and satellite SBUV (v8.~~6~~7) total ozone data. **(c)** Same as (a) but for the ~~SC1SD base 02~~HIS-SD simulation and satellite MODIS/Terra cloud fraction data. Error, t-value, and p-value refer to slope; t-value should be higher than 2.576 for 99% statistical significance.

(a) DNA active irradiance

	R	Slope	Error	t-value	p-value	N	RMSE
>55° N	+0.518	0.657	0.129	5.105	<0.0001	73	9.543
>55° S	+0.746	0.879	0.070	12.629	<0.0001	129	14.766
50° N – 50° S	+0.499	0.387	0.045	8.564	<0.0001	223	4.215

(b) Total ozone

	R	Slope	Error	t-value	p-value	N	RMSE
>55° N	+0.908	0.839	0.034	24.627	<0.0001	131	1.359
>55° S	+0.892	0.888	0.040	22.211	<0.0001	129	3.414
50° N – 50° S	+0.894	0.817	0.028	29.672	<0.0001	223	0.872

(c) Cloud cover

	R	Slope	Error	t-value	p-value	N	RMSE
>55° N	+0.480	0.405	0.065	6.215	<0.0001	131	6.367
>55° S	+0.485	0.806	0.129	6.230	<0.0001	128	5.003
50° N – 50° S	+0.703	0.721	0.049	14.674	<0.0001	222	5.162

1239

(a) DNA active irradiance

	R	Slope	Error	t-value	p-value	N	RMSE
>55° N	+0.504	0.807	0.125	6.447	<0.0001	124	11.527
>55° S	+0.746	0.879	0.070	12.629	<0.0001	129	14.766
50° N – 50° S	+0.499	0.387	0.045	8.564	<0.0001	223	4.215

(b) Total ozone

	R	Slope	Error	t-value	p-value	N	RMSE
>55° N	+0.899	0.858	0.037	23.264	<0.0001	131	1.308
>55° S	+0.892	0.888	0.040	22.211	<0.0001	129	3.414
50° N – 50° S	+0.894	0.817	0.028	29.672	<0.0001	223	0.872

(c) Cloud cover

	R	Slope	Error	t-value	p-value	N	RMSE
>55° N	+0.453	0.362	0.063	5.775	<0.0001	131	4.483
>55° S	+0.485	0.806	0.129	6.230	<0.0001	128	5.003
50° N – 50° S	+0.703	0.721	0.049	14.674	<0.0001	222	5.162

1240

1241

1242

1243 **Table 3.** Trends (% per decade) in total ozone, DNA active irradiance, and cloudiness from the two model
1244 simulations and the differences between them, i.e., free-running simulation with increasing GHGs (~~RC2 base 04~~REF) minus the simulation with fixed GHGs at 1960 levels (~~SC2 fGHG 01~~FIX), averaged at ~~2~~3
1246 stations in the northern high latitudes (>55° N), 4 stations in the southern high latitudes (>55° S), and 13
1247 stations between 50° N – 50° S. The trends are estimated from the annual mean anomalies shown in Figures
1248 ~~3, 4, 5~~4, 5, 6.

1249

Trends (% per decade)	>55° N (2 stations)								
	RC2-base-04			SC2-fGHG-01			Difference		
	1960-1999	2000-2049	2050-2099	1960-1999	2000-2049	2050-2099	1960-1999	2000-2049	2050-2099
Ozone	−0.56 ± 0.24	0.53 ± 0.16	0.49 ± 0.17	−1.28 ± 0.27	0.42 ± 0.14	0.02 ± 0.16	0.72 ± 0.27	0.12 ± 0.16	0.47 ± 0.18
DNA active irradiance	0.29 ± 0.88	−2.79 ± 0.62	−2.54 ± 0.68	2.99 ± 0.91	−1.18 ± 0.49	−0.34 ± 0.57	−2.70 ± 1.16	−1.54 ± 0.63	−2.11 ± 0.74
Clouds	0.09 ± 0.40	−0.13 ± 0.30	0.18 ± 0.28	−0.05 ± 0.44	0.23 ± 0.19	−0.06 ± 0.29	0.14 ± 0.63	−0.36 ± 0.36	0.25 ± 0.39
Trends (% per decade)	>55° S (4 stations)								
	RC2-base-04			SC2-fGHG-01			Difference		
	1960-1999	2000-2049	2050-2099	1960-1999	2000-2049	2050-2099	1960-1999	2000-2049	2050-2099
Ozone	−3.78 ± 0.57	2.63 ± 0.31	1.42 ± 0.29	−4.65 ± 0.48	2.28 ± 0.41	0.58 ± 0.31	0.87 ± 0.56	0.35 ± 0.46	0.84 ± 0.42
DNA active irradiance	5.70 ± 0.97	−4.92 ± 0.55	−1.68 ± 0.43	7.61 ± 0.92	−4.81 ± 0.75	−0.72 ± 0.38	−1.91 ± 0.95	−0.10 ± 0.82	−0.97 ± 0.58
Clouds	−0.36 ± 0.39	−0.71 ± 0.28	−0.28 ± 0.26	0.18 ± 0.31	−0.05 ± 0.22	−0.01 ± 0.26	−0.54 ± 0.47	−0.53 ± 0.35	−0.21 ± 0.35
Trends (% per decade)	50° N − 50° S (13 stations)								
	RC2-base-04			SC2-fGHG-01			Difference		
	1960-1999	2000-2049	2050-2099	1960-1999	2000-2049	2050-2099	1960-1999	2000-2049	2050-2099
Ozone	−0.61 ± 0.14	0.42 ± 0.11	0.02 ± 0.12	−1.27 ± 0.16	0.36 ± 0.10	0.12 ± 0.09	0.66 ± 0.10	0.06 ± 0.08	−0.10 ± 0.09
DNA active irradiance	1.55 ± 0.44	−0.53 ± 0.35	0.86 ± 0.35	1.75 ± 0.48	−0.54 ± 0.32	0.05 ± 0.28	−0.20 ± 0.58	0.01 ± 0.44	0.81 ± 0.39
Clouds	−1.15 ± 0.29	−0.30 ± 0.27	−0.60 ± 0.25	0.16 ± 0.30	−0.25 ± 0.23	−0.16 ± 0.19	−1.21 ± 0.42	−0.12 ± 0.30	−0.50 ± 0.27

1250

Trends (% per decade)	>55° N (3 stations)								
	REF			FIX			Difference		
	1960-1999	2000-2049	2050-2099	1960-1999	2000-2049	2050-2099	1960-1999	2000-2049	2050-2099
Ozone	−0.55 ± 0.21	0.50 ± 0.16	0.41 ± 0.17	−1.35 ± 0.26	0.36 ± 0.15	0.05 ± 0.15	0.79 ± 0.24	0.14 ± 0.16	0.36 ± 0.17
DNA active irradiance	1.03 ± 0.77	−1.75 ± 0.56	−2.47 ± 0.60	2.61 ± 0.78	−1.15 ± 0.46	−0.83 ± 0.57	−1.57 ± 0.96	−0.59 ± 0.68	−1.64 ± 0.76
Clouds	−0.21 ± 0.30	−0.10 ± 0.23	0.32 ± 0.20	−0.20 ± 0.43	0.02 ± 0.25	0.19 ± 0.27	−0.29 ± 0.45	−0.39 ± 0.25	0.29 ± 0.27

Trends (% per decade)	REF			FIX			Difference		
	>55º S (4 stations)								
	1960-1999	**2000-2049**	**2050-2099**	**1960-1999**	**2000-2049**	**2050-2099**	**1960-1999**	**2000-2049**	**2050-2099**
Ozone	−3.78 ± 0.57	2.63 ± 0.31	1.42 ± 0.29	−4.65 ± 0.48	2.28 ± 0.41	0.58 ± 0.31	0.87 ± 0.56	0.35 ± 0.46	0.84 ± 0.42
DNA active irradiance	5.70 ± 0.97	−4.92 ± 0.55	−1.68 ± 0.43	7.61 ± 0.92	−4.81 ± 0.75	−0.72 ± 0.38	−1.91 ± 0.95	−0.10 ± 0.82	−0.97 ± 0.58
Clouds	−0.36 ± 0.39	−0.71 ± 0.28	−0.28 ± 0.26	0.18 ± 0.31	−0.05 ± 0.22	−0.01 ± 0.26	−0.54 ± 0.47	−0.53 ± 0.35	−0.21 ± 0.35

Trends (% per decade)	REF			FIX			Difference		
	50º N – 50º S (13 stations)								
	1960-1999	**2000-2049**	**2050-2099**	**1960-1999**	**2000-2049**	**2050-2099**	**1960-1999**	**2000-2049**	**2050-2099**
Ozone	−0.61 ± 0.14	0.42 ± 0.11	0.02 ± 0.12	−1.27 ± 0.16	0.36 ± 0.10	0.12 ± 0.09	0.66 ± 0.10	0.06 ± 0.08	−0.10 ± 0.09
DNA active irradiance	1.55 ± 0.44	−0.53 ± 0.35	0.86 ± 0.35	1.75 ± 0.48	−0.54 ± 0.32	0.05 ± 0.28	−0.20 ± 0.58	0.01 ± 0.44	0.81 ± 0.39
Clouds	−1.15 ± 0.29	−0.30 ± 0.27	−0.60 ± 0.25	0.16 ± 0.30	−0.25 ± 0.23	−0.16 ± 0.19	−1.21 ± 0.42	−0.12 ± 0.30	−0.50 ± 0.27

1251

1252

1253

1254

1255 **Table 4.** Same as Table 3 but for the winter months, January (J), February (F), and March (M) for the

1256 northern high latitude stations. Due to the polar night, UV results for January and February are not shown

1257 due to large standard errors.

		>55° N (2 stations)								
Trends (% per decade)		RC2-base-04			SC2-fGHG-01			Difference		
		1960-1999	2000-2049	2050-2099	1960-1999	2000-2049	2050-2099	1960-1999	2000-2049	2050-2099
Ozone (J)		−1.85 ± 0.91	1.72 ± 0.59	−0.02 ± 0.63	−1.09 ± 0.93	0.33 ± 0.58	0.61 ± 0.64	−0.76 ± 1.36	1.39 ± 0.71	−0.63 ± 0.88
Ozone (F)		−2.36 ± 0.78	2.09 ± 0.63	1.39 ± 0.62	−2.15 ± 0.84	0.21 ± 0.61	0.17 ± 0.48	−0.21 ± 1.08	1.88 ± 0.81	1.22 ± 0.76
Ozone (M)		−3.16 ± 0.53	0.65 ± 0.49	0.83 ± 0.39	−2.79 ± 0.71	0.84 ± 0.38	−0.82 ± 0.48	−0.37 ± 0.81	−0.18 ± 0.55	1.65 ± 0.59
DNA active irradiance (J)		Polar night	Polar night	Polar night	Polar night	Polar night	Polar night	Polar night	Polar night	Polar night
DNA active irradiance (F)		Polar night	Polar night	Polar night	Polar night	Polar night	Polar night	Polar night	Polar night	Polar night
DNA active irradiance (M)		5.49 ± 1.77	−1.70 ± 1.40	−3.00 ± 1.22	8.28 ± 1.90	−0.82 ± 1.23	1.30 ± 1.19	−2.80 ± 2.41	−0.49 ± 1.81	−4.29 ± 1.64
Clouds (J)		−0.67 ± 0.67	1.38 ± 0.62	0.41 ± 0.54	1.21 ± 0.66	−0.31 ± 0.52	0.43 ± 0.51	−1.84 ± 0.93	1.70 ± 0.98	0.11 ± 0.74
Clouds (F)		−0.71 ± 0.99	0.99 ± 0.72	0.83 ± 0.68	0.47 ± 0.91	−0.54 ± 0.71	−0.26 ± 0.65	−1.58 ± 1.11	−0.60 ± 1.12	0.09 ± 0.88
Clouds (M)		0.47 ± 0.88	1.34 ± 0.92	1.61 ± 0.73	0.72 ± 1.35	0.31 ± 0.94	−0.27 ± 0.78	−0.25 ± 1.44	1.03 ± 1.30	1.92 ± 0.95

1258

		>55° N (3 stations)								
Trends (% per decade)		REF			FIX			Difference		
		1960-1999	2000-2049	2050-2099	1960-1999	2000-2049	2050-2099	1960-1999	2000-2049	2050-2099
Ozone (J)		−1.66 ± 0.74	1.81 ± 0.53	0.49 ± 0.53	−1.32 ± 0.72	0.28 ± 0.50	0.28 ± 0.54	−0.34 ± 1.09	1.53 ± 0.64	0.21 ± 0.73
Ozone (F)		−2.27 ± 0.74	2.00 ± 0.59	0.88 ± 0.58	−1.65 ± 0.83	0.21 ± 0.54	0.31 ± 0.44	−0.62 ± 0.96	1.79 ± 0.78	0.58 ± 0.71
Ozone (M)		−2.98 ± 0.53	0.75 ± 0.50	0.66 ± 0.35	−3.04 ± 0.71	0.58 ± 0.39	−0.54 ± 0.41	0.06 ± 0.83	0.17 ± 0.58	1.20 ± 0.51
DNA active irradiance (J)		Polar night	Polar night	Polar night	Polar night	Polar night	Polar night	Polar night	Polar night	Polar night
DNA active irradiance (F)		Polar night	Polar night	Polar night	Polar night	Polar night	Polar night	Polar night	Polar night	Polar night
DNA active irradiance (M)		3.03 ± 1.97	−0.63 ± 1.52	−2.83 ± 1.22	7.20 ± 1.77	−0.09 ± 1.44	−0.98 ± 1.27	−3.28 ± 2.55	−0.06 ± 2.18	−1.90 ± 1.51
Clouds (J)		−0.67 ± 0.61	1.29 ± 0.63	0.94 ± 0.48	1.11 ± 0.77	0.03 ± 0.53	0.52 ± 0.49	−1.77 ± 0.92	1.25 ± 0.88	0.39 ± 0.68
Clouds (F)		−0.07 ± 0.86	0.60 ± 0.68	1.30 ± 0.57	0.55 ± 0.81	−0.14 ± 0.66	0.06 ± 0.58	−0.62 ± 1.11	0.74 ± 0.93	1.24 ± 0.82
Clouds (M)		0.35 ± 0.70	1.15 ± 0.60	1.33 ± 0.61	0.23 ± 1.02	0.21 ± 0.69	−0.17 ± 0.64	0.12 ± 1.12	0.94 ± 0.88	1.49 ± 0.79

1259

1260

1261

1262 **Table 5.** Statistical test results for the difference between two trends in DNA active irradiance (trend of
1263 1960-2049 minus trend of 2050-2099), for the northern high latitude stations (>55⁰ N), the southern high
1264 latitude stations (>55⁰ S), and the stations between 50⁰ N – 50⁰ S.

Latitudes	>55⁰ N (2 stations)		>55⁰ S (4 stations)		50⁰ N – 50⁰ S (13 stations)	
	1960–2049	2050–2099	1960–2049	2050–2099	1960–2049	2050–2099
N	605	336	630	350	1080	600
slope, b/year (Eq. 4)	–0.200	–0.204	–0.116	–0.096	–0.033	0.081
S_b (Eqs. 5 and 6)	0.027	0.061	0.026	0.048	0.015	0.037
S_{b1-b2} (Eq. 3)	0.067		0.054		0.040	
t (Eq. 3)	0.061		–0.376		–2.844	
degrees of freedom	937		976		1676	
significance level	0.05		0.05		0.05	
p-value	0.951		0.707		0.005	
t-critical	1.96		1.96		1.96	
Significantly different trends	No		No		Yes	

1265

Latitudes	>55⁰ N (3 stations)		>55⁰ S (4 stations)		50⁰ N – 50⁰ S (13 stations)	
	1960–2049	2050–2099	1960–2049	2050–2099	1960–2049	2050–2099
N	553	315	630	350	1080	600
slope, $b/year$ (Eq. 4)	–0.173	–0.186	–0.116	–0.096	–0.033	0.081
s_b (Eqs. 5 and 6)	0.027	0.062	0.026	0.048	0.015	0.037
$s_{(b_1-b_2)}$ (Eq. 3)	0.068		0.054		0.040	
$t-value$ (Eq. 3)	0.185		–0.376		–2.844	
degrees of freedom	864		976		1676	
significance level	0.05		0.05		0.05	
$p-value$	0.853		0.707		0.005	
$t-critical$	1.96		1.96		1.96	
Significantly different trends	No		No		Yes	

1266

1267

1268

1269 **Table 6. (a)** Coefficients of multiple regression analysis according to Eq. (7), applied to the differences
1270 between the two model simulations, ~~RC2 base 04~~REF and ~~SC2 fGHG 01~~FIX, for the period 2050–2099,
1271 for the northern high latitude stations (>55º N), the southern high latitude stations (>55º S), and the stations
1272 between 50º N – 50º S. **(b)** Trends (% per decade) for the period 2050-2099 in the DNA active irradiance,
1273 the ozone-related DNA active irradiance component and the cloud-related DNA active irradiance
1274 component.

(a) MLR coefficients (2050–2099)	>55º N (2 stations)	>55º S (4 stations)	50º N – 50º S (13 stations)
$a \pm error$	−4.305 ± 0.885	−1.994 ± 0.670	−0.557 ± 0.336
$\beta_{O_3} \pm error$	−2.068 ± 0.187	−0.667 ± 0.071	−2.831 ± 0.128
$\beta_{cloud} \pm error$	−0.593 ± 0.068	−0.367 ± 0.065	−0.642 ± 0.035

(b) Trends (% per decade) (2050–2099)	>55º N (2 stations)	>55º S (4 stations)	50º N – 50º S (13 stations)
DNA active irradiance	−2.04 ± 0.61%	−0.96 ± 0.48%	0.81 ± 0.37%
Ozone-related DNA active irradiance component	−0.96 ± 0.30%	−0.57 ± 0.21%	0.27 ± 0.20%
Cloud-related DNA active irradiance component	−0.14 ± 0.23%	0.07 ± 0.13%	0.33 ± 0.17%

1275

(a) MLR coefficients (2050–2099)	>55º N (3 stations)	>55º S (4 stations)	50º N – 50º S (13 stations)
$a \pm error$	−4.473 ± 0.976	−1.994 ± 0.670	−0.557 ± 0.336
$\beta_{O_3} \pm error$	−2.017 ± 0.220	−0.667 ± 0.071	−2.831 ± 0.128
$\beta_{cloud} \pm error$	−0.749 ± 0.090	−0.367 ± 0.065	−0.642 ± 0.035

(b) Trends (% per decade) (2050–2099)	>55º N (3 stations)	>55º S (4 stations)	50º N – 50º S (13 stations)
DNA active irradiance	−1.86 ± 0.61%	−0.96 ± 0.48%	0.81 ± 0.37%
Ozone-related DNA active irradiance component	−0.72 ± 0.25%	−0.57 ± 0.21%	0.27 ± 0.20%
Cloud-related DNA active irradiance component	−0.21 ± 0.24%	0.07 ± 0.13%	0.33 ± 0.17%

1276

1277

1278

1279   **Table 7.** Trends and their standard errors (% per decade) in the differences between the two model
1280   simulations, ~~RC2 base 04~~REF and ~~SC2 fGHG 01~~FIX, for the DNA active irradiance, total ozone, cloud
1281   cover and surface albedo at Barrow (Alaska) and Palmer (Antarctica) for the periods 1960–1999, 2000–
1282   2049 and 2050–2099.

Trends (% per decade)	Barrow, Alaska			Palmer, Antarctica		
	1960-1999	2000-2049	2050-2099	1960-1999	2000-2049	2050-2099
DNA active irradiance	−2.88 ± 1.67	−2.18 ± 1.17	−2.14 ± 1.12	0.75 ± 1.47	−1.79 ± 1.08	−0.33 ± 0.90
Ozone	0.39 ± 0.24	0.06 ± 0.17	0.44 ± 0.19	−0.02 ± 0.54	0.23 ± 0.37	0.54 ± 0.40
Clouds	−0.96 ± 0.78	0.42 ± 0.54	0.60 ± 0.52	−1.60 ± 0.65	0.41 ± 0.49	−0.46 ± 0.48
Surface albedo	0.88 ± 1.33	−6.42 ± 0.80	−2.73 ± 0.89	0.08 ± 0.82	−1.52 ± 0.51	−1.60 ± 0.53

1283

1284

1285
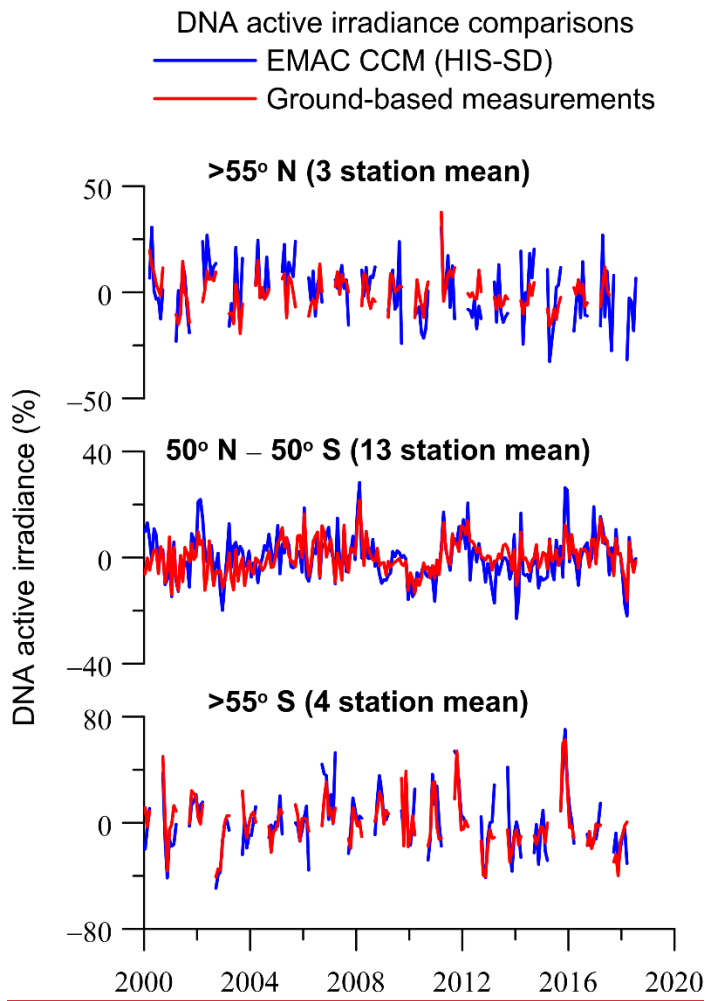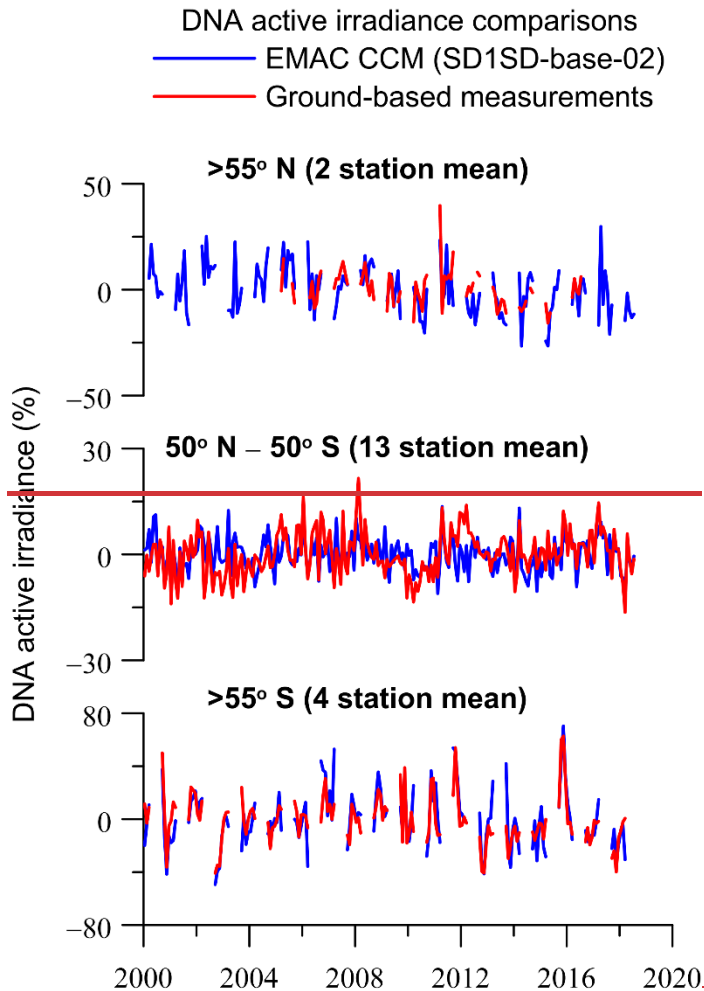
Figure 1. Comparison of model simulations of DNA active irradiance with averages of ground-based measurements at ~~2~~ 3 UV stations in the northern high latitudes (>55º N) (upper panel), 13 UV stations from 50º N to 50º S (middle panel) and 4 UV stations in the southern high latitudes (>55º S) (lower panel). ~~Shown are data from March to September for the northern high latitudes and from September to March for the southern high latitudes.~~ The y-axis shows ~~yearly averaged~~monthly de-seasonalized DNA active irradiance data (in %) ~~calculated from de-seasonalized monthly data~~. The monthly data at each station were de-seasonalized by subtracting the long-term monthly mean (2000–2018) pertaining to the same calendar month and were expressed in %. The~~n, the~~ average over each geographical zone was estimated by averaging the de-seasonalized data of the stations belonging to each geographical zone. Shown are data from March to September for the northern high latitudes and from September to March for the southern high latitudes.~~For the northern high latitude stations, the annual average refers to the average of monthly anomalies from March to September, and for the southern high latitude stations, it refers to the average of monthly anomalies from September to March. For the stations between 50° N–50° S we used all months to calculate the annual average.~~

1304

1305
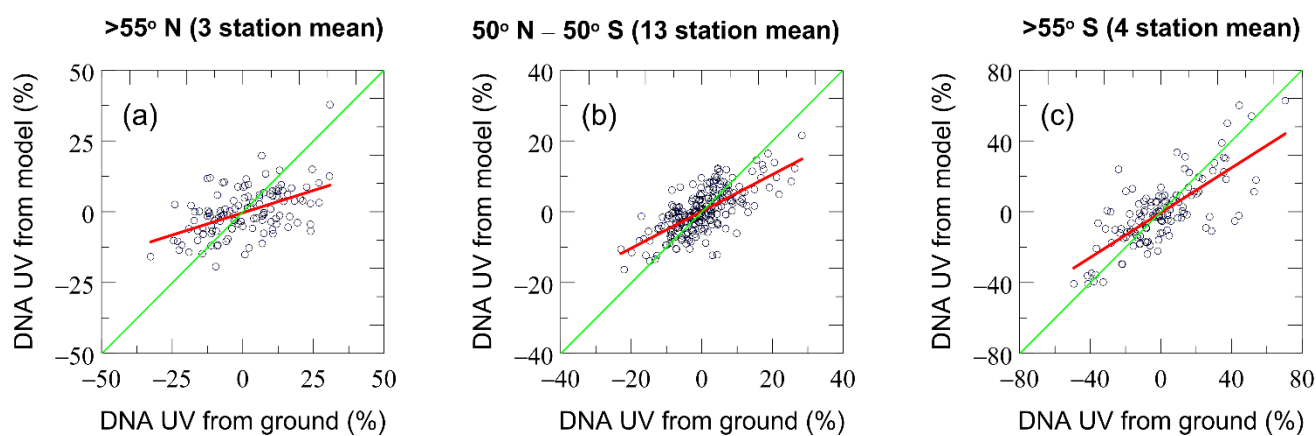
1306 **Figure 2.** Scatter plots of DNA active irradiance from simulated and ground-based data shown in Figure 1
1307 for **(a)** 3 UV stations in the northern high latitudes (>55° N), **(b)** 13 UV stations from 50° N to 50° S and **(c)**
1308 4 UV stations in the southern high latitudes (>55° S).

1309

1310

1313
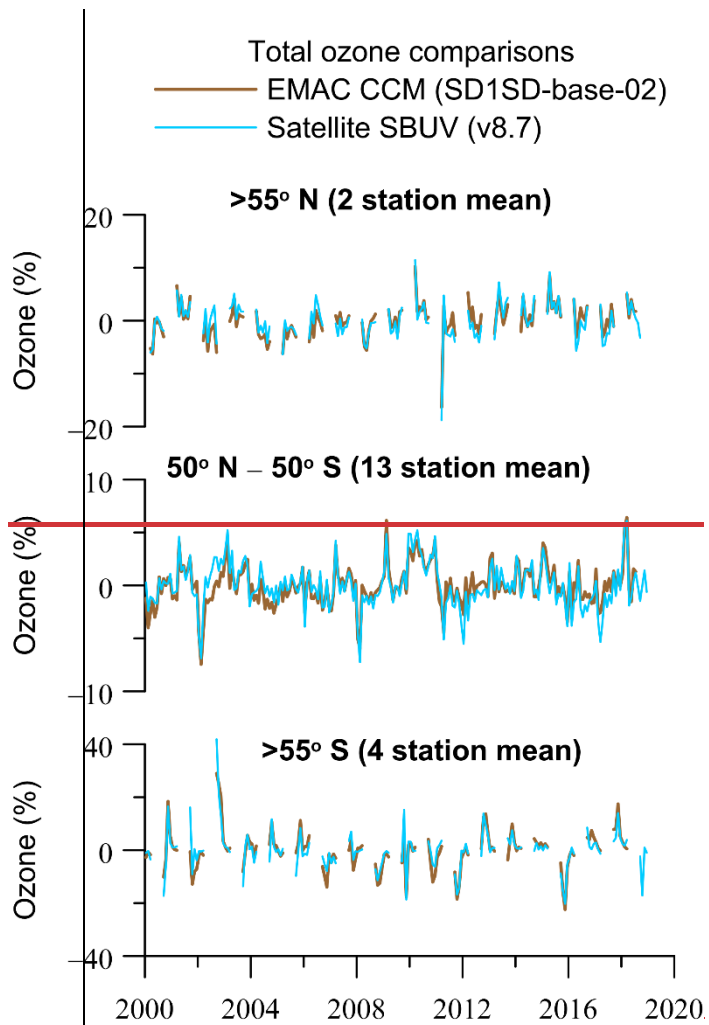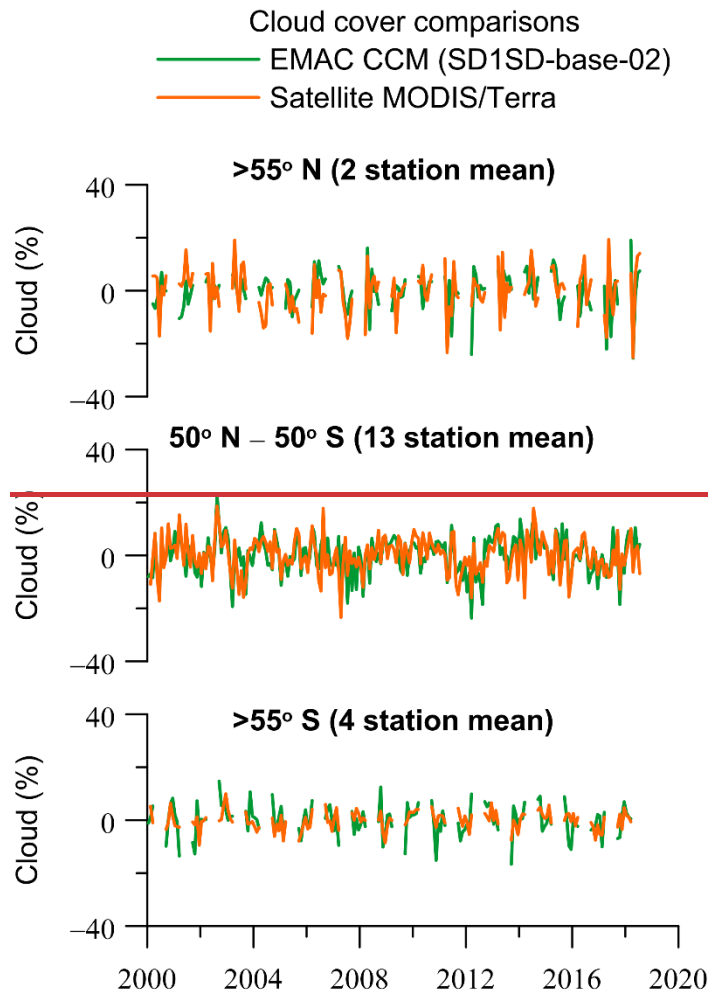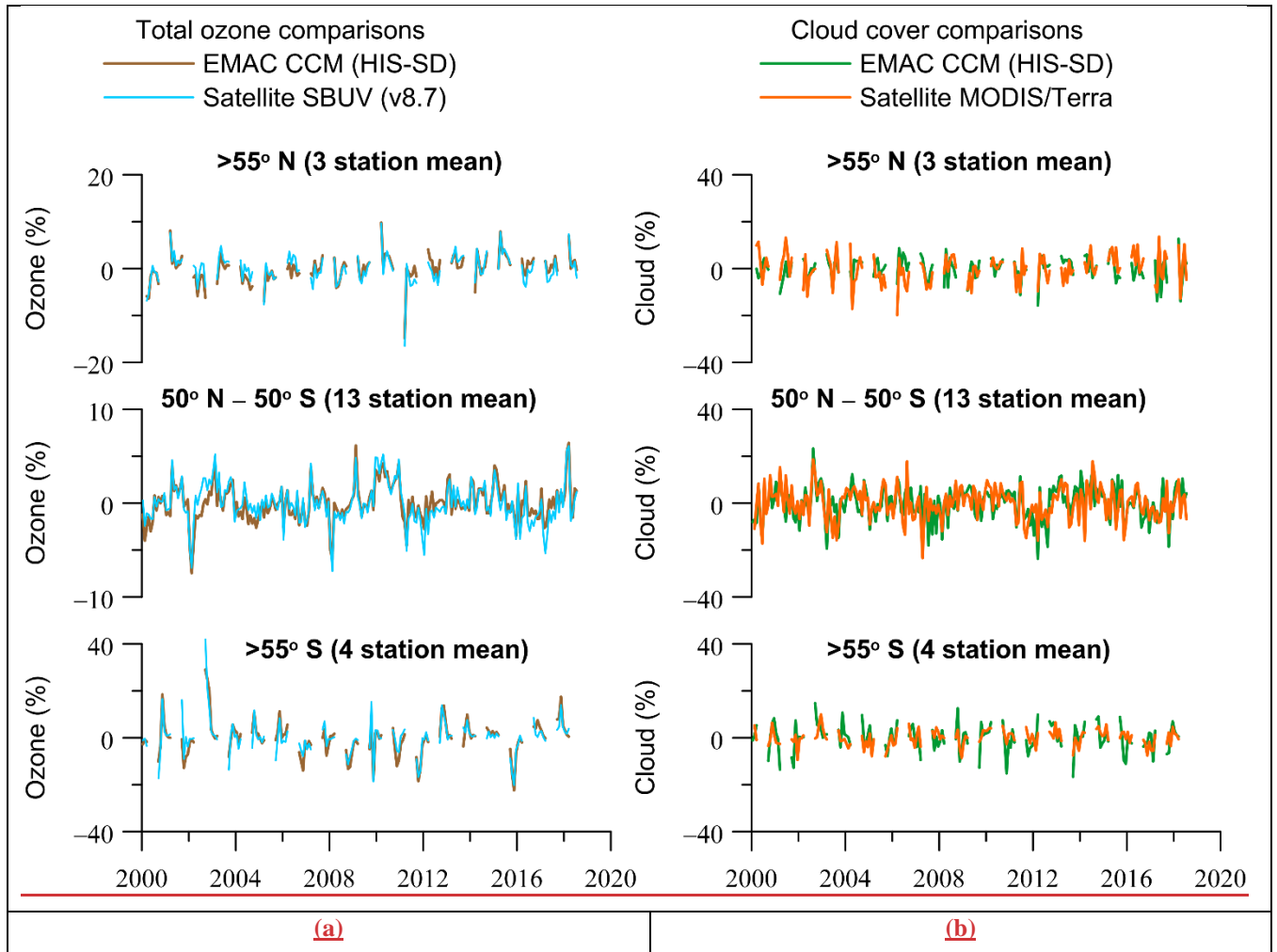
Figure 2̶3. **(a)** Same as in Figure 1 but for ozone column. **(b)** For cloud cover. The y-axes show monthly
de-seasonalized anomalies (in %) y̶e̶a̶r̶l̶y̶ ̶a̶v̶e̶r̶a̶g̶e̶d̶ ̶d̶a̶t̶a̶ ̶(̶i̶n̶ ̶%̶)̶ ̶c̶a̶l̶c̶u̶l̶a̶t̶e̶d̶ ̶f̶r̶o̶m̶ ̶d̶e̶-̶s̶e̶a̶s̶o̶n̶a̶l̶i̶z̶e̶d̶ ̶m̶o̶n̶t̶h̶l̶y̶
d̶a̶t̶a̶.̶ ̶T̶h̶e̶ ̶m̶o̶n̶t̶h̶l̶y̶ ̶d̶a̶t̶a̶ ̶w̶e̶r̶e̶ ̶d̶e̶-̶s̶e̶a̶s̶o̶n̶a̶l̶i̶z̶e̶d̶ relative to the long-term monthly mean (2000–2018) ̶a̶n̶d̶
w̶e̶r̶e̶ ̶e̶x̶p̶r̶e̶s̶s̶e̶d̶ ̶i̶n̶ ̶%̶.̶ Shown are monthly anomalies from March to September for the northern high
latitudes, and from September to March for the southern high latitudes. For 50º N–50º S, we present all
months.F̶o̶r̶ ̶t̶h̶e̶ ̶n̶o̶r̶t̶h̶e̶r̶n̶ ̶h̶i̶g̶h̶ ̶l̶a̶t̶i̶t̶u̶d̶e̶ ̶s̶t̶a̶t̶i̶o̶n̶s̶,̶ ̶t̶h̶e̶ ̶a̶n̶n̶u̶a̶l̶ ̶a̶v̶e̶r̶a̶g̶e̶ ̶r̶e̶f̶e̶r̶s̶ ̶t̶o̶ ̶t̶h̶e̶ ̶a̶v̶e̶r̶a̶g̶e̶ ̶o̶f̶ ̶m̶o̶n̶t̶h̶l̶y̶
a̶n̶o̶m̶a̶l̶i̶e̶s̶ ̶f̶r̶o̶m̶ ̶M̶a̶r̶c̶h̶ ̶t̶o̶ ̶S̶e̶p̶t̶e̶m̶b̶e̶r̶,̶ ̶a̶n̶d̶ ̶f̶o̶r̶ ̶t̶h̶e̶ ̶s̶o̶u̶t̶h̶e̶r̶n̶ ̶h̶i̶g̶h̶ ̶l̶a̶t̶i̶t̶u̶d̶e̶ ̶s̶t̶a̶t̶i̶o̶n̶s̶,̶ ̶i̶t̶ ̶r̶e̶f̶e̶r̶s̶ ̶t̶o̶ ̶t̶h̶e̶ ̶a̶v̶e̶r̶a̶g̶e̶ ̶o̶f̶
m̶o̶n̶t̶h̶l̶y̶ ̶a̶n̶o̶m̶a̶l̶i̶e̶s̶ ̶f̶r̶o̶m̶ ̶S̶e̶p̶t̶e̶m̶b̶e̶r̶ ̶t̶o̶ ̶M̶a̶r̶c̶h̶.̶ ̶F̶o̶r̶ ̶t̶h̶e̶ ̶s̶t̶a̶t̶i̶o̶n̶s̶ ̶b̶e̶t̶w̶e̶e̶n̶ ̶5̶0̶°̶ ̶N̶–̶5̶0̶°̶ ̶S̶ ̶w̶e̶ ̶u̶s̶e̶d̶ ̶a̶l̶l̶ ̶m̶o̶n̶t̶h̶s̶ ̶t̶o̶
c̶a̶l̶c̶u̶l̶a̶t̶e̶ ̶t̶h̶e̶ ̶a̶n̶n̶u̶a̶l̶ ̶a̶v̶e̶r̶a̶g̶e̶.̶

1323
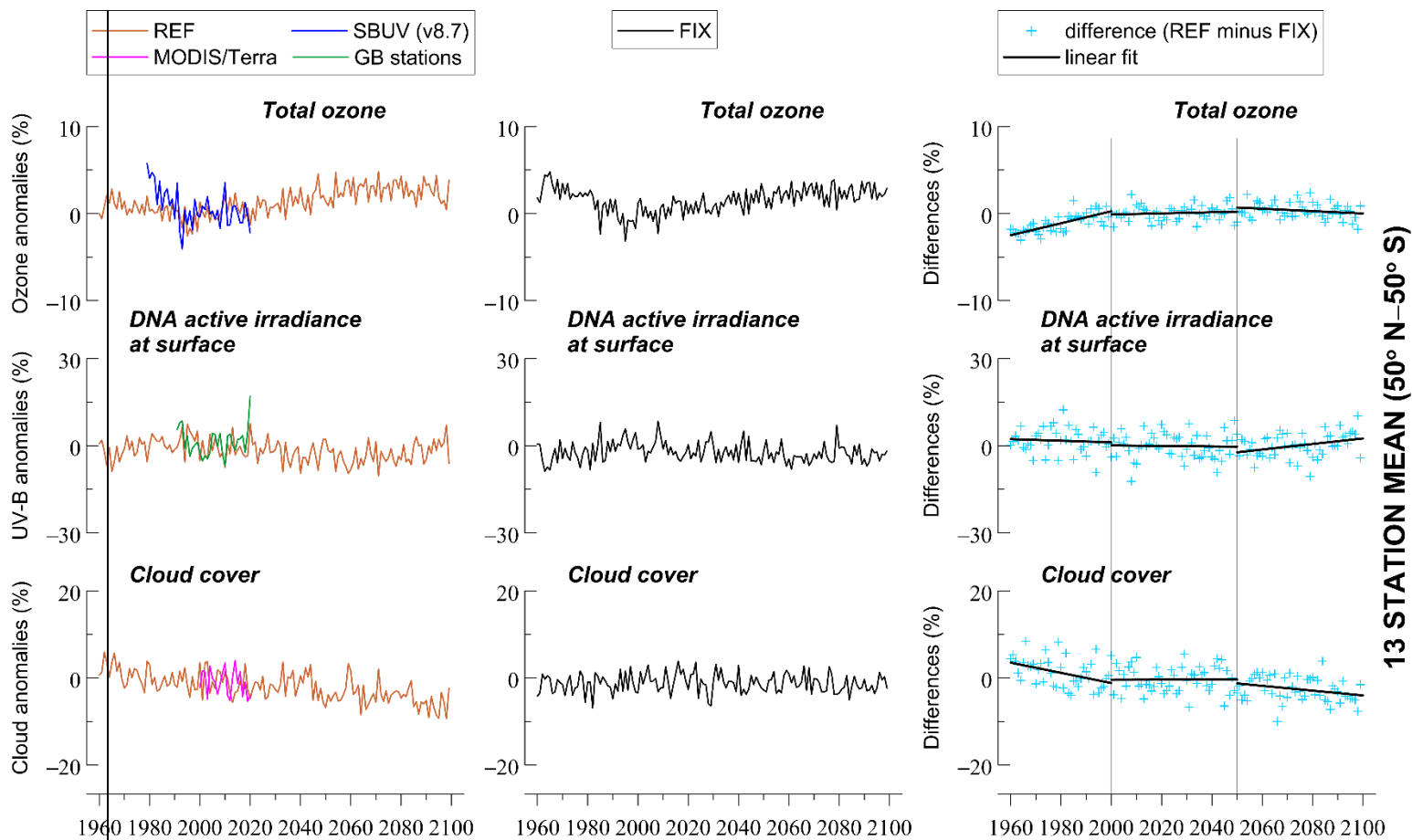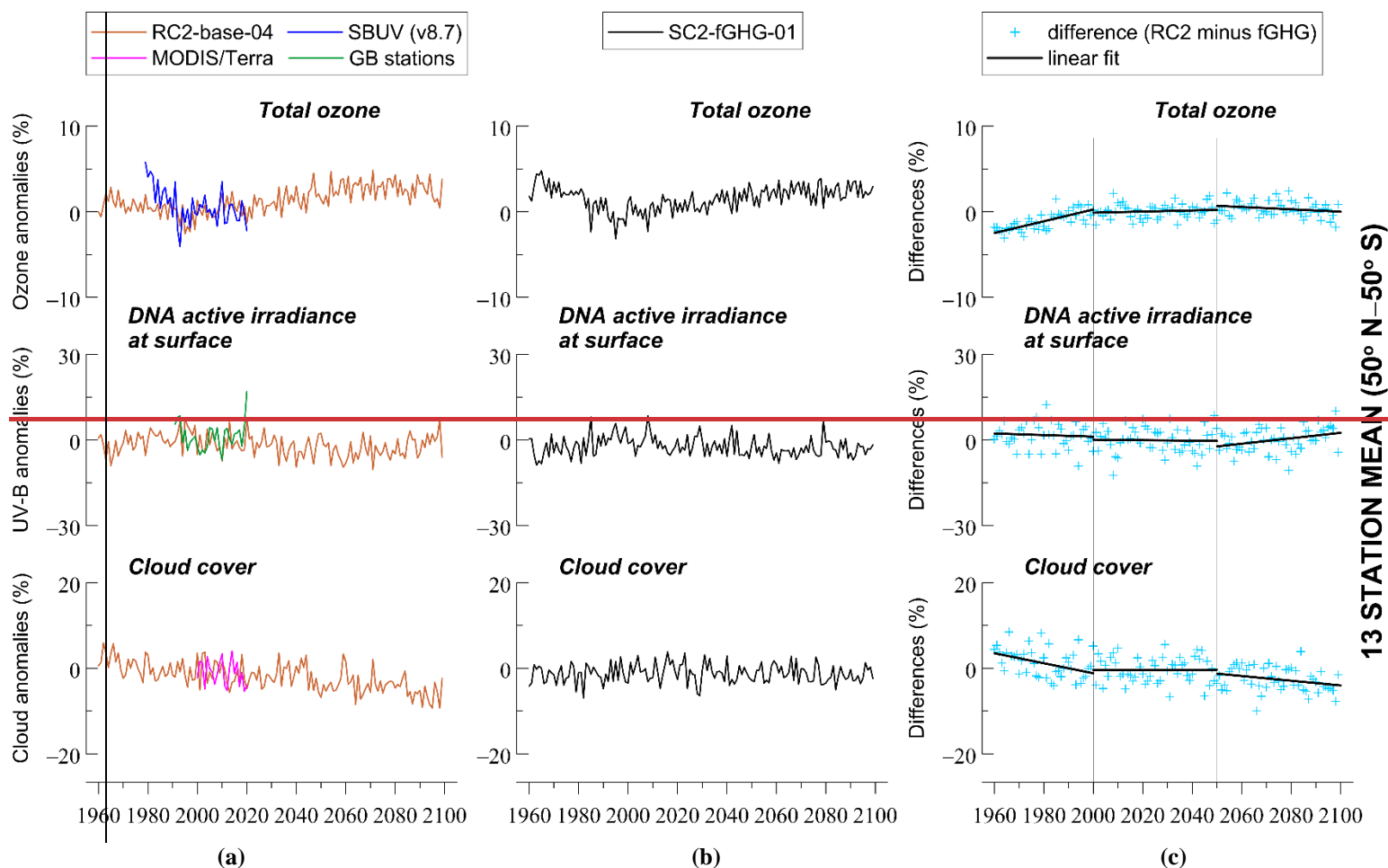
1324 **Figure 3̶4.** Changes in total ozone, DNA active irradiance and cloud cover averaged at 13 UV stations from
1325 50º N to 50º S, based on simulations with increasing and fixed GHGs mixing ratios. **(a)** R̶C̶2̶ ̶b̶a̶s̶e̶ ̶0̶4REF
1326 is the simulation with increasing GHGs according to RCP-6.0. **(b)** S̶C̶2̶ ̶f̶G̶H̶G̶ ̶0̶1FIX is the simulation with
1327 fixed GHGs emissions at 1960 levels. **(c)** Difference between the two model simulations, indicating the
1328 impact of increasing GHGs. The y-axes in (a) and (b) show yearly averaged data (in %) calculated from de-
1329 seasonalized monthly data. The monthly data were de-seasonalized relative to the long-term monthly mean
1330 (1990–2019) and were expressed in %. For stations between 50º N–50º S we used all months to calculate
1331 the   annual   average.
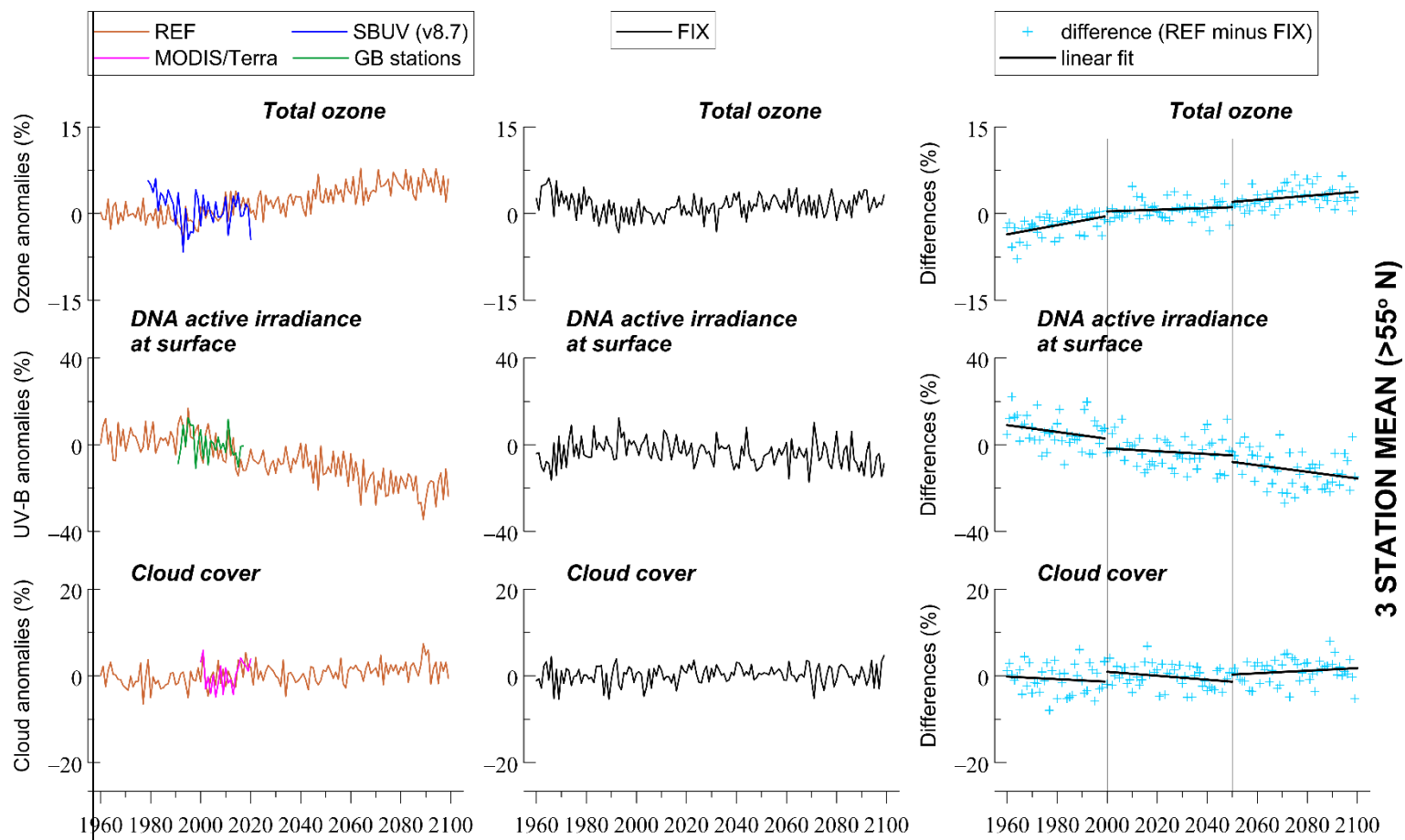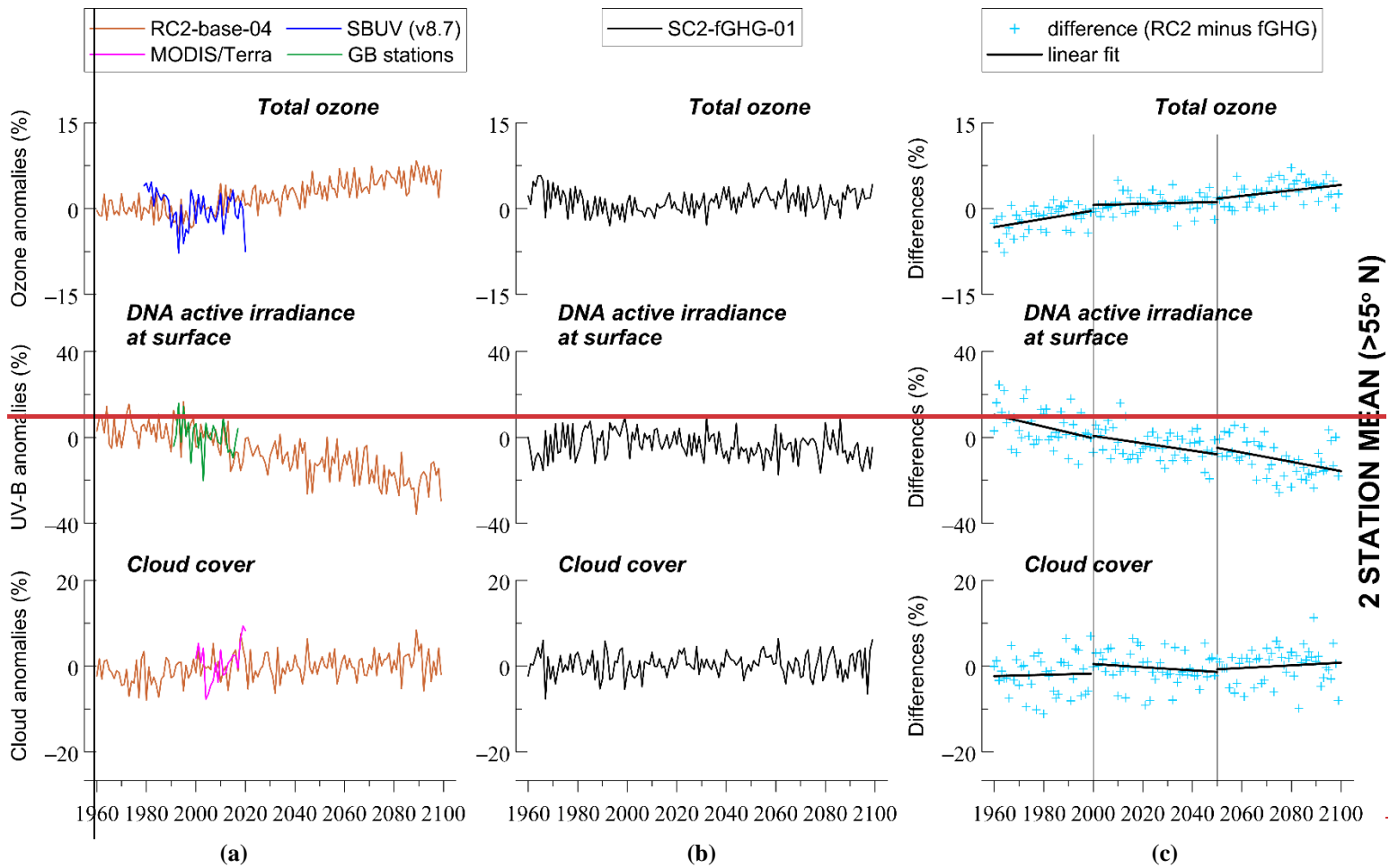
Figure 4~~5~~. ~~Changes in total ozone, DNA active irradiance and cloud cover averaged at 2~~ Same as Figure 4 but for 3 UV stations in the northern high latitudes (>55° N). The y-axes in (a) and (b) show averages of monthly de-seasonalized anomalies from March to September. ~~, based on simulations with increasing and fixed GHGs mixing ratios. (a) RC2 base 04 is the simulation with increasing GHGs according to RCP 6.0. (b) SC2 fGHG 01 is the simulation with fixed GHGs emissions at 1960 levels. (c) Difference between the two model simulations, indicating the impact of increasing GHGs. The y axes in (a) and (b) show yearly averaged data (in %) calculated from de seasonalized monthly data. The monthly data were de seasonalized relative to the long term monthly mean (1990 2019) and were expressed in %. For the northern high latitude stations, the annual average refers to the average of monthly anomalies from March to September.~~
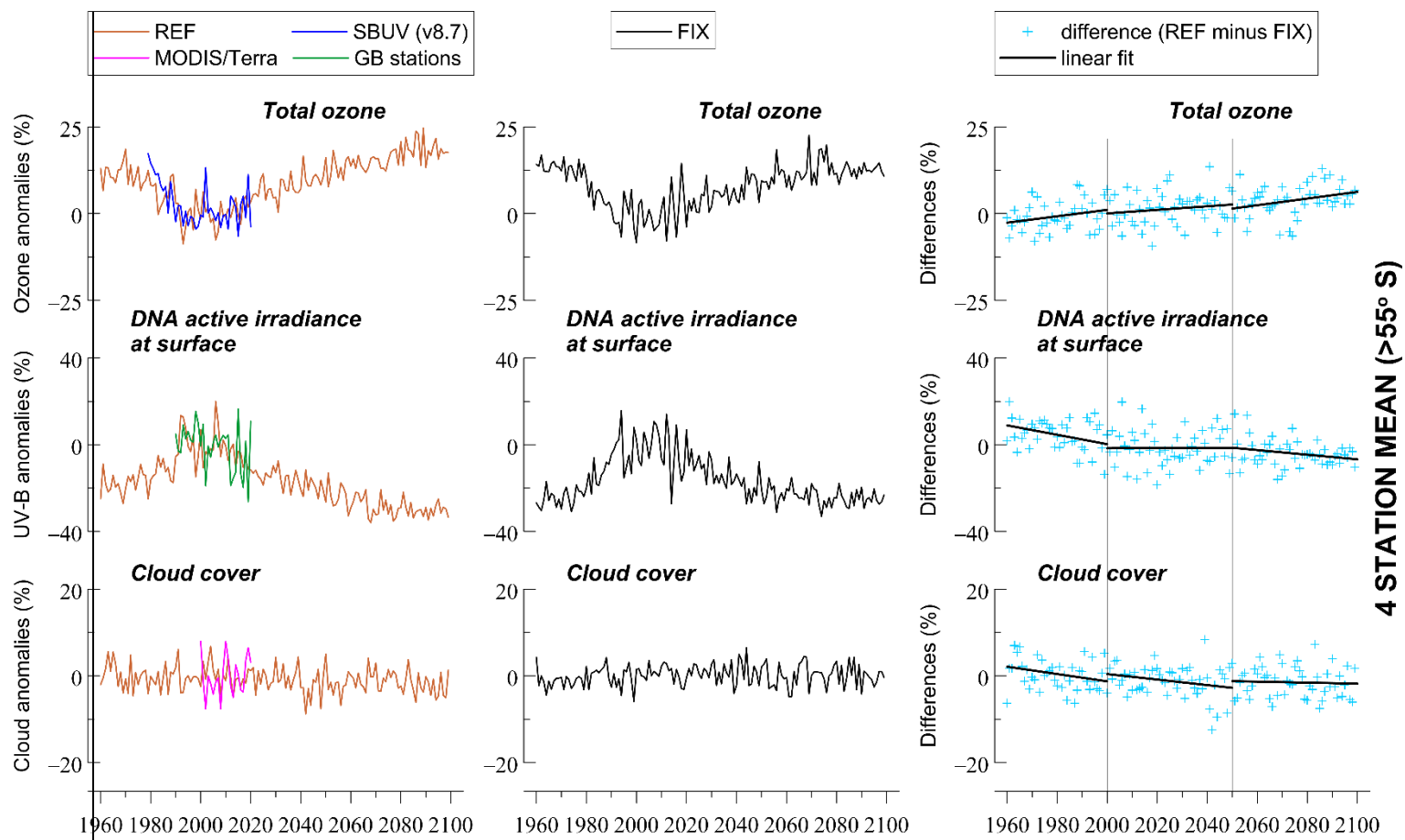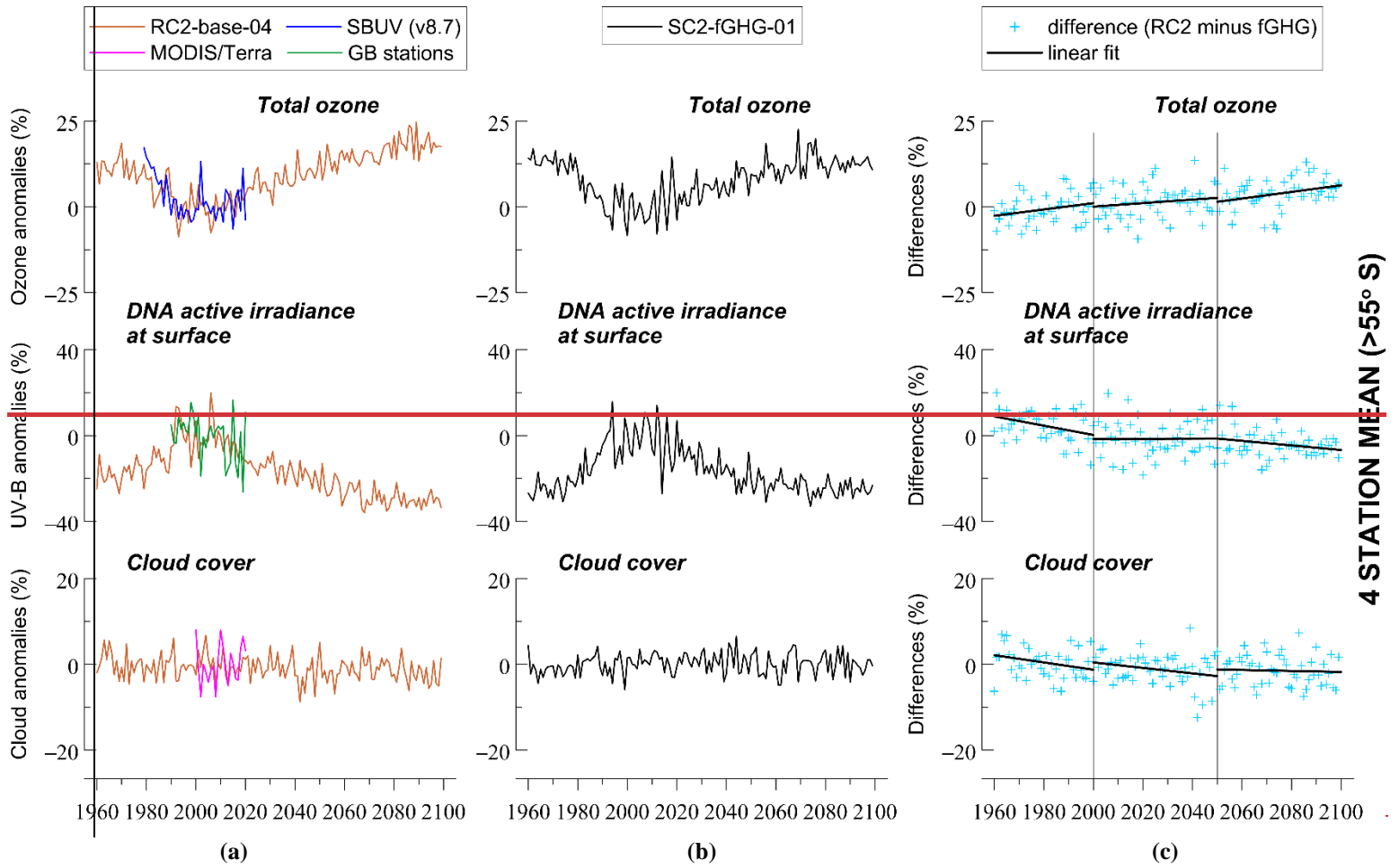
Figure ~~5~~6. ~~Changes in total ozone, DNA active irradiance and cloud cover averaged at~~ Same as Figure 4 but for 4 UV stations in the southern high latitudes (>55° S). The y-axes in (a) and (b) show averages of monthly de-seasonalized anomalies from September to March., ~~based on simulations with increasing and fixed GHGs mixing ratios. (a) RC2-base-04 is the simulation with increasing GHGs according to RCP 6.0. (b) SC2-fGHG-01 is the simulation with fixed GHGs emissions at 1960 levels. (c) Difference between the two model simulations, indicating the impact of increasing GHGs. The y-axes in (a) and (b) show yearly averaged data (in %) calculated from de-seasonalized monthly data. The monthly data were de-seasonalized relative to the long-term monthly mean (1990-2019) and were expressed in %. For the southern high latitude stations, the annual average refers to the average of monthly anomalies from September to March.~~

**EMAC CCM differences
(REF minus FIX)**

a) Surface albedo (BARROW)

b) Surface albedo (PALMER)

1352

1353
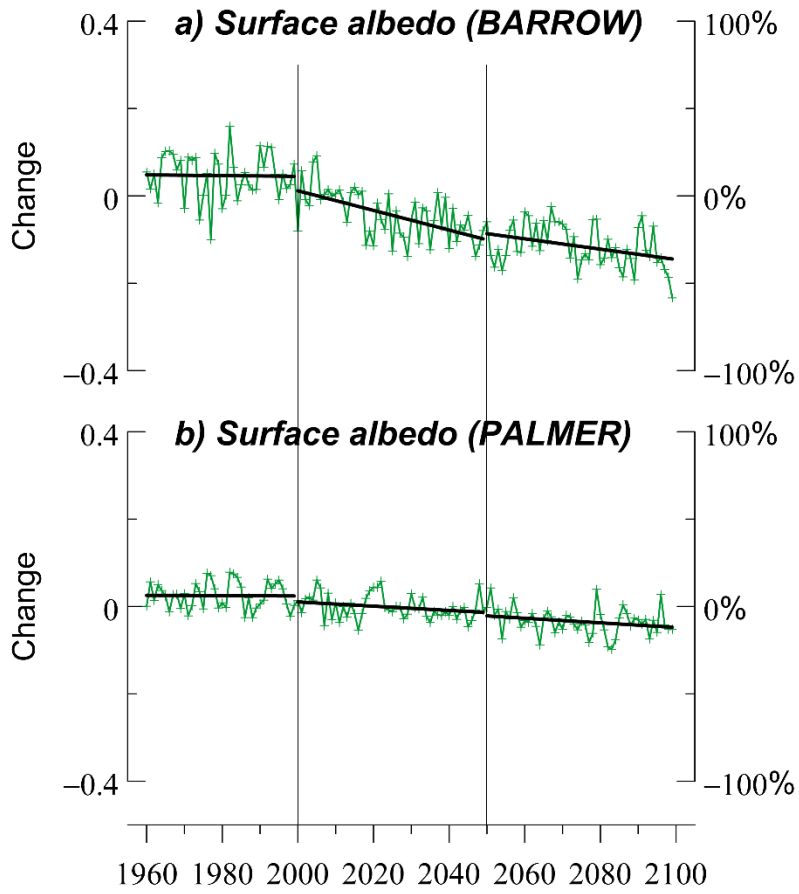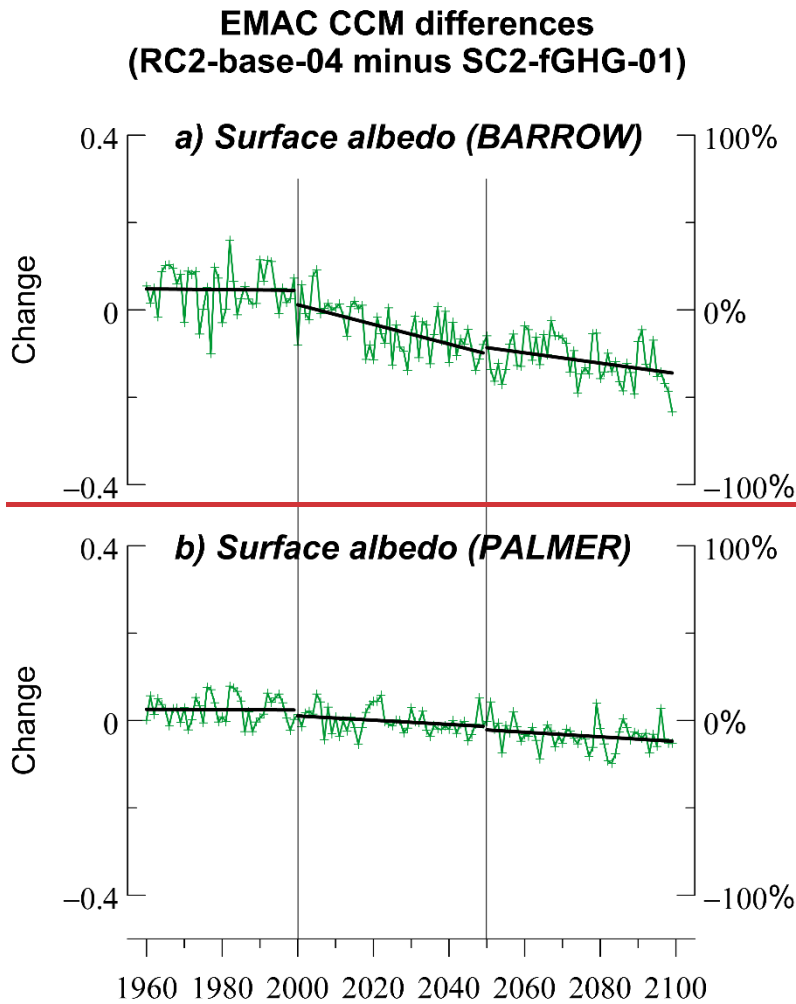
Figure 6̶7. **(a)** Changes in surface albedo at Barrow, Alaska, and **(b)** at Palmer, Antarctica, derived from
the differences between the two model simulations: the one with increasing GHGs (R̶C̶2̶ ̶b̶a̶s̶e̶ ̶0̶4̶REF) and
the one with fixed GHGs (S̶C̶2̶ ̶f̶G̶H̶G̶ ̶0̶1̶FIX). Results refer to the summer season. Data were de-
seasonalized with respect the period 1990–2019 and then were averaged from March to September at
Barrow, and from September to March at Palmer. The left y-axis shows the differences in surface albedo
values and the right y-axis shows the respective differences in % of the mean.

1354
1355
1356
1357
1358
1359

1360

1361